Tuning photovoltaic properties in ferroelectric materials

Anatolii Makhort

UNIVERSITÉ DE STRASBOURG

ÉCOLE DOCTORALE de Physique et Chimie-Physique (ED182)

Institut de Physique et Chimie des Matériaux de Strasbourg

UMR7504 CNRS – Université de Strasbourg

THÈSE présentée par :

Anatolii MAKHORT

soutenue le : **20 novembre 2020**

pour obtenir le grade de : **Docteur de l'Université de Strasbourg**

Discipline / Spécialité : Physique / Physique de la Matière Condensée

Tuning photovoltaic properties in ferroelectric materials

THÈSE dirigée par :

Monsieur KUNDYS Bohdan	Chargé de Recherche (CR1), IPCMS, UMR7504, CNRS-Unistra

RAPPORTEURS :

Monsieur VIRET Michel	Senior Chercheur, CEA Saclay URA CNRS 2464
Madame MATZEN Sylvia	Maître de conférences, Université Paris-Sud 11

AUTRES MEMBRES DU JURY :

Monsieur DOUDIN Bernard	Professeur, IPCMS, UMR7504, CNRS-Unistra
Monsieur GUMENIUK Roman	Professeur, Institut für Experimentelle Physik, TU Bergakademie Freiberg
Monsieur DAYEN Jean-François	Maître de conférences, IPCMS, UMR7504, CNRS-Unistra
Monsieur FOUCHET Arnaud	Chargé de Recherche, UMR6508, CNRS, Laboratoire de cristallographie et sciences des matériaux, CRISMAT, Caen

Acknowledgements

Throughout preparing and writing of this dissertation I have received a great deal of support and assistance.

I would like to express my sincere gratitude to Michel Viret and Sylvia Matzen for accepting to be thesis reviewers and for their time invested into reading this manuscript. I also thank to Bernard Doudin, Roman Gumeniuk, Jean-François Dayen and Arnaud Fouchet for their agreement to be jury members.

I'd like to single out my supervisor Bohdan Kundys. I'm grateful to you for the possibility to be part of this project. For your enormous support, guidance and enthusiasm that motivated me all this years spent on the frontier of science. Your valuable advices and experience both in professional and everyday lives helped me a lot and became landmarks for the future.

I acknowledge the financial support of Grand Est region. I thank Doctoral school of Strasbourg University and its director Aziz Dinia for the possibility to study here. I'm also grateful to the IPCMS director Pierre Rabu and to the responsible of our department Yves Henry for this opportunity to be part of the institute's research team. I'd like to thank Veronique Wernher and Catherine Bonnin for the assistance with administrative procedures.

I also wish to thank to David Halley for being a mid-term jury member and for his useful comments. I'm grateful to Guy Schmerber and Loïc Mager for optical spectroscopy measurements, trainings and valuable discussions. I thank Fabien Chevrier for help in solving technical issues.

I further appreciate the organized trainings and assistance of cleanroom/STNano stuff: Alain Carvalho, Hicham Majjad, Romain Bernard and Sabine Siegwald.

I thank to my colleagues – PhD students: Liudmyla Klochko, Yelyzaveta Berezovska, Adeline Cascales and Matias Grassi.

Last but not least, I'm thankful to my family for their love and support during all my life. I'm grateful to my friends Viktoriia Untilova and Danylo Babich for all you've done for me all this years.

Dedicated to my family...

Contents

List of Figures

Abbreviations

AC	Alternating current
ADC	Analog to Digital converter
APVE	Anomalous photovoltaic effect
BCO	Bismuth chromate $BiCrO_3$
BFCO	Bismuth iron chromium oxide Bi_2FeCrO_6
BFO	Bismuth ferrite $BiFeO_3$
BLFO	Lanthanum doped bismuth ferrite $Bi_{1-x}La_xFeO_3$
BMO	Bismuth manganite $BiMnO_3$
BPVE	Bulk photovoltaic effect
BSNO	Barium-strontium niobate $Ba_xSr_{1-x}Nb_2O_6$
BTO	Barium titanate $BaTiO_3$
BVO	Bismuth vanadate $BiVO_4$
BZT-BCT	Barium zirconate-titanate/barium calcium-titanate $[(BaZr_{0.2}Ti_{0.8})O_3]_{1-x} - [(Ba_{0.7}Ca_{0.3})TiO_3]_x$
Cr:BFO	Cr-doped bismuth ferrite
CRO	Calcium ruthenate $CaRuO_3$
DC	Direct current
EDS	Energy-dispersive spectroscopy
FE	Ferroelectric
FF	Fill factor
FTO	Fluorine-doped tin oxide $SnO_2 \cdot F$
IoT	Internet of things
IQE	Internal Quantum Efficiency
Isc	Short-circuit photocurrent
ITO	Indium tin oxide $In_{1.69}Sn_{0.15}O_{2.85}$
Jsc	Short-circuit photocurrent density

KBFO	Potassium bismuth ferrite $KBiFe_2O_5$
KNO	Potassium niobate $KNbO_3$
LAO	Lanthanum aluminate $LaAlO_3$
LED	Light-emitting diode
LFO	Lutetium ferrite $LuFeO_3$
LMO	Lutetium manganate $LuMnO_3$
LNO	Lithium niobate $LiNbO_3$
LSMO	Lanthanum strontium manganite $La_{1-x}Sr_xMnO_3$
MPB	Morphotropic phase boundary
Nd:BTO	Nb-doped barium titanate
NETD	Noise equivalent temperature difference
NKBiT	Sodium-potassium bismuth titanate $(1-x)(Bi_{1/2}Na_{1/2})TiO_3 - x(Bi_{1/2}K_{1/2})TiO_3$
NSTO	Nb-doped strontium titanate
OpAmp	Operational amplifier
PCE	Power conversion efficiency
PFM	Piezoelectric force microscopy
PLT	Lead lanthanum titanate $(Pb_{1-x}La_x)TiO_3$
PLZT	Lead lanthanum zirconate-titanate $Pb_{1-x}La_x(Zr_yTi_{1-y})_{1-0.25x}O_3$
PMN	Lead magnesium niobate $MgNb_2O_9Pb_3$
PMN-PT	Lead magnesium niobate lead titanate $Pb\left[(Mg_{1/3}Nb_{2/3})_{1-x}Ti_x\right]O_3$
PoC	Proof of concept
Pr:BFO	Pr-doped bismuth ferrite
PT	Lead titanate $PbTiO_3$
PV	Photovoltaic
PWM	Pulse width modulation
PZT	Lead zirconate titanate $Pb(Zr_x, Ti_{1-x})O_3$
S-SWCNTs	Semiconducting single-wall carbon nanotubes
SRO	Strontium ruthenate $SrRuO_3$
STO	Strontium titanate $SrTiO_3$
Tc	Curie temperature
TFO	Thulium ferrite $TmFeO_3$
Voc	Open-circuti photovoltage
XRD	X-ray diffraction

YMO Ytterbium manganate $YMnO_3$

Introduction

The ever increasing demand for cheap and clean energy sources identifies photovoltaic industry as an important alternative solution. However, nowadays photovoltaic market is dominated by solar cells made of semiconductors. This industry is currently facing its fundamental limit of efficiency for single bandgap architecture. Therefore developing new PV cells paradigms and materials becomes an important and timely research challenge. Ferroelectric materials are interesting candidates for future PV applications due to their potential to overcome the fundamental limits of conventional single bandgap semiconductor-based solar cells. Although the photovoltaic effect in ferroelectrics was firstly demonstrated by Chynoweth[1] in 1956, the number of known PV compounds is currently well below 40. The renaissance in this field of research started after discovery of PV effect in the multiferroic BFO[2] Since then we are witnessing the numerous reports each year dedicated to ferroelectric photovoltaic materials and structures contributing to the development of a separate emerging field of research in material science. Such a fast growing interest is on the one hand a result of the increased energy consumption over the last decade (fast growing internet infrastructure: data-centres, servers, IoT devices and others, require more and more electricity each year) and on the other hand a desire for environmental-friendly energy concept realization. The general research trend for photovoltaics is very well illustrated by the number of research articles published each year, see Fig. I (the data was obtained from the WebOfScience archive).

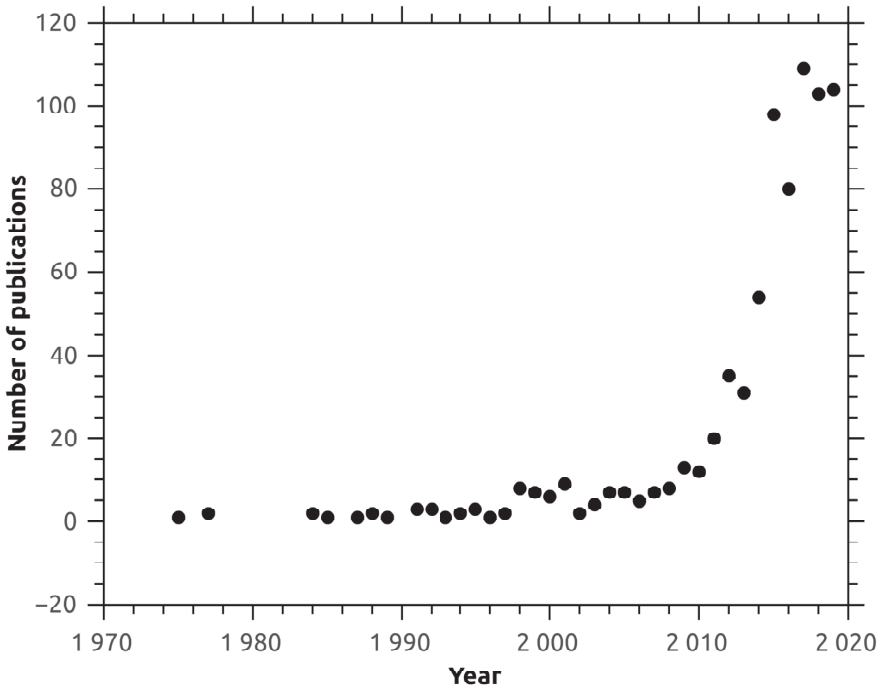

Figure I: Fast growing interest in photovoltaic materials.

Because the amount of voltage generated by a single band-gap semiconductor-cell cannot exceed its corresponding bandgap value, such a technology, now requires realization of more and more complicated architectures, involving multi-bandgap approaches. This strategy, however, rises the costs and endurance issues of the PV-based solar cells and alternative materials must be found. Because the electron-hole pairs are separated only in a narrow region inside the p-n junction, the unique bandgap architecture is basically limited in its PCE to 33.7% by a Shockley-Queisser limit[3]. It results in lower separation efficiency and stimulates conception with multiple p-n junctions in the cell. Therefore, electrically polar materials, where each crystalline unit cell can generate photo-carriers (and charge separation happens throughout the bulk due to the existence of non-zero remnant polarization, see Fig. II) are interesting candidates for future photovoltaic applications. Although a more efficient charge separation and above bandgap photovoltages are advantageous in these materials, understanding physical properties for tailoring their photovoltaic response remains puzzling.

Experiments devoted to basic understanding of physical properties must be focused on the simplest possible and widely available model compounds, to sort out extrinsic contributions resulting into device-dependent PV properties. Therefore, this thesis,

first of all, reports the two new photovoltaic compounds corresponding to the above criteria and secondly, also addresses issues of PV tunability in ferroelectrics. The non-linear character of PV effect with light intensity provides insight to light induced non-equilibrium charge carrier dynamics.

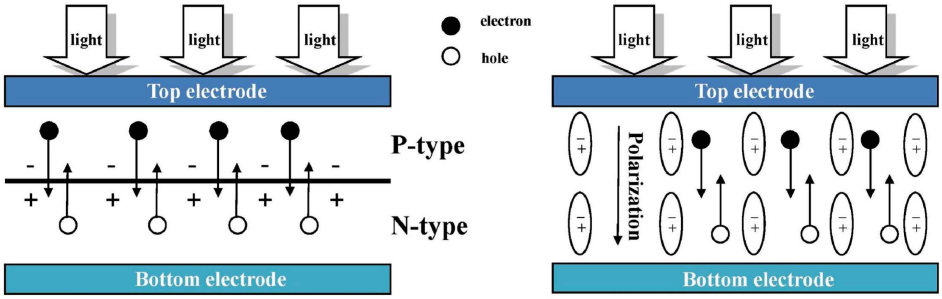

Figure II: Illustration of the working principle of a conventional single-bandgap semiconductor PV device (a) and FE-based one (b). Image taken from [4].

More precisely, the present work describes the discovery of the two PV compounds from the PMN-PT family of FE crystals and demonstrates the possibility of influencing on their photovoltaic properties by the external stimuli, like electric field, ferroelectric history, light intensity, temperature and mechanical stress. It is illustrated how the photovoltaic response can be enhanced by combining different strategies.

Organization of manuscript

This manuscript consists of 7 chapters listed below with concluding remarks, followed by the general conclusions summarizing the obtained results and discussion of potential perspectives.

Chapter 1 gives a brief photovoltaic materials overview with a focus on electrically polar compounds in bulk and thin film forms. Additionally, it introduces the new family of ferroelectric materials that possesses photovoltaic properties even being undoped.

Chapter 2 describes the sample origin and different experimental measurement techniques using which the experimental results described in this manuscript were obtained.

Chapter 3 gives insight into the photopolarization and photovoltage dependence on the ferroelectric state (and history of its change).

In *Chapter 4* the light intensity dependence of PV effect is discussed and a fascinating photoexcited charge carriers dynamics is revealed.

Chapter 5 shows the temperature dependence of photopolarization/photovoltage in the studied compounds of PMN-PT family.

In *Chapter 6* the mechanical stress is reported as one of a key parameters influencing the photovoltaic properties of PMN-PT30% and PMN-PT32% crystals.

The *Chapter 7* provides general conclusions and illustrates some perspectives for using the reported effects even beyond photovoltaics.

Chapter 1

Photovoltaic effect in polar materials

1.1 Overview

The acentric crystalline structure in semi-insulating or insulating polar materials induces an intrinsic electric field comparable with that existing in the p-n junction region of semiconductor-based solar cells. Subsequently, the electrically polar materials with photovoltaic properties gain renewed attention with regard to photovoltaics[5–10] and other attractive multifunctionalities[11–17]. The field of PV in FE was rejuvenated after the discovery of the photovoltaic effect in the multiferroic $BiFeO_3$[2, 18], resulting in the revival of ferroelectric-based photovoltaic operation and related materials[5, 7, 19, 20]. Based on recent progress in photovoltaic efficiency of Bi_2FeCrO_6 films[21], ferroelectric cells might become competitors for conventional photovoltaics in the near future. In this respect, better insight into photo-induced changes of electrical properties over a wide range of temperatures and electric fields would be helpful. Such a study, however, requires high-quality crystals that are free from the surface/interface effects occurring in thin films[22] and grain size dependence occurring in ceramics[23]. This task is challenging because, the total number of currently known photovoltaic-ferroelectric compounds is well below 40[5, 7, 19, 20]. In that respect finding new PV compound among inexpensive single crystals would be beneficial from the both fundamental and application viewpoints.

The ferroelectric material is one that exhibits a spontaneous dipole moment (polarization) electrically switchable with 180°. The spontaneous polarization, however

occurs in the absence of the external electric field as the centres of positive and negative charges doesn't coincide. From the symmetry point of view this is only possible when such a crystal lacks the inversion centre (distinctive feature of polar groups). Hierarchically, all crystals can be classified as showed in Fig. 1.1. There are 32 crystal classes and only $20 + 1$ among them lack a centre of symmetry.

All ferroelectrics are also piezoelectrics, but the opposite is not always true (like in a case of quartz). This class of materials is further divided into two: half of them that also posses the pyroelectric properties (have a unique polar direction) and half that don't. From the hierarchy overview (Fig. 1.1) all ferroelectrics also posses the pyroelectric properties (but with ability of polarization inversion by external electric field) and many of them are used in this context (historically they were viewed as such): abundant of research papers and proceedings are dedicated to the discovery of new pyroelectric materials, performance optimization and their usage as sensors for motion and flame detection. Besides FE memories, insulating ferroelectrics have also been used for years in capacitor fabrication due to the miniaturization possibility (higher the ε is – smaller the capacitor thickness can be) and only recently they started to be considered as a promising photovoltaic candidates.

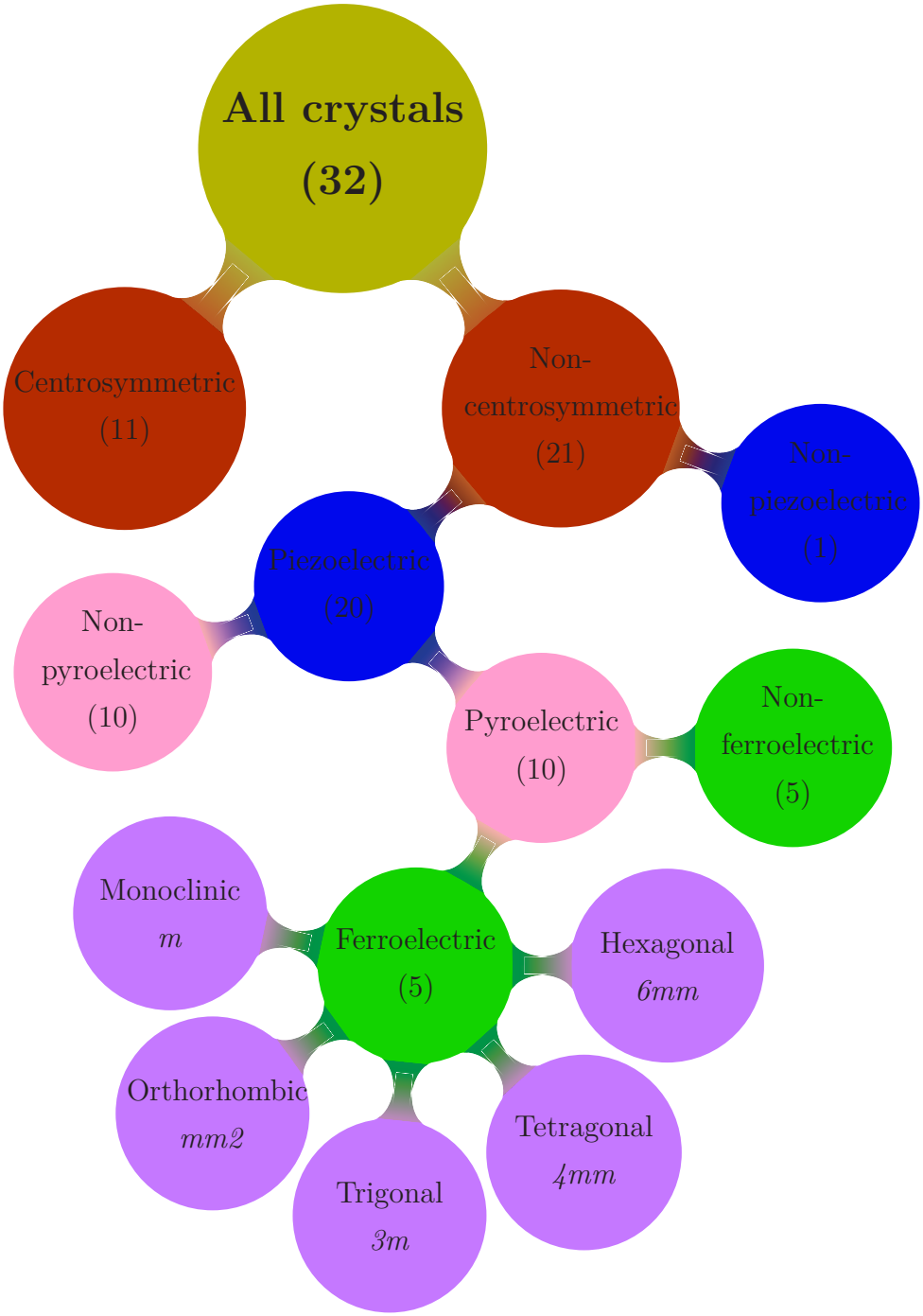

Figure 1.1: Crystals classification from symmetry considerations. Number in parenthesis represents the number of point groups in each crystal class.

For the photovoltaic effect a lack of inversion centre becomes also crucial. As it is one of the necessary conditions that guarantees that newly generated charges will not recombine. Chynoweth[1] was the first one who demonstrated the presence of a photovoltaic effect in non-centrosymmetric BTO crystals (see Fig. 1.2).

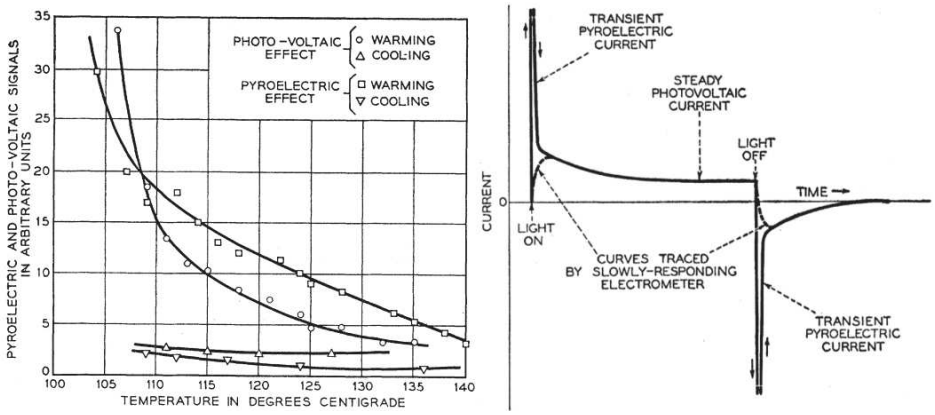

Figure 1.2: Photovoltaic and pyroelectric currents as a function of temperature (left) and current dynamics under single light pulse (right). Originals taken from [1].

Two years later it was observed in $CdTe$[24, 25] films and ZnS single crystals[26]. Later, the bandgap-exceeding photovoltages were firstly measured by Lempicki[27] in ZnS single crystals. This is where the term "anomalous photovoltaic effect" originates. Extensive studies were conducted on ferroelectric $SbSI$[28–31] in view of its photovoltaic properties. Then Chen *et al.*[32] observed the PV response in lithium niobate crystals (LNO), see Fig. 1.3.

Later, Brody *et al.*[33] showed that photovoltages in doped BTO are proportional to the length of crystal, to its remanent polarization and exist only below Curie temperature while decreasing linearly with heating. Later, Glass *et al.*[34] reported the above-bandgap photovoltage in ferroelectric LNO (doped, single crystal) and termed it as a "bulk photovoltaic effect" due to its anisotropy and intrinsic origin. Just after that Brody *et al.*[35, 36] showed the grain-size dependence of a PV effect in doped BTO and PZT ceramics as well as the role of temperature, light intensity and wavelength.

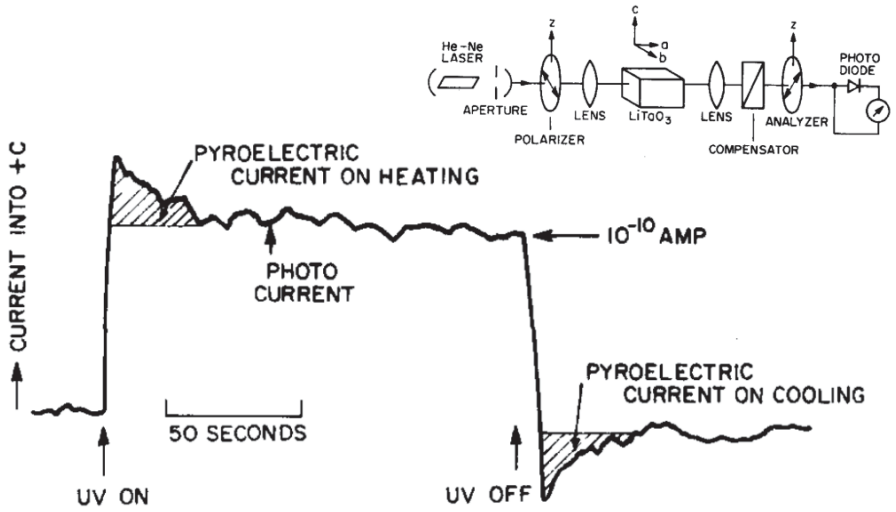

Figure 1.3: Contribution of both the photovoltaic and pyroelectric currents in LNO crystals during the light pulse illumination. Experimental setup is shown at the top right corner. Originals taken from [32].

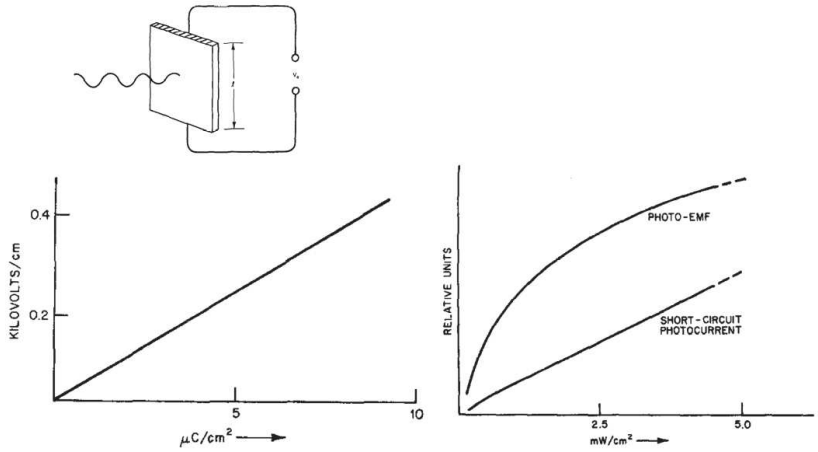

Figure 1.4: Photovoltaic electric field in BTO ceramics as a function of sample's remanent polarization (left). Photovoltaic effect light intensity dependence in PZT (right). Top left image represents the illumination geometry. Originals taken from [36].

Two years later, Fridkin *et al.*[37–39] conducted the temperature-, spectral- and intensity-dependence measurements on ferroelectric compounds (LNO, KNO and BSNO (0.25)) and introduced the theoretical interpretation of obtained results based on the fluctuation model. From that model the current dynamics in ferroelectric crystal shows a non-linear behaviour, followed by the saturation, where the equilibrium between

charge generation, recombination and trapping (under sufficiently high light intensity charges could even be additionally re-excited from their traps into the conduction band) is reached. This kinetics is illustrated by Fig. 1.5.

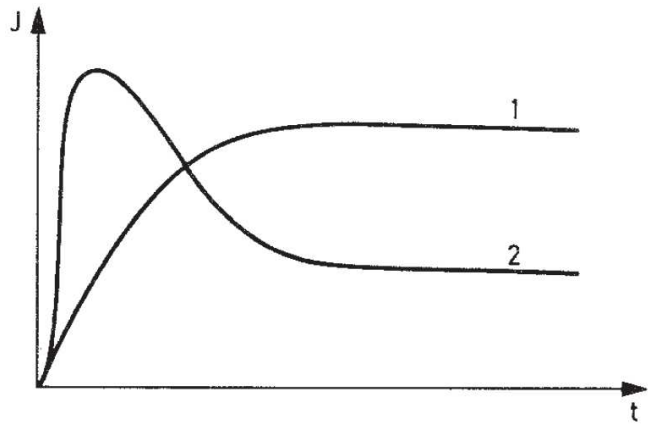

Figure 1.5: Bulk photovoltaic current kinetics (for fluctuations localized on shallow (1) and on deep (2) levels) in n-type ferroelectric crystal (theoretical investigation discussed in[37], original image taken from there).

Furthermore, the authors showed[40, 41] that the effect of optical damage can lead to the anomalous photovoltaic effect. Then authors suggested the existence of the APVE in $PbTiO_3$ (PT)[42]. Later, Brody[43] suggested a nonvolatile memory device based on this effect. Since then photovoltaic effect have been reported in other non-organic materials[44–51], polymers[52–55] and theoretical models were discussed[56–64]. Nonaka *et al.*[65] seeking of improvements to the existing photostrictive* materials for precise actuators, demonstrated that the lead lanthanum zirconate-titanate (PLZT) is a promising candidate due to its good piezoelectricity. Moreover, they showed an interesting light intensity dependence of photocurrent and photovoltage (Fig. 1.6).

Then Grekov *et al.*[66] developed a theory explaining the important role of localized states (especially near Tc with a lot of defects/impurities) in ferroelectric semiconductor crystals influencing its photovoltaic properties. They showed that Curie temperature could be modified by light of proper wavelength and photocurrent could enhance close to the ferroelectric $\rightarrow$ paraelectric transition. One year later, Cho *et al.*[67] observed the photovoltaic effect in $Sn_2P_2S_6$ (in ceramic and crystal forms) under the infrared illumination.

*Photostriction – generation of strain in illuminated sample. It is a combination of photovoltaic and piezoelectric effects. Photo-generated electric field (photovoltaic effect) acts just like external

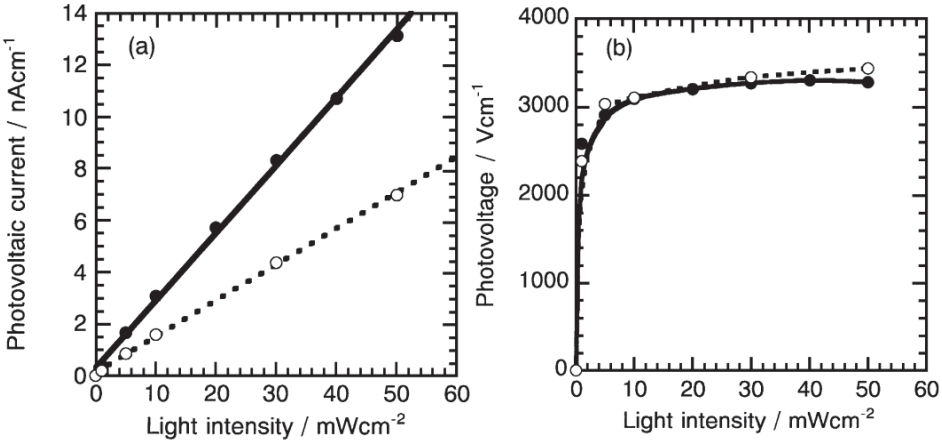

Figure 1.6: Photovoltaic current (left) and voltage (right) dependence on illumination intensity in PLZT (3/52/48). Unfilled points represents the same measurements done for A-site 1% deficient composition. Originals taken from [65].

To this moment PZT becomes a classical FE-photovoltaic material and its characterization continues for sol-gel prepared films by Kholkin *et al.*[68]. Authors discovered the fast photocurrent dynamics caused by UV pulses irradiation and attributed it to the BPVE in this compound. Then Watanabe *et al*[69] demonstrated the non-linear behaviour of PV effect in PZT/STO epitaxial films. Later, Kim *et al.*[70] discussed the grain size and doping dependence of photocurrent in lead lanthanum titanate (PLT) ceramics. Authors introduced an explanation based on formation of the electro-potential barrier (created by trapped on grain boundaries photo-excited electrons) that impedes the movement of other excited electrons. And showed the existence of a critical grain size that maximises the photovoltaic current. Yao *et al.*[71] showed that large V_{oc} can be obtained from poled WO_3-doped PLZT thin film under UV illumination. Results suggest that both photovoltage polarity and magnitude depend on the poling field, as well as bandgap illumination wavelength drastically improves the PV efficiency (such configuration can be used as an UV detector, as was demonstrated by Gan *et al.*[72]). The same is also true for the photocurrent in epitaxial[73] and polycrystalline[74] PZT films. Ichiki *et al.*[75] studied a new layered structure and showed that photocurrent in PLZT can be improved by 2 orders in its magnitude compared to one in bulk. That current is proportional to the illumination area. Later, it was showed[76–78] that this current depends on film thickness: increases exponentially with decrease in thickness

electric field applied to piezoelectric sample.

till the critical point (< 10 nm), where the ferroelectricity vanishes. Moreover, the photovoltage depends on the film thickness[78] and PV conversion efficiency becomes more important at low light intensities. It was found in[79] that trapping and polarization screening by photo-excited charges, as well as asymmetric Schottky barriers at the film-electrode interfaces are responsible for photovoltage degradation in this compound under multi-cycle illumination. Later, it was showed by Bogomolov *et al*[80] that the photocurrent in $Sn_2P_2S_6$ semiconductor ferroelectric films consists of both the unsteady (attributed to pyroelectric effect) and quasi-steady (photovoltaic) components. Each of those has its own temperature dependence: one is decreasing, the other – increasing (and reaches its maximum near the Tc) during heating. A new leap of research started from the discovery of the photovoltaic effect in multiferroic BFO by Choi *et al.*[2] and Yang *et al.*[81] in 2009. Soon, the above-bandgap photovoltage was reported[82] for thin films of this compound. The PV properties were then extensively studied in epitaxial films[83–85], in transition metal modified polycrystalline films[86], in a sol-gel fabricated nanofiber[87], in BTO/BFO[88] and BFO/LSMO/PMN-PT[89] heterostructures. A new trend in the research now is the lead-free[90–100] materials for energy conversion. Table 1.1 shows PV efficiencies of a number of FE-based PV devices (crystals, thin films, multilayer structures). Although the data are reported for different light excitations, the table, nevertheless, summarizes photovoltaic performance of the FE-based PV cells for over the last 20 years.

Table 1.1: Listing of photovoltaic efficiencies (η) of some known ferroelectric compounds and structures. Isc is in A, Jsc is in A/cm^2. Missing efficiencies were calculated approximately (using Eq. (2.22)), and supposing the FF = 100% (FF defined as Eq. (2.24)).

Ferroelectric	**Voc, V**	**Isc or Jsc**	η, %	**Ref**
PZT				
PZT/NSTO	0.7	–	0.6	[101]
ITO/PZT/Pt	0.56	$4 \cdot 10^{-5}$	$8 \cdot 10^{-3}$	[102]
ITO/PZT/Cu_2O/Pt	0.42	$4.8 \cdot 10^{-3}$	0.57	
ITO/PZT/Pt	0.65	$1.4 \cdot 10^{-4}$	0.036	[103]
Pt/PZT/ITO	0.62	$5 \cdot 10^{-5}$	0.011	[104]
Ag/a-Si/PZT/ITO	1.28	$2.56 \cdot 10^{-3}$	1.12	
ITO/PZT/ZnO/Au	0.681	$-4.241 \cdot 10^{-5}$	$\sim 1.25 \cdot 10^{-2}$	[105]

Table 1.1 – continued from previous page

Ferroelectric	**Voc, V**	**Isc or Jsc**	η, %	**Ref**
ITO/PZT/STO/GaAs/Al	0.38	$5.2 \cdot 10^{-2}$	~ 20	[106]
LNO/PZT/Pt	0.248	$4.5 \cdot 10^{-6}$	$2.79 \cdot 10^{-6}$	[107]
LNO/PZT/CuO/Pt	0.27	$2.7 \cdot 10^{-5}$	$1.82 \cdot 10^{-5}$	
Pt/PZT/Pt	-1.01	$1.55 \cdot 10^{-4}$	0.035	[108]
PLZT				
PLZT (5/54/46)	0.12	$-4.06 \cdot 10^{-7}$	$5 \cdot 10^{-5}$	[109]
	0.24	$-7.88 \cdot 10^{-7}$	$1.03 \cdot 10^{-4}$	
	0.37	$-3.6 \cdot 10^{-6}$	$7.08 \cdot 10^{-4}$	
PLZT (3/52/48)/NSTO	–	$9.15 \cdot 10^{-7}$	0.28	[77]
		$2.32 \cdot 10^{-6}$	~ 0.04	
		$3.376 \cdot 10^{-4\dagger}$	$18.7^{\dagger}$	
PLZT (3/52/48) (001)	0.96	$1.07 \cdot 10^{-6}$	$6.1 \cdot 10^{-8\ddagger}$	[110]
PLZT (3/52/48) (111)	0.82	$4.30 \cdot 10^{-7}$	$2.1 \cdot 10^{-8\ddagger}$	
PLZT (3/52/48)/NSTO	–	$\sim 5.5 \cdot 10^{-8}$	~ 0.01	[78]
BFO				
ITO/BFO/SRO	$0.8 - 0.9$	$1.5 \cdot 10^{-3}$	$0.128^{\S}$	[81]
BFO	16	$1.2 \cdot 10^{-4}$	$\sim 10^{-3}$	[82]
ITO/poly-BFO/Pt	–		0.125	[111]
Au/poly-BFO/Pt	–		$5 \cdot 10^{-3}$	
BFO/top Pt electrodes	–		$\sim 5 \cdot 10^{-5\S}$	[112]
BFO nanotubes	–	–	0.207	[113]
Pr:BFO nanotubes	-0.21	$8.9 \cdot 10^{-10}$	0.5	
Cr:BFO nanotubes	-0.12	$3.5 \cdot 10^{-10}$	0.106	
BFO single crystal	–		$3 \cdot 10^{-3}$	[2]
oriented BFO (001) films	–		$7 \cdot 10^{-4}$	[83]
BFO/NSTO	0.04	$6 \cdot 10^{-3}$	0.03	[114]
Gr***/BFO/Pt	0.2	$2.8 \cdot 10^{-3}$	0.14	[115]
ITO/BFO/FTO	0.63	$1.3 \cdot 10^{-4}$	$2.73 \cdot 10^{-2}$	[116]
Au/BVO/thin BFO/FTO	1.0	$1.4 \cdot 10^{-4}$	0.039	[117]
ITO/Ca:BFO/Au	0.42	$2.4 \cdot 10^{-5}$	$7.2 \cdot 10^{-3}$	[118]
BFO annealed at $550°C$	0.11	$4.327 \cdot 10^{-5}$	$1.62 \cdot 10^{-2}$	[119]
BFO annealed at $600°C$	0.075	$2.031 \cdot 10^{-5}$	$2.03 \cdot 10^{-3}$	

Table 1.1 – continued from previous page

Ferroelectric	**Voc, V**	**Isc or Jsc**	η, %	**Ref**
BFO annealed at $650°C$	0.078	$0.99 \cdot 10^{-5}$	$3.66 \cdot 10^{-3}$	
ITO/ZnO/BFO films/Pt	$--$	$3.4 \cdot 10^{-4}$	0.33	[120]
ITO/Ba:BFO/Au	0.58	$3.4 \cdot 10^{-5}$	$6 \cdot 10^{-3}$	[121]
ITO/Sr:BFO/Au	–		$4 \cdot 10^{-3}$	[122]
Au/BTO/$(BFO/BTO)_2$/Pt/Ti	-1.25	$3.184 \cdot 10^{-4}$	0.067	[123]
ITO/$(BFO/BCO)_4$/CRO/LAO	~ 2	$-1.3 \cdot 10^{-5}$	~ 0.01	[90]
ITO/BFOBMO/NSTO	0.56	$3.5 \cdot 10^{-3}$	1.43	[124]
ITO/Sm:BFO/Au	–		0.37	[125]
Au/(BFO films)$_3$/Pt	0.41	$1.6 \cdot 10^{-5}$	0.015	[126]
Au/(BFO films)$_{11}$/Pt	1.28	$1.05 \cdot 10^{-4}$	0.242	
m-TiO_2/BFO films/NiO	0.67	$5.1 \cdot 10^{-4}$	0.19	[127]
Gr***/BFO/ZnO/Gr***/ITO	0.67	$\sim 1.32 \cdot 10^{-2}$	7.4	[128]
Pt/BFO/NSTO	0.206	$3.194 \cdot 10^{-3}$	2.23	[129]
Pt/S-SWCNTs/BFO/NSTO	0.233	$7.521 \cdot 10^{-3}$	4.409	
ITO/ZnO/BFO/PbS/Ag	0.11	$-0.61 \cdot 10^{-6}$	$1.63 \cdot 10^{-5}$	[130]
ITO/Ni:ZnO/BFO/PbS/Ag	0.13	$-2.56 \cdot 10^{-6}$	$9.37 \cdot 10^{-5}$	
ITO/CdS/BFO/PbS/Ag	0.13	$\sim -0.24 \cdot 10^{-3}$	$7.65 \cdot 10^{-3}$	
ITO/ZnO/BFO/C	0.19	$-1.59 \cdot 10^{-6}$	$8.07 \cdot 10^{-5}$	
ITO/Ni:ZnO/BFO/C	0.11	$-0.51 \cdot 10^{-6}$	$1.51 \cdot 10^{-5}$	
Au/BFO††/FTO	0.81	$2 \cdot 10^{-3}$	0.99	[131]
Au/BFO‡‡/FTO	0.87	$2.5 \cdot 10^{-3}$	1.36	
Au/BLFO(0.05)‡‡/FTO	0.95	$2.56 \cdot 10^{-3}$	1.5	
Au/BLFO(0.05)‡‡/$TiO_2^{\S\S}$/FTO	1.74	$3.7 \cdot 10^{-3}$	5.62	
Au/BLFO(0.05)‡‡/$SnO_2^{\S\S}$/FTO	1.69	$4.18 \cdot 10^{-3}$	5.45	
Au/BLFO(0.05)‡‡/ZnO§§/FTO	1.23	$4.08 \cdot 10^{-3}$	4.11	
BTO				
BTO	-0.82	$-4.4 \cdot 10^{-6}$	$9.6 \cdot 10^{-4}$	[132]
Nd:BTO 2%	-1.07	$-5 \cdot 10^{-6}$	$1.4 \cdot 10^{-3}$	
Nd:BTO 3%	-1.01	$-3.2 \cdot 10^{-6}$	$8.5 \cdot 10^{-4}$	
Nd:BTO 5%	-0.98	$-2.5 \cdot 10^{-6}$	$6.3 \cdot 10^{-4}$	
BTO	1.2	$1.91 \cdot 10^{-2}$	4.8	[8]

Table 1.1 – continued from previous page

Ferroelectric	**Voc, V**	**Isc or Jsc**	η, %	**Ref**
BFCO				
ITOBFCO/SRO/NSTO/MgO	0.52	$1.38 \cdot 10^{-2}$	2.65	[133]
ITO/BFCO/SRO/STO	0.79	$1.17 \cdot 10^{-2}$	3.3	[21]
ITO/$(BFCO)_3$/NSTO	0.84	$2.06 \cdot 10^{-2}$	8.1	
ITO/NiO/BFCO/NSTO	0.53	$8 \cdot 10^{-3}$	2	[134]
BMO				
ITO/BMO/NSTO	~ 0.56	$\sim 0.23 \cdot 10^{-3}$	0.1	[135]
ITO/BMO/NSTO	1.36	$\sim 7.03 \cdot 10^{-3}$	3.96**	[136]
Other compositions				
Pt/NKBiT(0.18)/Pt	-0.74	$16.4 \cdot 10^{-9}$	~ 0.01	[137]
ITO/NKBiT(0.18)/Pt	-0.94	$45.25 \cdot 10^{-9}$	~ 0.035	
ITO/h-LMO/Pt	-0.71	$0.52 \cdot 10^{-3}$	0.11	[138]
ITO/h-YMO/Pt	-0.66	$0.55 \cdot 10^{-3}$	0.108	
ITO/BLFO(0.1)/LSMO/STO	2.05	$0.31 \cdot 10^{-3}$	0.82	[139]
BZT-BCT(0.5)/ITO	~ 0.8	$\sim 7.26 \cdot 10^{-5}$	~ 0.01	[93]
ITO/h-YbFO/Pt/MgO¶	-0.52	$2.1 \cdot 10^{-5}$	$3.12 \cdot 10^{-3}$	[140]
ITO/h-YbFO/Pt/Al_2O_3‖	-0.46	10^{-5}	$1.21 \cdot 10^{-3}$	
ITO/BFO/SRO/STO	-0.49	$8 \cdot 10^{-6}$	$1.17 \cdot 10^{-3}$	
ITO/h-TFO/Pt	-0.42	$2.1 \cdot 10^{-5}$	$2.3 \cdot 10^{-3}$	
ITO/h-LFO/Pt	-0.4	$9 \cdot 10^{-6}$	10^{-3}	
FTO/TiO_2/KNBY¶¶/p-NiO/Au	1.56	$6.3 \cdot 10^{-4}$	0.85	[141]
Au/KBFO/Au	1.89	$3.04 \cdot 10^{-4}$	0.11	[142]

The state of the art and emergent nature of the field is very well illustrated by the

†From the simulation
‡Max efficiency
§IQE
¶FE thin film under compressive (substrate-induced) strain
‖FE thin film under tensile (substrate-induced) strain
**PCE close to the average one of 5 samples
††FE thin film prepared by magnetron sputtering
‡‡FE thin film prepared by pulsed laser deposition
§§Electron transport layer
¶¶(K,Bi)(Nb,Yb)O_3
***Graphene

abundance of recent review papers on photovoltaic properties in the electrically polar materials[5, 7, 15, 20]. From the literature overview several conclusions could be made at the time of undertaking of this PhD program, as follows:

1. The number of known PV electrically polar materials is low, although the effect can theoretically exist in any acentric (polar) material[58].

2. There is a possibility to tune photovoltaic effect using electric field, but its mechanism is not enough clear. Although some articles reported electric field poling dependence[143, 144] of the PV effect, its clear hysteretic nature was established only recently[145, 146].

3. Although the domain walls were known to modify PV response[82, 112, 147–149] the mechanism was not clear. I'm convinced that the reported results on the hysteresis nature of the PV effect contribute to the clarification of this issue[145, 146].

4. The photovoltaic effect can be also tuned by extrinsic parameters (defects, electrodes, surface/interface effects)[144]. So this should be taken into account and light illumination via semitransparent electrode should be avoided in the geometry of the experiment as it can lead to additional charge injection[150].

5. The photovoltaic properties can also depend on strain and temperature[145] in these materials.

Unlike for photovoltaic semiconductors, the above state of the art information highly suggested the tunability of the PV response in FE and very interesting physics behind. This thesis contributes significantly to the state of the art in this field of research both directly and indirectly. The direct contribution may be determined via the two new photovoltaic compounds discovery and by evidencing a hysteretic nature of photoresponse as well as by its temperature and pressure dependences. The indirect contribution can be determined via finding non trivial light intensity dependence of the PV effect leading to the remanent effects and suggesting a presence of recombination centres generally unfavourable for PV but offering interesting application possibilities for memories and beyond (see Chapter 7).

1.2 The $Pb[(Mg_{1/3}Nb_{2/3})_{1-x}Ti_x]O_3$ compounds as new photovoltaic candidates

The usage of ferroelectric materials with multiferroic orders offers the additional possibilities of tuning their photovoltaic effect. That's why after the discovery of the photovoltaicity in BFO[2, 18, 81] the ferroelectric materials re-gained so much attention [5, 7, 13, 19, 20, 151]. In a seek of sorting-out most of the extrinsic contributions (surface/interface effects, grain-size dependence in ceramics, and so on) the samples in form of single crystals are preferable for performing the fundamental research. Unfortunately, the preparation of most attractive BFO crystals requires special procedures to grow the high-quality single crystals making it rarely available for a reasonable price and thus limiting its commercial usage. In this research the alternative model material is introduced.

The parent compound to the system of interest is the lead titanate, $PbTiO_3$ (or PT), which represents the "normal" ferroelectrics – ones that are characterized by a sharp phase transition (in dielectric permittivity versus temperature measurements) to paraelectric state while heating. This abrupt transition (see Fig. 1.7(a)) manifests the lower crystalline symmetry change to higher one (cubic) with the dielectric permittivity that satisfies the Curie-Weiss law:

$$\varepsilon_r = \frac{C}{T - T_c} \tag{1.1}$$

In contrast to that, relaxor ferroelectric PMN (lead magnesium niobate) doesn't have a precisely defined transition temperature due to the broad peak (in this case temperature T_{max} is identified by the peak's maximum), which additionally is not always reflecting the structural phase transition and dielectric permittivity is frequency dependent (see Fig. 1.7(b)). In this material the local polar regions exist even above T_{max}. Properties of both these types of ferroelectrics can be combined into PMN-PT solid solution system. In this case the PMN-PT, starting from 30% and above of PT concentration, behaves like a "normal" ferroelectric. The unit cell of such composition (in rhombohedral phase) is shown in Fig. 1.8. The most common ways of structural modification are the vacancy introduction (vacancy defect), atom substitution and impurity addition (doping). Such modifications make an important contribution to the sample's polarization through the interfacial/space charge polarization mechanism (see Chapter 2). The free charge

carriers (existing in material or photo-excited) migrate within the FE under its internal electric field. Some of them may be trapped by defects (vacancy, dislocation, impurity centre or grain boundary in ceramics) creating a localized charge accumulation which might lead to the increasing of dipolar moment. This in turn could be used to tune the material's properties, like photovoltaicity and piezoelectricity.

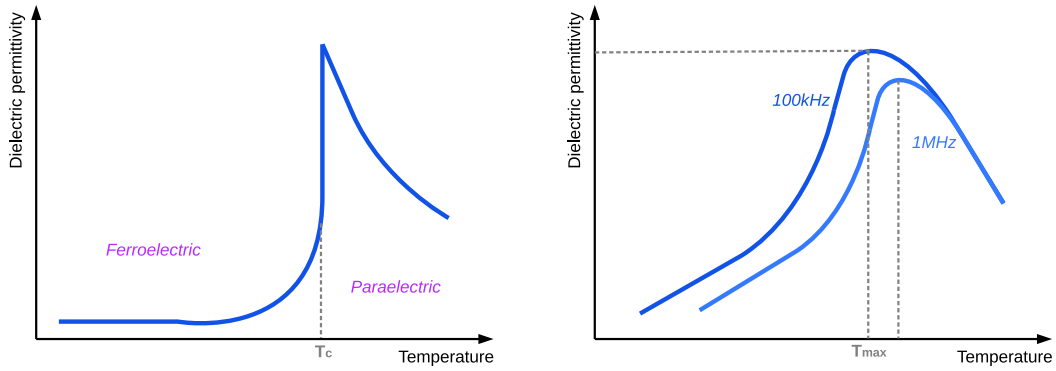

(a) (b)

Figure 1.7: Schematic representation of dielectric permittivity as a function of temperature in "normal" (a) and relaxor (b) ferroelectrics.

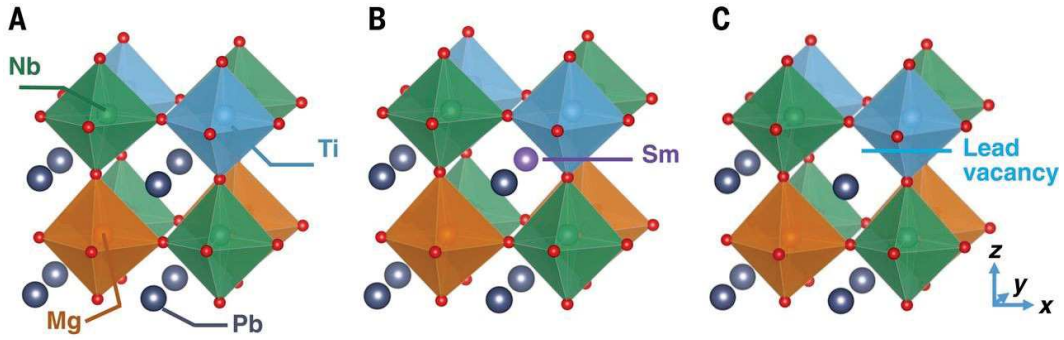

Figure 1.8: PMN-PT unit cell in Rhombohedral phase (A) with Samarium-substituted lead atom (B) and lead vacancy ("defect") (C) (original taken from [95]).

The MPB* of PMN-PT occurs at $30 - 35\%$ of PT and involves the competition between orthogonal and monoclinic phases, which act as a link between the PMN-rich rhombohedral and PT-rich tetragonal phases (Fig. 1.9).

*Term "morphotropic phase boundary" refers to the tetragonal $\leftrightarrow$ rhombohedral phase transitions as a result of composition change or a mechanical strain. The abrupt changes in the crystalline

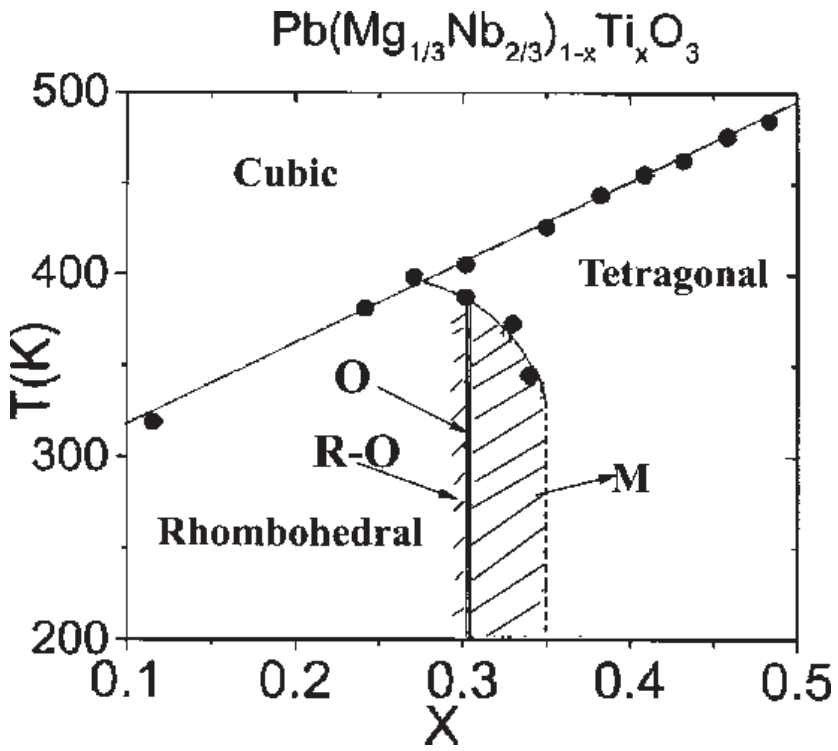

Figure 1.9: Phase diagram of PMN-PT crystals[152]. O, and M refer to orthorhombic, and monoclinic phases, respectively.

The crystalline ordering modifies Curie temperature and determines piezoelectric response having maximum at $x = 0.3$ (Fig. 1.11). The photovoltaic properties were not investigates in the pure compounds. However, for the $x = 0.36$ compound doped with WO_3 the photovoltaic effect was reported[153] in 2006. To prove that this composition is a ferroelectric, authors measured the polarization loop versus E-field in darkness (as presented in Fig. 1.14). Moreover, they demonstrated (Fig. 1.15) that poled samples exhibit similar photovoltaic responses (points for $E = 5$ kV/cm and $E = 10$ kV/cm coincide well) and have much larger photovoltage compared to the unpoled state. Additionally, near-UV illumination shows much stronger photovoltaic responses.

Based on these results and large availability of this compound (due to relatively simple growing process) this family was chosen as a good candidate. Moreover, it is also a FE with a rich phase diagram and remarkable piezoelectric properties (composition was optimized to give high d_{31} and d_{33} coefficients), especially in the morphotropic

structure close to this region causing the large variations in dielectric and electromechanical (d_{33}, etc) properties in ferroelectric materials.

phase boundary region, where different crystalline phases are stabilized in a delicate balance giving a possibility to exploit this sensitive to external stimuli state (as a result – widening the tuning potential and efficiency).

As was already mentioned, the MPB represents the keen interest among scientists, so the reasonable action was to choose the 32% composition as it is right in the middle of this region, commercially available and its photovoltaic properties haven't been studied yet. Driven by success[145] with this composition and by necessity of improvement and tunability of the PV effects the next step was to take the 30% composition.

This choice was motivated by its particular position in the phase diagram (Fig. 1.9 and Fig. 1.11) where subtle balance between thermodynamically equivalent phases is taking place. Moreover keeping in mind that the piezoelectricity and photovoltaicity can be closely coupled[154] the improvement in one could modify the other. Therefore, moving towards the edge of the MPB can amplify additional degree to tune the PV properties.

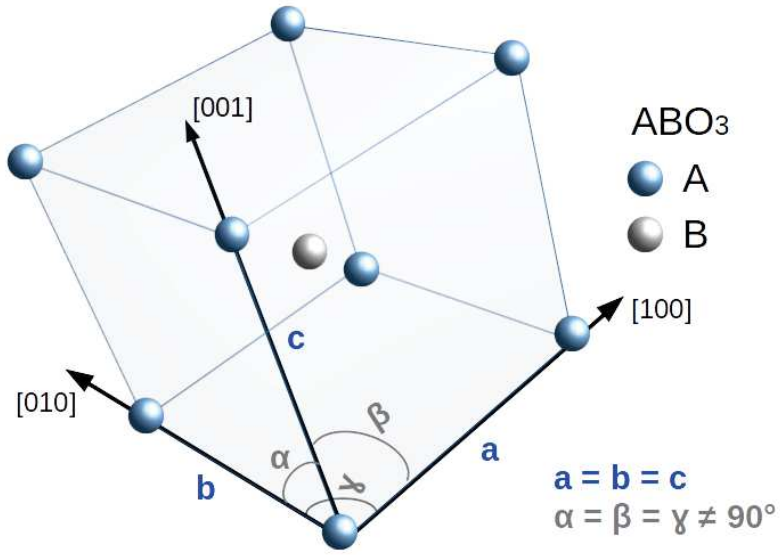

Figure 1.10: Crystalline lattice of ABO_3 (perovskite) in rhombohedral phase.

Lattice parameters for PMN-PT30% composition[155] at $300° K$ (rhombohedral phase, see Fig. 1.10):

a, Å	b, Å	c, Å	α, °	β, °	γ, °
4.019	4.019	4.019	89.91	89.91	89.91

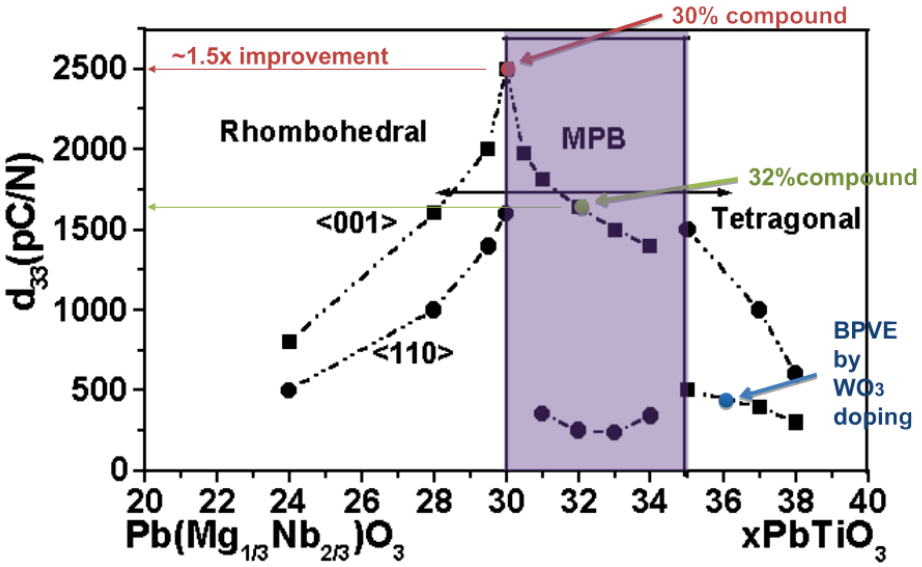

Figure 1.11: Piezoelectric constant (d_{33}) dependence on PMN-PT composition (phase) and orientation. Original taken from [156].

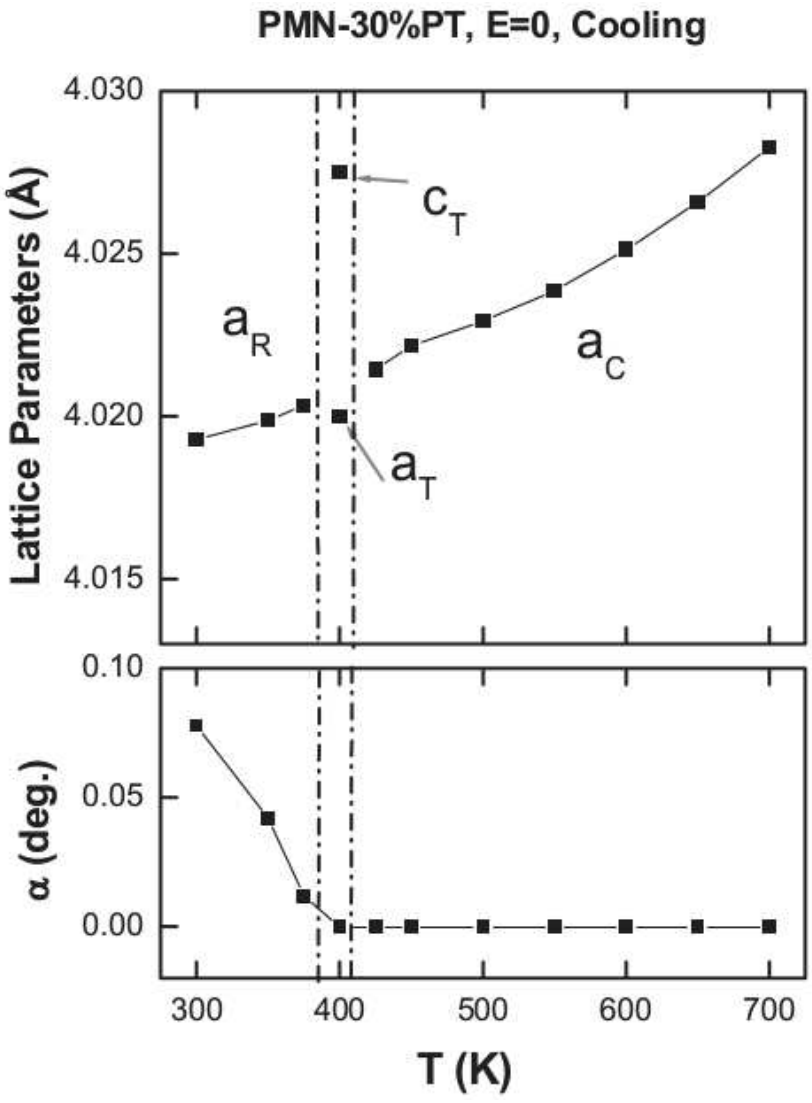

Figure 1.12: PMN-PT30% lattice parameters versus temperature under zero bias (original taken from [155]).

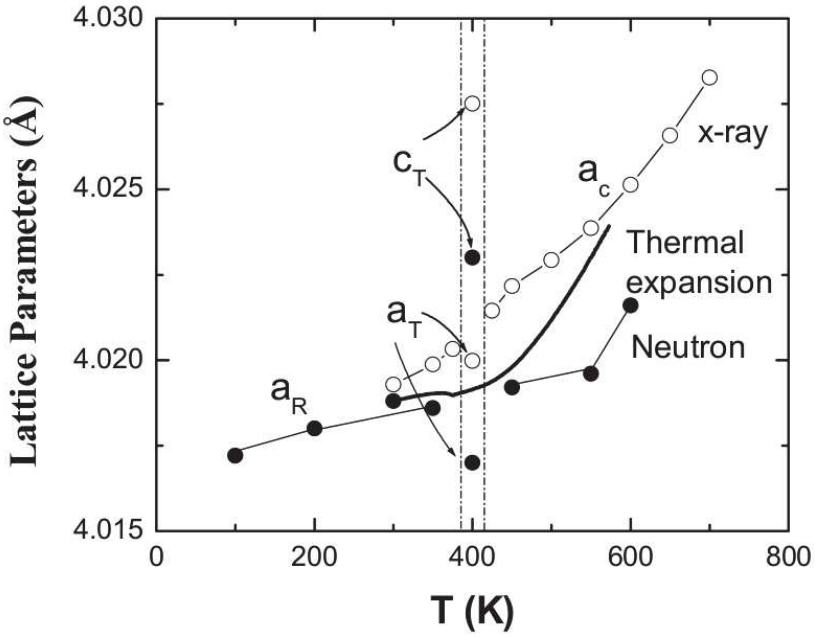

Figure 1.13: PMN-PT30% lattice parameters (a and c) versus temperature measured by XRD, thermal expansion and neutron scattering[155].

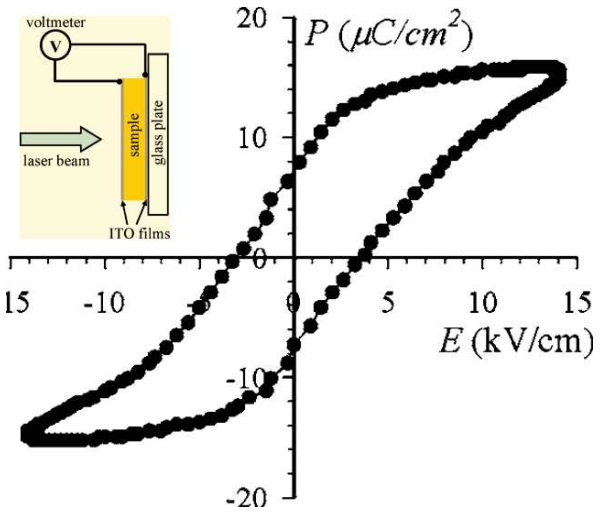

Figure 1.14: PMN-PT36% FE loop and experimental configuration (inset), originals taken from [153].

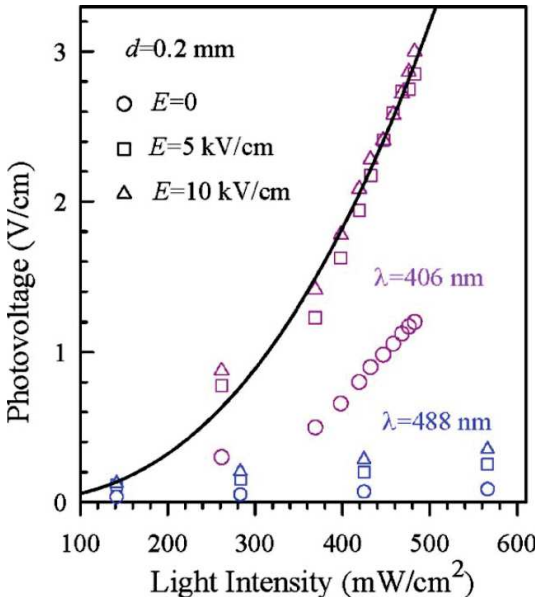

Figure 1.15: PMN-PT36% photovoltage versus light intensity and poling fields (original taken from [153]).

Chapter 2

Preparation and characterization of samples

2.1 Energy-dispersive X-ray spectroscopy

Thanks to important piezoelectric properties the PMN-PT crystals can be obtained commercially at low price. Ferroelectric single crystals of the both compositions were ordered from the *Crystal GmbH*[157] company (Germany) in the form of plates $10 \times 10 \times 0.3\,mm^3$ with [001] orientation and in a spontaneous polarization state. Top and bottom planes have been polished by a manufacturer to optical quality. These plates were cut into smaller pieces of the desired sizes by using a diamond wire saw. Due to their commercial value the detailed procedure of crystal growth is not available. Therefore we decided to verify their content before measurements. To this end the exact composition of PMN-PT compounds was investigated by the energy-dispersive X-ray spectroscopy. The sample was covered by a thin carbon film to make the surface conductive. The scan was performed under the electron beam accelerating voltage of 15 kV and take-off angle of 30°. The EDS spectrum confirmed an absence of significant amount of impurities and the exact content of each compound was found to be in correspondence with the data of supplier.

2.2 Impedance spectroscopy

Impedance spectroscopy is an electrical method of measuring dielectric properties of material as a function of excitation signal (AC voltage) frequency – frequency sweeps. As this externally applied AC electric field interacts with the material's intrinsic charges (electrons, ions, polar molecules) and so with dipoles – the overall ferroelectric polarization (dipole orientation and interactions, free/surface/interface charges) changes modify the resulting impedance: its magnitude reflects carriers concentration and its angle (phase shift – time delay between excitation and response) characterizes the intrinsic properties (mobility). As it will be shown later it is a particularly useful method to "take an electrical picture" of the sample before and after excitation. The related electrical ground state naturally depends on the "electric building blocks' of the sample" i.e. FE domains and free charges can be verified on demand by using the impedance spectroscopy after each excitation (see Fig. 2.3).

The LCR meters are the measuring instruments that can measure an impedance of a sample. Impedance (also expressed as $\tilde{Z}$) indicates resistance to the flow of an AC current I. It can be calculated from this current I flowing through the sample and the voltage V across the sample's contacts. This type of a physical property often expressed as a vector on a complex plane (Figure 2.1), so using this approach the LCR meters measure not only the ratio of the RMS values (of current and voltage), but also the phase difference between current and voltage waveforms (see Figure 2.2):

$$\tilde{Z} = \frac{\tilde{V}}{\tilde{I}} = \frac{\left|\tilde{V}\right|e^{j\varphi_v}}{\left|\tilde{I}\right|e^{j\varphi_i}} = R + jX = R + j \cdot 2\pi f L, \tag{2.1}$$

where R is a resistance, X – reactance, f – test frequency, L – inductance.
From this complex impedance the different intrinsic parameters can be calculated, like sample's capacitance, dielectric permittivity ε (knowing the sample's shape and dimensions) and resistance:

$$D = \frac{1}{2\pi f C_p R_p} \tag{2.2}$$

$$Q = \frac{1}{D} = \frac{|X|}{R} \tag{2.3}$$

where D is a dissipation factor and Q – quality factor, C_p – parallel capacitance and R_p – parallel resistance.

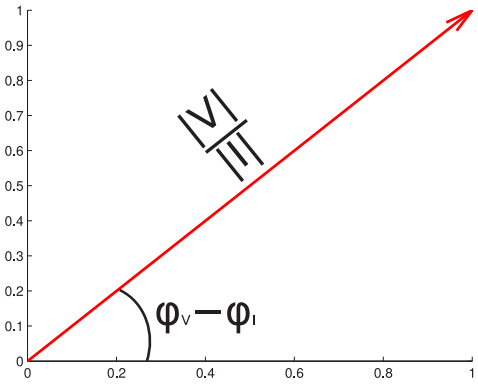

Figure 2.1: The complex-plane representation of impedance

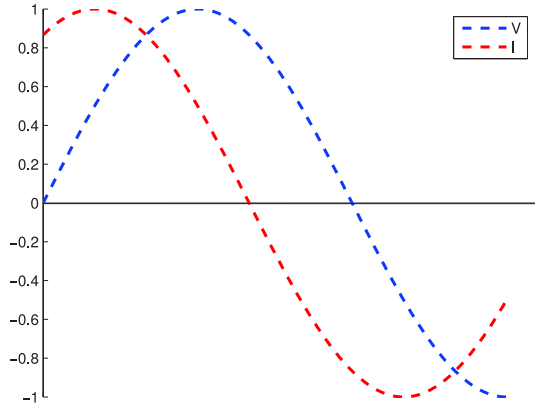

Figure 2.2: The phase shift between V_{RMS} and I_{RMS}

While applying the external electric field $\vec{E}$ across the sample, its charges will try to reduce (screen) this field and will develop an electric displacement $\vec{D}$ expressed as:

$$\vec{D} = \varepsilon_0 \vec{E} + \vec{P}, \tag{2.4}$$

where $\vec{P}$ is the material's intrinsic polarization. It can be expressed as a an expansion of arbitrary order (approximation depends on the material's type, frequency and magnitude of the external electric field):

$$P_i = \varepsilon_0 \sum_{j=1}^{3} \hat{\alpha}_{ij} E_j + \varepsilon_0 \sum_{j,k=1}^{3} \hat{\beta}_{ijk} E_j E_k + \varepsilon_0 \sum_{j,k,l=1}^{3} \hat{\chi}_{ijkl} E_j E_k E_l + \dots \ , \tag{2.5}$$

where $\hat{\alpha}$ is the second- and $\hat{\beta}$ – third- and $\hat{\chi}$ – fourth-rank polarizability tensors. If we consider the linear approximation then only the first term in this sum is non-zero, so the corresponding electric displacement becomes:

$$\vec{D} = \varepsilon_0 (1 + \hat{\alpha}) \vec{E} = \hat{\varepsilon} \vec{E}, \tag{2.6}$$

where $\hat{\varepsilon}$ is the dielectric constant of a bulk material. Its magnitude depends on the charges' response time – how fast enough they can move to remain synchronized with the external field changes. The heavier these charges become – the more time is needed. So the polarizability can be expressed as:

$$\hat{\alpha} = \hat{\alpha}_e + \hat{\alpha}_i + \hat{\alpha}_d + \hat{\alpha}_s, \tag{2.7}$$

and so do dielectric constant:

$$\hat{\varepsilon} = \varepsilon_0 + \hat{\varepsilon}_e + \hat{\varepsilon}_i + \hat{\varepsilon}_d + \hat{\varepsilon}_s \tag{2.8}$$

This expression is accounting for the 4 following mechanisms (sorted in descending order by their response time to external electric field change):

- electronic density redistribution (contributes to $\hat{\alpha}_e$);
- displacement of ions/bond stretching ($\hat{\alpha}_i$);
- alignment of dipoles/reorientation of polar molecules ($\hat{\alpha}_d$);
- long range charge migration $\rightarrow$ space and interfacial charges ($\hat{\alpha}_s$).

The last two are of a particular interest as dipole reorientation modifies the FE domain structure and free charge carriers migrations are altering by the presence of defects: lattice vacancies, dislocations, impurity centres (doping contributions), grain boundaries (especially in ceramics) and others. So this is a powerful method that allows to keep track of FE domain modifications, overall defects concentration and sample's integrity changes caused by poling procedures and light illumination. The initially present poly-domain structure in a sample with spontaneous polarization state is clearly represented in Fig. 2.3 (black) and disappears after poling $+P_R$ (green) and $-P_R$ (blue). The "noise" in the low frequency region for depolarized sample testifies for the domains contribution that is slower in electric response and disappears after FE saturation. In contrast, the high frequency peaks appear for saturated sample are the signature of FE dipoles ordering, since FE dipoles are able to respond faster to external AC electric fields. Such measurements can therefore be used to verify if electric response of the sample has been modified before or after excitation. This is particularly useful for FE ground sate verification as minimal invasive technique.

All the capacitance, resistance and dielectric permittivity measurements in this work were performed using the *Agilent E4980a* LCR meter with the pseudo four-probe technique (see Fig. 2.4). A keen selection of a signal frequency defines the signal-to-noise ratio: the larger it is – the higher becomes this ratio. The same time, frequencies in audio range (usually 1 kHz and below) manifest the interfacial effects (also keeping in mind that AC lines have 50/60 Hz) as well as at too high frequencies (> 20 MHz) are highly attenuating in dipolar interactions. From these considerations, in this work

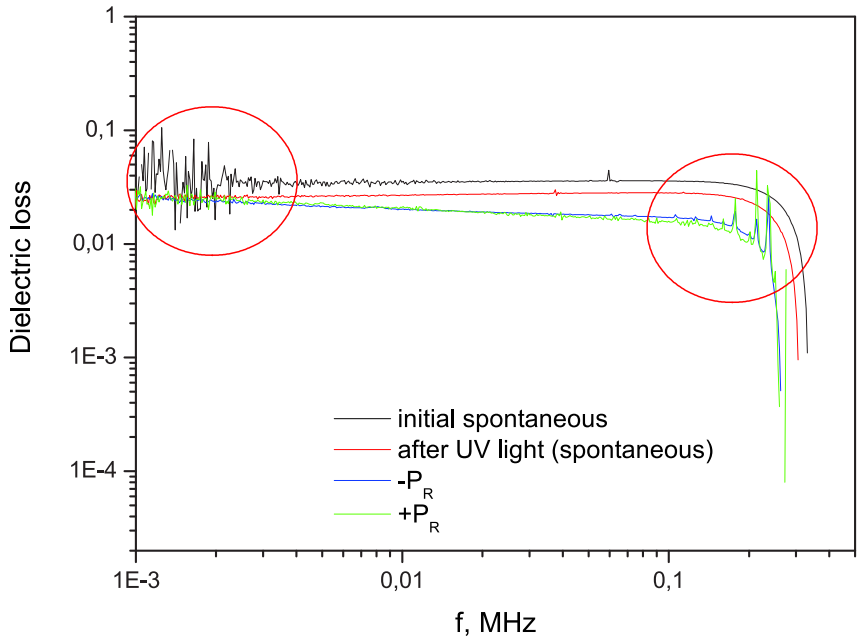

Figure 2.3: Example of the frequency dependence of dielectric loss in the sample recorded for different polarization states.

the 100 kHz was selected as an excitation frequency for dielectric measurements, while the range of $\approx$ 1 kHz to 2 MHz was used for impedance spectroscopy.

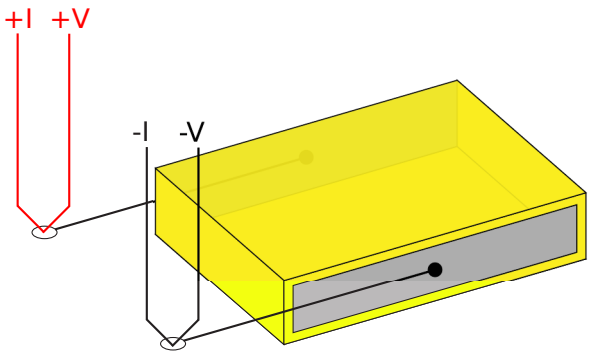

Figure 2.4: Pseudo four-probe technique configuration: when $+I$ is connected with $+V$, as well as $-I$ connected with $-V$ at the sample's electrodes.

2.3 Polarization measurements

In the present work, charge and polarization were measured by *Keithley 6517B* electrometer. The measurements are performed using the built-in electric current integration with respect to time. Thanks to electric circuit-based operation, such integration is less noisy compared to manual current integration. The sample is connected to the "Triax Input". Charge (Q_s) measurements based on the current integration method – a known capacitor (C_f, high accuracy) is placed in the feedback loop of the input amplifier, so the voltage developed across it (V) is proportional to the integral of the input current:

$$V = \frac{1}{C_f}\int_0^\tau I dt = \frac{Q_s}{C_f} \ , \tag{2.9}$$

where τ is a time constant. So

$$Q_s = V \cdot C_f \tag{2.10}$$

Sample's polarization obtained as

$$P_s = \frac{Q_s}{S_e} \ , \tag{2.11}$$

where S_e is an electrode's surface.

2.4 Voltage measurements

Voltage was measured by *Keithley 6517B* electrometer in the open circuit configuration as for the charge measurements discussed above. As a voltage can by digitized directly (by ADC) it requires no additional pre-conversion step (as for charge measurements), so it passes by the input buffer, amplifier and eventually gets treated by ADC. In this work the voltage was measured as a function of time (during light pulses) and versus light intensity (intensity sweeps).

2.5 Current measurements

Currents (under biases up to $20V$ and as a function of time during light pulses and for light intensity sweeps) were measured by *Keithley 2614B*[*] in pseudo four-probe configuration and for biases above $20V$ – by *Keithley 6517B* in current mode.

[*]Higher sensitivity and speed, allows also four-probe configuration. These benefits are useful for current versus light intensity measurements (especially in depolarized state), see Chapter 4.

2.6 Ferroelectric loops measurements

Ferroelectric properties of materials are of great importance for technological applications and for fundamental material research. The renewed attention to photovoltaic effects in ferroelectrics in solids has reinforced interest in the scientific community for ferroelectric and electric polarization measurements and their dependence on light excitation. As a consequence, an increasing level of attention should be paid to ferroelectric measurements and their integration with light sources. Although professional Sawyer-Tower[158] circuit-based AC ferroelectric measurement units are available on the market, their usage for light dependent ferroelectric studies is difficult, because it is necessary to trace the loops in a DC quasi-static way; i.e., by means of an ultra-low frequency measuring signal. This is due to the fact that a progressive structural damage (ferroelectric fatigue) may occur when a sample is subjected to cyclic AC electric field application and this can change strongly the PV. Moreover, for real PV cells there is a need to understand slow dynamics first before moving to fast excitations. The aforementioned aspects therefore make quasi-static ferroelectric measurements extremely attractive for opto-electric investigations. Simple circuits of quasi-static loop tracers have been known for a long time [159–161]. However, the more general use of these circuits is limited by the difficulties generated in compensation of electric leakage and linear components of capacitance as the ferroelectric loops are recorded. The proposed compensational circuits are often complicated and refer rather to ferroelectric loop analysis than to current voltage curves that provide more complete information about the insulating properties of the samples under electric fields. In this regard, we used a home-made straightforward DC ferroelectric test unit that utilized the commonly available Keithley 6517A electrometer easily integrated with set of LED light sources of different wavelengths. A more convenient mathematical way of calculating both the electric leakage and linear capacitance compensation can be used. Besides the ultra-low frequency operation important advantage of the system is also that it can be used for so called "Positive up negative down" (PUND) method for determination of ferroelectric switching, if FE is in doubt.

2.6.1 Electric leakage compensation

The undesired imperfection of some dielectric materials is known as electric leakage. It is the result of a dielectric material not being a perfect insulator and having some non-zero DC conductivity, allowing leakage current to flow, slowly discharging the capacitor. This bad insulator behaviour naturally reflects itself in the increment of the current value as a function of the applied electric field, while no current flow is expected for a good insulator (Fig. 2.5).

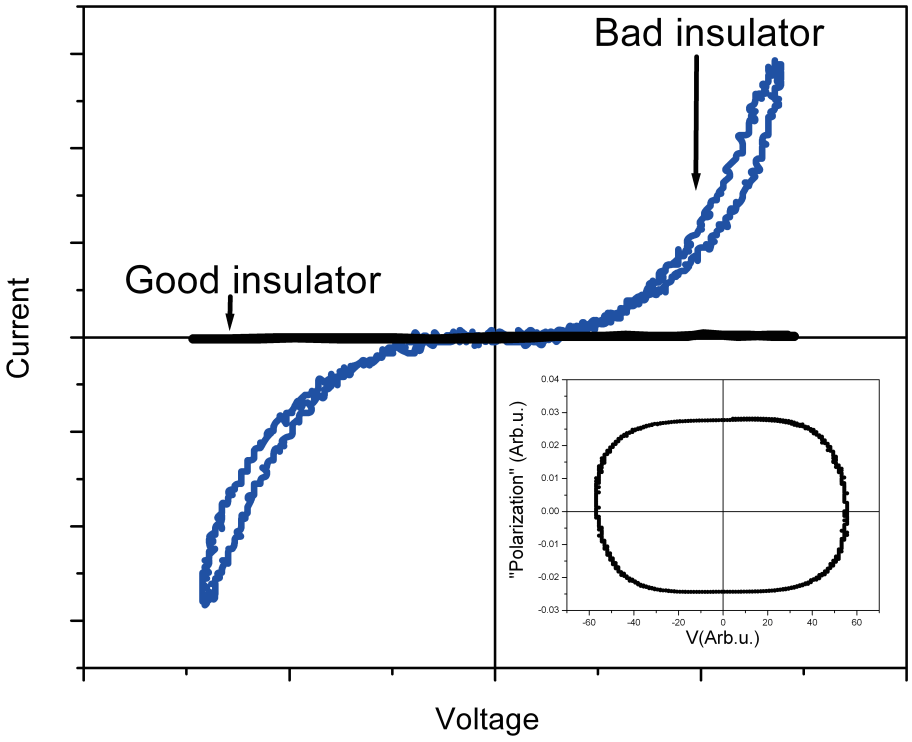

Figure 2.5: Example of the I-V characteristics recorded for good insulator and electrically leaky dielectric material. Inset shows the result of the P-V curves of the bad insulator.

The integration of the curves with respect to time is the ferroelectric hysteresis shown in the inset in Fig. 2.5. In ferroelectric materials, however, an additional contribution to the current (a peak) is expected to arise from electric dipole (charge Q) movement:

$$i = \frac{1}{R(V)}V + \frac{\delta Q}{\delta t}, \tag{2.12}$$

where R is resistivity, V is applied voltage. This ferroelectric contribution to the non linear leakage current gives a typical lossy uncompensated ferroelectric I-V characteristic, shown in Fig. 2.6.

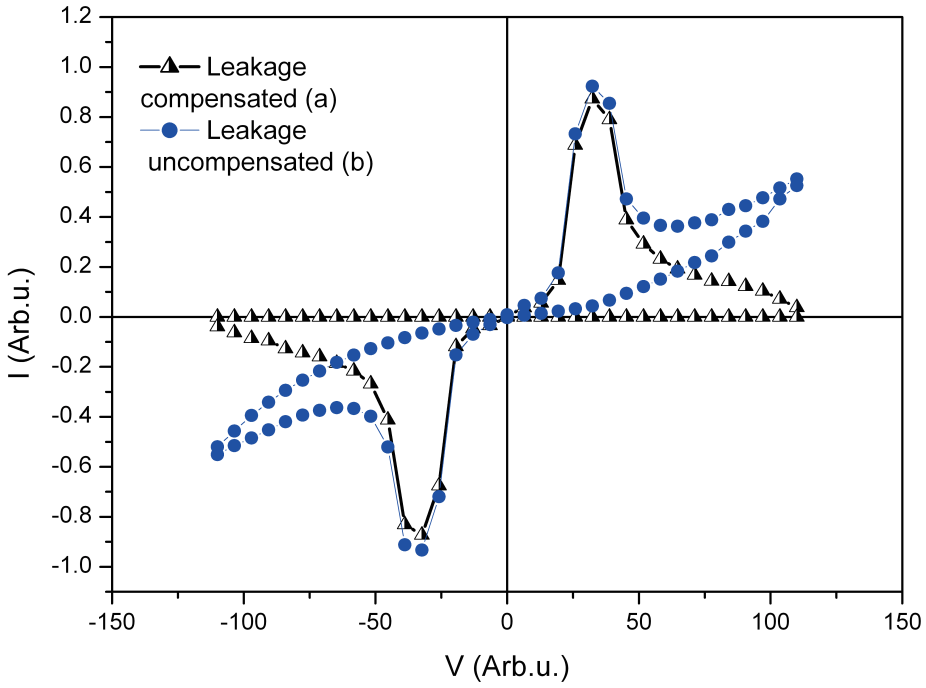

Figure 2.6: Example of the I-V characteristic recorded for electrically leaky ferroelectric material and same I-V curve after the leakage subtraction.

The result of current integration with respect to time gives rounded, ferroelectric-like hysteresis shown in Fig. 2.7. It has to be noted that I-V characteristic in Fig. 2.6 represents the model of a very first loop taken for non-single domain ferroelectric sample. Indeed, if the electric field is applied stepwise in a parallel direction of the forced polarization (sample is already polarized) no switching ferroelectric current is observed in this direction.

Consequently, additional cycle has to be taken, to present the two consecutive peaks in the positive and negative voltages. This is a base for so called "positive up, negative down (PUND)" method to verify FE in doubted samples. This effect may also be used to determine the leakage current background. As one can see the electric leakage manifestly increase both the apparent coercive fields and apparent remanent polarization. In order to avoid the leakage current contribution additional DC conductivity compensating circuit should be added to the electric circuit[159]. Alternatively, and more easily one can propose the simple subtraction of background

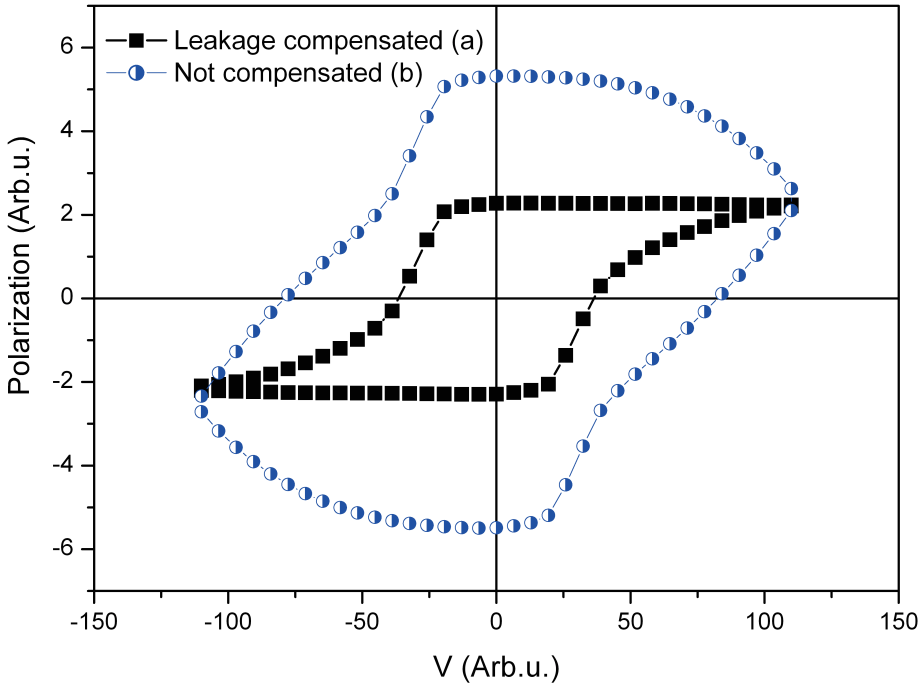

Figure 2.7: Electric leakage – compensated (a) and uncompensated (b) ferroelectric hysteresis obtained as a result of the I-V curves integration shown on Fig. 2.6 (see text).

leakage current from the I-V curve as shown on Fig. 2.6. The application of this procedure gives a nice looking saturation ferroelectric loop that is also shown on Fig. 2.7 for comparison.

2.6.2 Capacitance compensation

To measure the ferroelectric loop, the sample is placed into an electrical circuit of the DC electrometer together with its electrical wires. If the capacitance of the sample is smaller than or equal to the parasitic capacitance of the electrical circuit, the parasitic capacitance should be taken into account when considering the ideal circuit elements. Such situation might happen when too many wire junctions are used (case of cryostat) and so on. This extra capacitance usually has detrimental effects on the operation of "real-life" circuits, changing the shape of ferroelectric loop, therefore also requiring compensation. Additionally, due to the parasitic capacitance, the dipole reversibility time may vary, consequently affecting both light induced and time-dependent polarization studies. The latter effect can be minimized, excluding wire contributions, by the application of the four contacts method that is often used for precise capacitance measurements. The presence of the parasitic capacitance reflects itself in the shape characteristic of both I-V and ferroelectric loops, as shown in Fig. 2.8. The equation describing this can therefore be written as:

$$i = C\frac{\delta V}{\delta t} + \frac{\delta Q}{\delta t} \tag{2.13}$$

As one can see from Fig. 2.8, the parasitic capacitance largely decreased the apparent coercive fields and can be successfully removed (by subtracting linear capacitance background (Fig. 2.8)) with this straightforward approach.

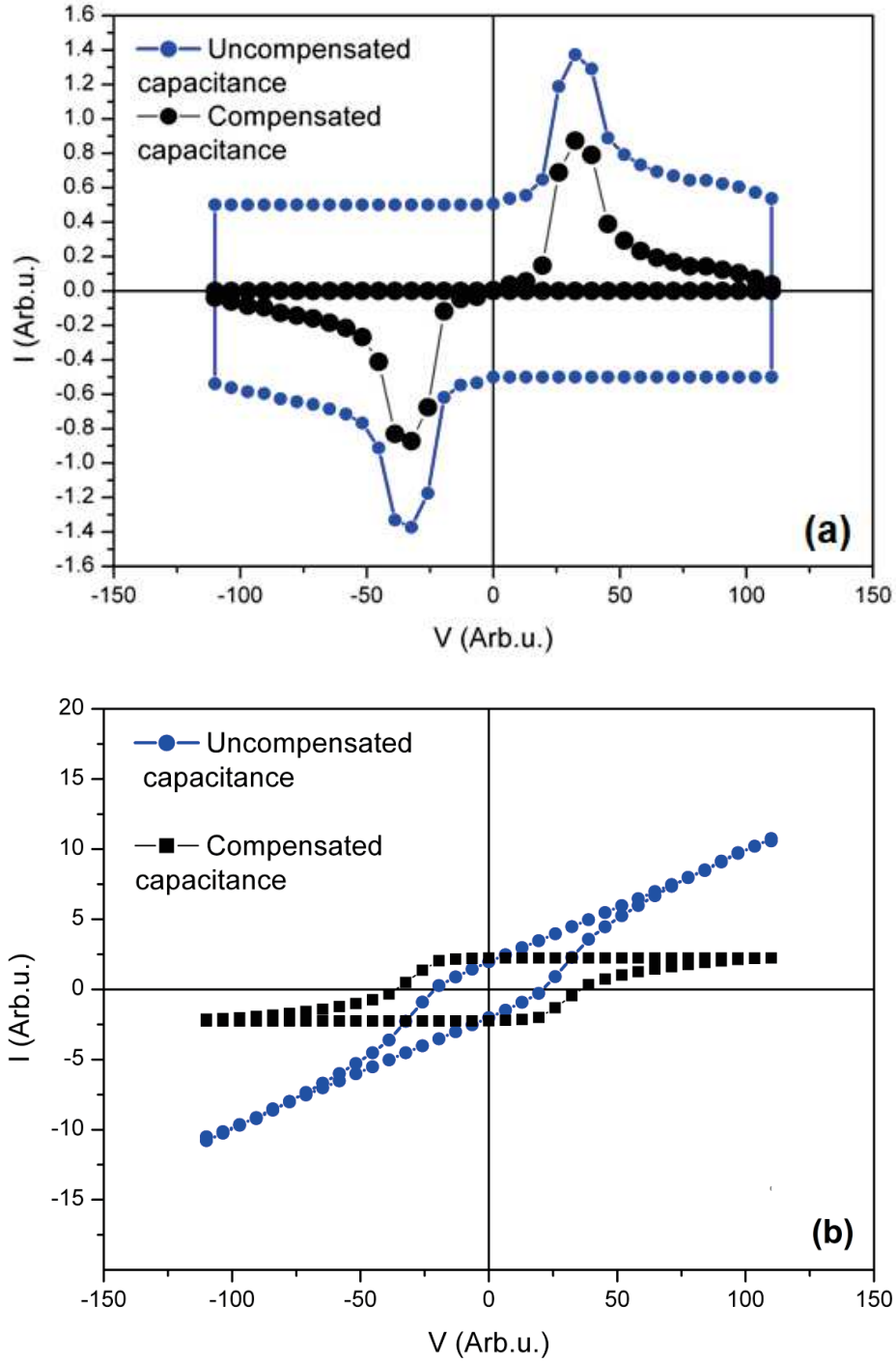

Figure 2.8: Example of the I-V characteristic recorded on a background large linear capacitance contribution before (a) and after (b) capacitance compensation.

2.6.3 Combination of both electric leakage and parasitic capacitance contributions

In the real samples the both aforementioned contributions: leakage and parasitic capacitance at the same time can be present. The basic equation describing parasitic capacitance C_P and electric leakage contributions therefore is written as follows:

$$i = \frac{1}{R(V)}V + C_P\frac{\delta V}{\delta t} + \frac{\delta Q}{\delta t} \tag{2.14}$$

Figure 2.9 and Fig. 2.10 show such artefacts via uncompensated I-V curve (blue line) which results in an uncompensated FE loop with wrong coercive field and saturation polarization. After compensation the both values are corrected (black lines). Although the both loops in Figure 2.10 show ferroelectric-like hysteresis, the contributions of parasitic capacitance and electric leakage current are clearly seen on their I-V plots. Therefore, the parasitic contributions may be successfully removed by numerical compensations approach.

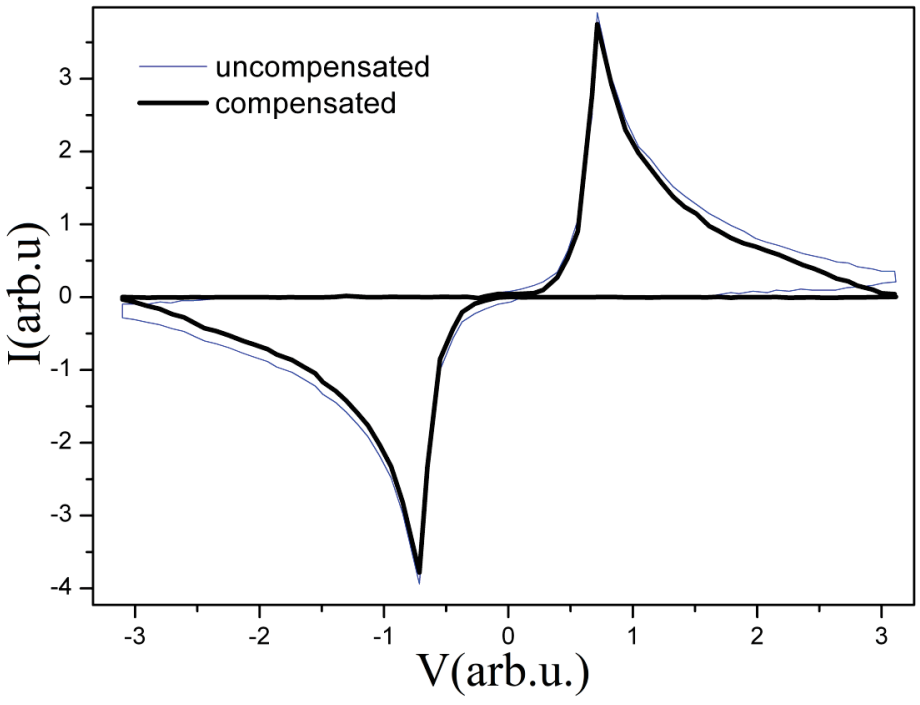

Figure 2.9: I-V loops: illustration of presence of both parasitic contributions (parasitic capacitance and leakage current).

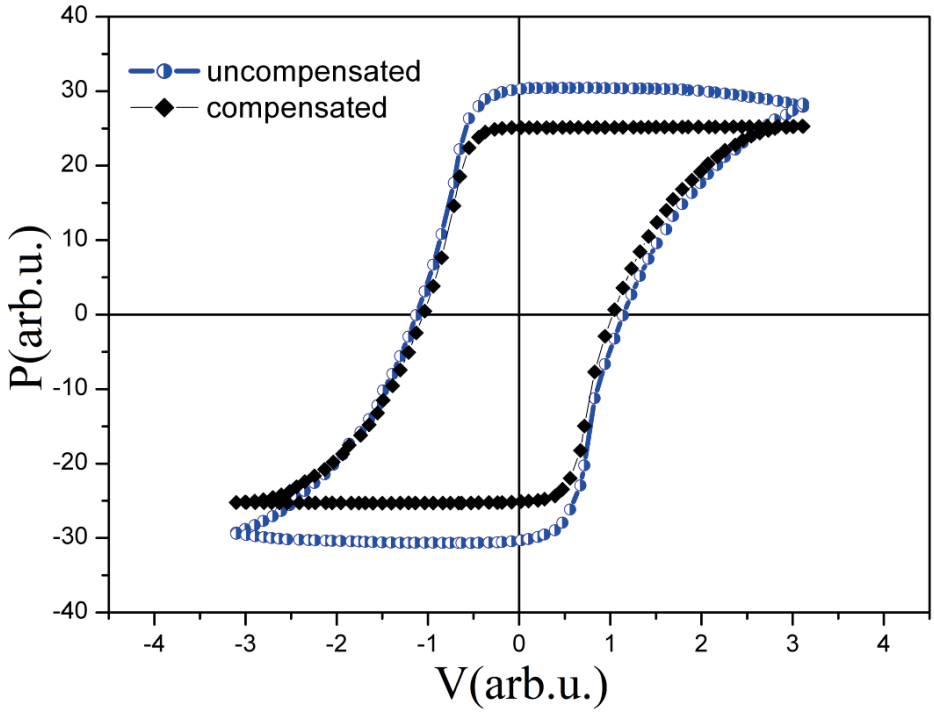

Figure 2.10: Uncompensated (a) and compensated (b) ferroelectric hysteresis loops obtained from the I-V curves (Fig. 2.9) integration with respect to time.

2.6.4 Sweep rate dependence of the FE loops

The ferroelectric coercive field and remanent polarization are the most important parameters characterizing FE material. Therefore their determination is crucial for the field of ferroelectrics. Unlike for ferromagnetic loops in magnetism, these basic characteristics can involve artefacts as was shown above and, therefore, a careful verification of measurements using the both extrinsic and intrinsic parameters must be taken into account. In addition, to these issues the one more intrinsic parameter is an electric field change rate (frequency), because to measure FE loop the electric field is applied to the sample at a certain rate. To minimize its energy the FE sample in as-prepared state favours configuration consisting of domains, where each domain can have a different polarization direction. Under such conditions, as it will be shown in Chapter 3 the light-induced charge generation will be also affected. When the external electric field is directionally applied, these domains start to align along this direction, new domains nucleate and grow. Consequently, the shape of the FE loop should be strongly influenced by the domains motion and depend on the measurement frequency. Because of the existence of these electrically inhomogeneous regions (FE domains) in the sub-coercive region and atomic movements at over-coercive one, the response of the system may occur at different time scales. Moreover, this electric-field-induced change dynamics can take place on a general background of undesired insulating imperfection (free charges) in the sample volume. In this situation understanding how the sweep rate influences the electric-field-induced polarization reversal is very important. Furthermore, in a view of recent results on photovoltaic properties development in FE, it becomes technologically important to know how long the system stays in the electrically excited state as it can strongly influence its PV performance. Figure 2.11 illustrates FE loops taken for the PMN-PT30% at different speeds of electric field cycle.

A clear effect of the frequency can be seen, although we remain in the limited ultra-low frequency region. The both ferroelectric coercive field and remanent polarization are strongly affected. To ensure recovery of the initial polarization state the same pre programmed de-polarization procedure with the time profile (shown on Fig. 2.12) has been applied to the sample before each sequential FE loop measurements. As the measurement frequency increases the apparent FE P_R values increase for both negative and positive poling. The extracted apparent increase in the values of the remanent charge (polarization) depends linearly on the time step (duration of each

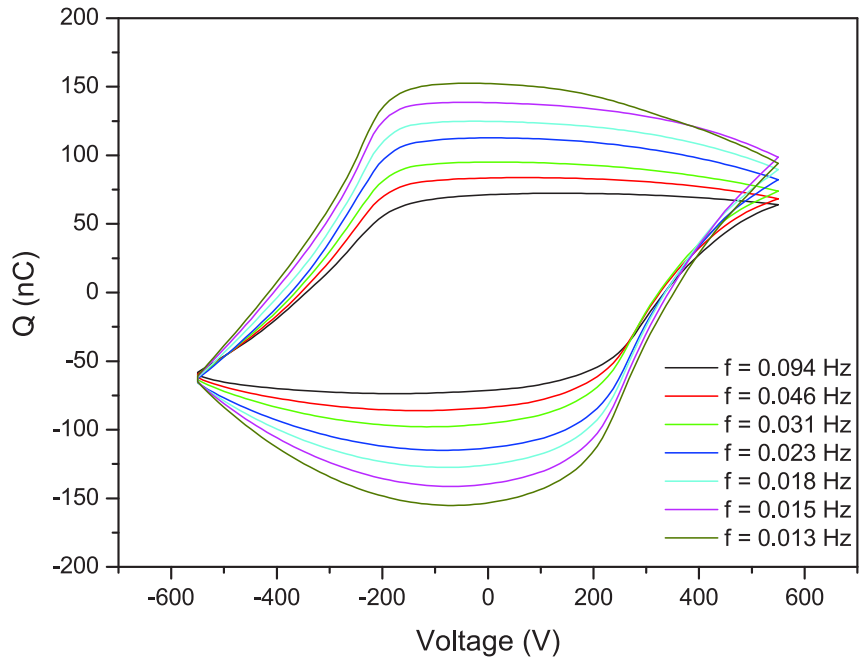

Figure 2.11: Ferroelectric loops of the PMN-PT30% crystal measured for different frequencies. Each FE loop was measured after the same de-polarization cycle.

consecutive voltage application, so $\sim 1/x$ for the frequency) for both negative and positive polarizations (see Fig. 2.13).

Indeed, this behaviour is comparable to the effect of leakage current (Fig. 2.7) on the both FE coercive field and remanent polarization. The longer our sample stays at each applied electric field the more free (background) charges flow and lead to modification in the basic FE loop parameters as the charge it is a current integration whatever its origin. The same type of dependence (linear for duration at each electric field and $\sim 1/x$ for sweep rate), is also observed for the negative values of the FE coercive field versus frequency (Fig. 2.14(a)). However, the frequency dependence is different for the positive values of the coercive FE field, because of FE loop asymmetry (Fig. 2.14(b)). It reveals the two regimes: the low frequency regime leading to the decrease in FE coercive electric field and high frequency regime leading to increase of FE coercive electric field. This behaviour can be understood via the different type of domain wall motion. Unlike larger frequencies, in the quasi-static regime (lower frequency region) the domain walls have time to relax, possibly due to free charges in the samples and

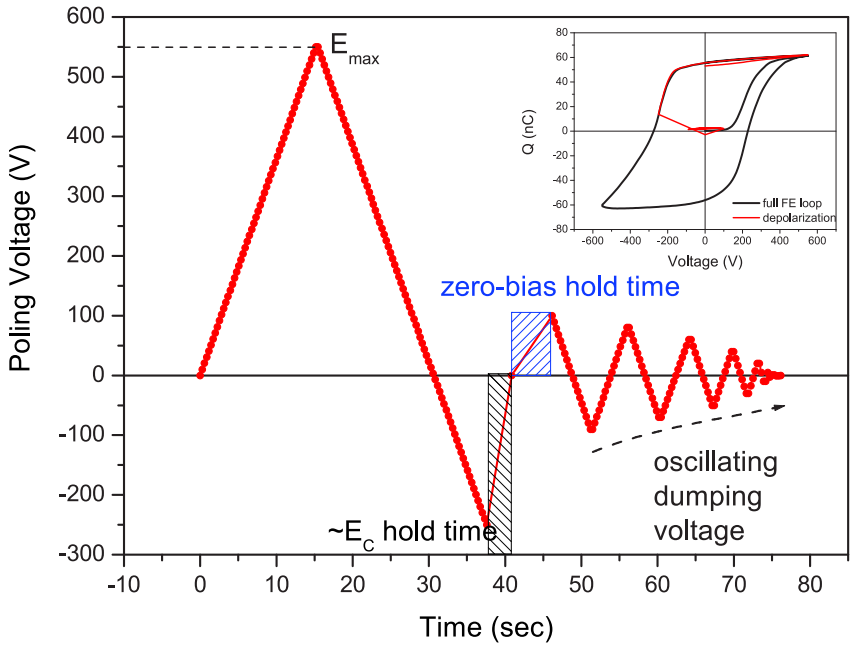

Figure 2.12: FE sample de-polarization profile. Inset shows a corresponding FE loops (full loop is black, de-polarization one is red) with a final polarization close to 0C. Thus proving high efficiency of this method.

therefore electric field needed for domains reversal increases as measurements become slower [162–166].

The deeper analysis of this phenomenon requires larger frequencies[167] and is out of the scope of this thesis because of a DC regime PV cells operation. Never the less, taking into account the above considerations, the FE loops in this thesis were measured at the same frequency in darkness and under light excitation to have the same "background" contributions for the both cases. In the light of the above-mentioned, it is clear that a proper frequency window must be found in order to find a balance between good-shaped FE loop preferring high frequencies and light induced charge generation which may be generally slower. To minimize leakage the FE loop was measured at fastest possible frequency of our set-up ($f = 0.094$ Hz). Because photovoltaic properties are about the free charge generation, the quasi-static technique of FE sample characterization is more appropriate here.

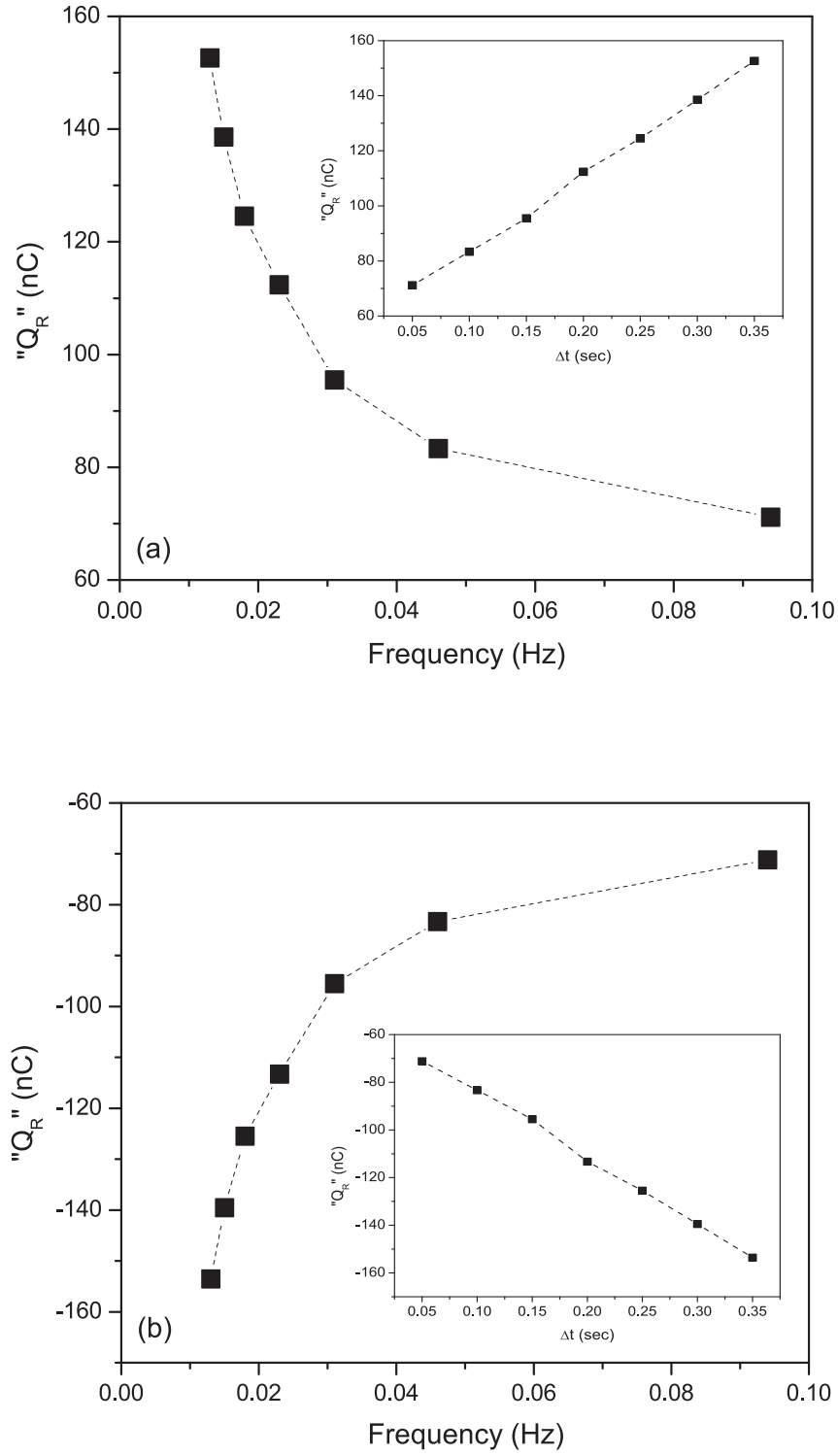

Figure 2.13: The frequency dependence of the apparent values of the remanent charge extracted from the Fig. 2.11 for both positive (a) and negative (b) poling.

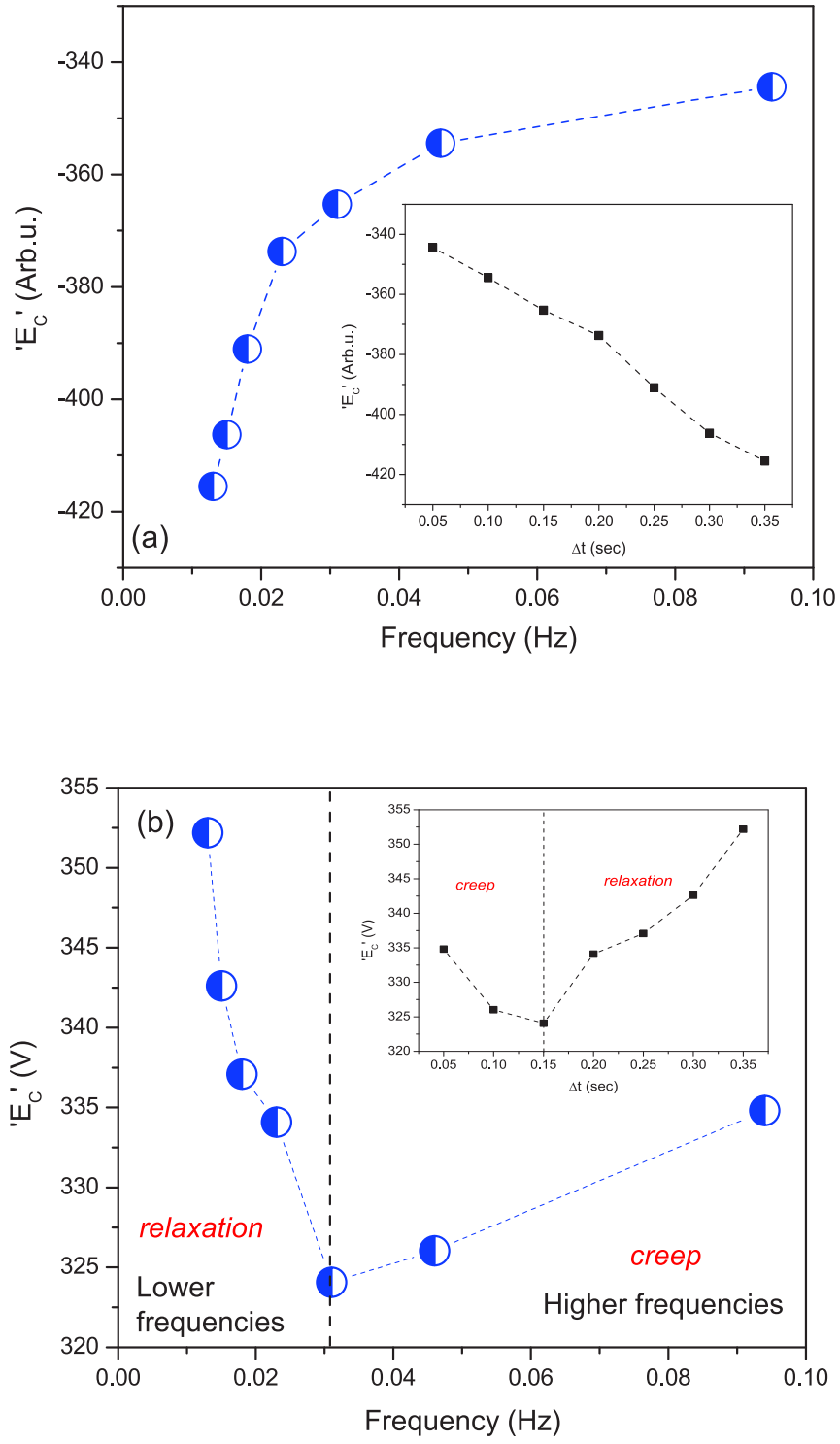

Figure 2.14: The frequency dependence of the coercive field values of the remanent charge extracted from the Fig. 2.11.

2.6.5 Conclusions

While electrical polarity (acentric structure)[168] is required for the BPVE, the polarity alone, does not yet guarantee ferroelectricity and therefore an electric tunability of the PV effect. The ferroelectricity itself is often difficult to demonstrate experimentally[169]. For example, the reversibility of the electric dipoles could require bigger electric fields than the breakdown field, or it might be due to asymmetric, irreversible arrangements of the atoms. Without ferroelectricty the electric field induced tunability is very limited or unstable. Moreover, a repetitive electric field cycling can lead to progressive electrical damage of the sample and modify PV response. Therefore the proper, fatigue-free FE characterization is a key. That is why in this thesis the DC ferroelectric test unit was used. As it was illustrated above, even small, uncompensated electrical leakage and parasitic capacitance may lead to large errors in ferroelectric hysteresis observation. Another important advantage of this technique is a more accurate, simple, numerical compensation for parasitic capacitances and leakage current which substitute complicated electrical circuits in conventional FE loop tracers. Then FE loop is measured under light excitation, the frequency dependent studies suggest a high dependence of the PV effect on the electric field speed, whereas a slow dynamics must be revealed first before moving to higher frequencies. The FE loop under light may experience qualitatively similar form to the one obscured by background free charges, therefore it must be measured at the same frequency in darkness and under light. From the above-mentioned, it is clear that a proper frequency window must be found in order to find a balance between good-shaped FE loop preferring high frequencies and light induced charge generation which may be generally slower. All these effects are particularly important to be taken into account when FE sample is excited by light and clear distinguishment between leakage currents and photovoltaic charge generation is required.

2.7 Deformation measurements

Because FE have also piezoelectric properties and the PMN-PT crystals investigated here are used in piezoelectric elements, it was decided to examine a deformation control over the reported PV effect. The simplest and less invasive technique of strain measurements is one that uses the *strain gauge* (Fig. 2.15) – metallic grid that changes its electrical resistance in proportion to the amount of strain experienced by the sample. A principle – dependence of the material's electrical resistance on its geometrical shape:

$$R = \rho \frac{l}{S} \ , \tag{2.15}$$

where R is the resulting resistance, ρ – material's resistivity, l – length (distance between contacts) and S – cross section. Any deformation of the material modifies these three parameters. As a result resistance changes (see Figure 2.16). This relative change could be expressed as:

$$\frac{\Delta R}{R_0} = \frac{\Delta \rho}{\rho_0} + \frac{\Delta l}{l_0} - \frac{\Delta S}{S_0} = (1 + 2\nu + \pi\varepsilon)\frac{\Delta l}{l_0} = G\frac{\Delta l}{l_0} \ , \tag{2.16}$$

where ν is a Poisson's ratio, π – piezo-resistive coefficient, ε – Young's module and G – gauge factor (tabular value for each material/alloy and geometry). For sensors used in this work $G = 2.08$. By fixating this grid to the sample by means of a special cements, glues and epoxies (sensor glued on top of the PMN-PT sample, see Figure 2.17) a good deformation transfer is achieved.

As strain is defined as $\frac{\Delta l}{l_0}$ its unit is "meter per meter". The other commonly used unit is "microns per meter" ($\mu m/m$):

$$1\,\mu m/m = 10^{-6}\,m/m \equiv 1\,ppm, \tag{2.17}$$

where *ppm* stands for "part per million".

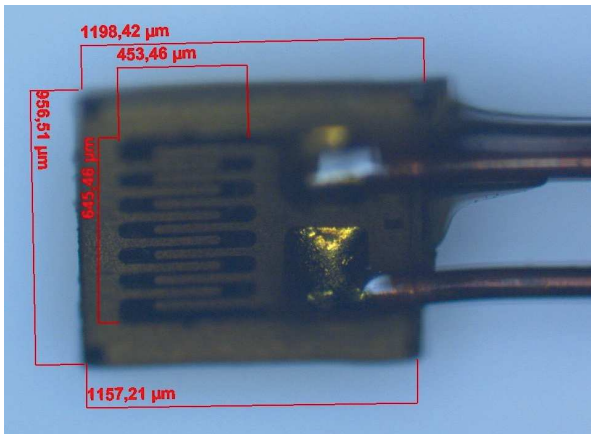

Figure 2.15: Strain gauge.

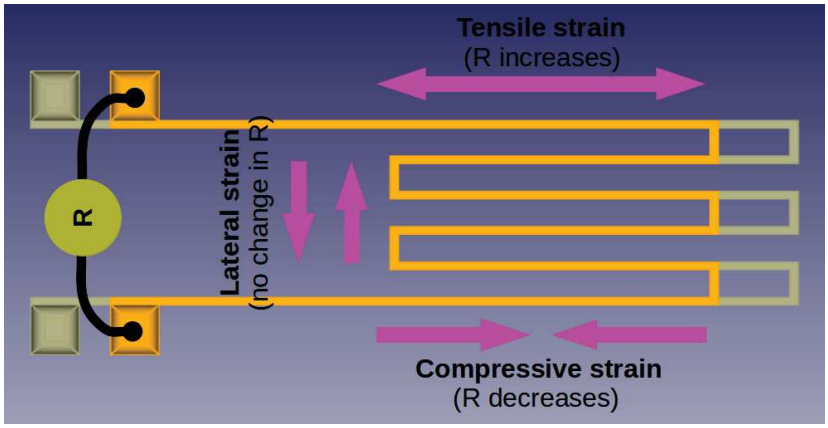

Figure 2.16: Strain gauge schematics. Tensile strain leads to increase in gauge resistance while compressive one decreases it. Contribution of lateral strain is negligible in this configuration.

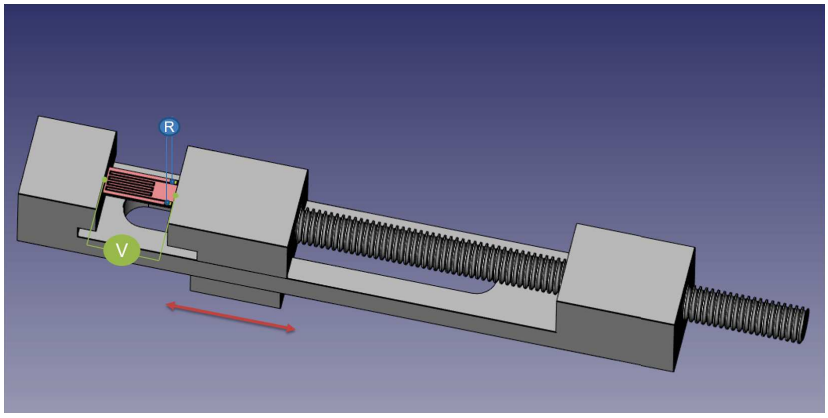

Figure 2.17: Photovoltaic effect under compressive strain measurements.

2.8 Characterization of light sources

Light intensity was controlled using the *Thorlabs DC4100 LED Driver* connected to PC. As neither hardware, nor official software doesn't support the intensity control in power units (controls only current – primary and brightness – secondary options) each LED must be calibrated prior to measurements. The calibration process is an intensity measurements (by *Thorlabs PM100 Power Meter* with *S120VC* silicone photodiode (extended to UV) adjusted to the right wavelength) for each current value from 0 mA to 700 mA with a fixed increment. The linear approximation gives a calibration equation. Intensity is calculated as a power divided by the beam's cross section at a given distance from the fiber ending.

One more problem arises from dealing with "real" LEDs (with pulse profile showed in Fig. 2.18) rather than "ideal" ones giving a perfectly rectangular-shaped pulses ($\bar{\tau}_{rise} = \bar{\tau}_{fall} = 0$, switch is instantaneous). As in this case the LED's rise/fall time becomes crucial when dealing with intensity sweeps. If the sweep frequency is too high (grater than $1/\bar{\tau}_{rise}$ for increasing intensity or $1/\bar{\tau}_{fall}$ for going back to 0 mA) – the LED and controller circuit doesn't have enough time to supply the requested intensity and the results will be erroneous. In the present research the 365 nm (central wavelength) LED was used for the light intensity sweeps. Its characteristic rise times were measured[†] for the step-like intensity profile formed with pulses of equal duration and intensities going from 50 mA to 700 mA (maximal supply current for this LED). The resulting plot is showed in Fig. 2.19. At currents up to 650 mA rise times are almost the same and yield the mean value of $\bar{\tau}_{rise} \approx 0.13$ sec. However, as it can be clearly seen, at higher currents (650 and 700 mA) this time becomes ≈ 4 times grater. This could be explained by the fact that to stabilize higher currents, LED driver circuit (constructed as a PWM-driven voltage-to-current converter with negative feedback loop) needs more time due to the OpAmp gain, required number of PWM periods, smoothing factor, and circuit's and wires' capacitances.

This behaviour is confirmed by fixing the baseline current to 650 mA and making pulses of additional 50 mA (see Fig. 2.20). In this configuration the rise and fall times becomes the same and slightly lower than above-mentioned mean rise time.

[†]Power was measured as a function of time while performing the light pulses. Time constant was ≈ 0.03 sec.

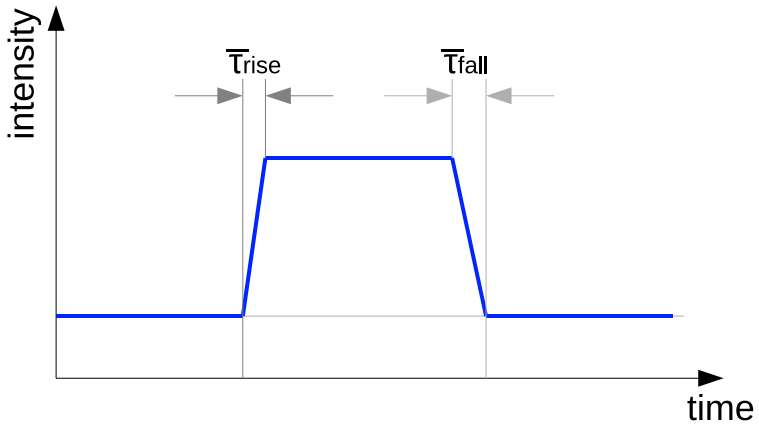

Figure 2.18: Schematic of "real" LED pulse intensity change over time. It demonstrates the presence of rise and fall times related to the LED and its driver functioning.

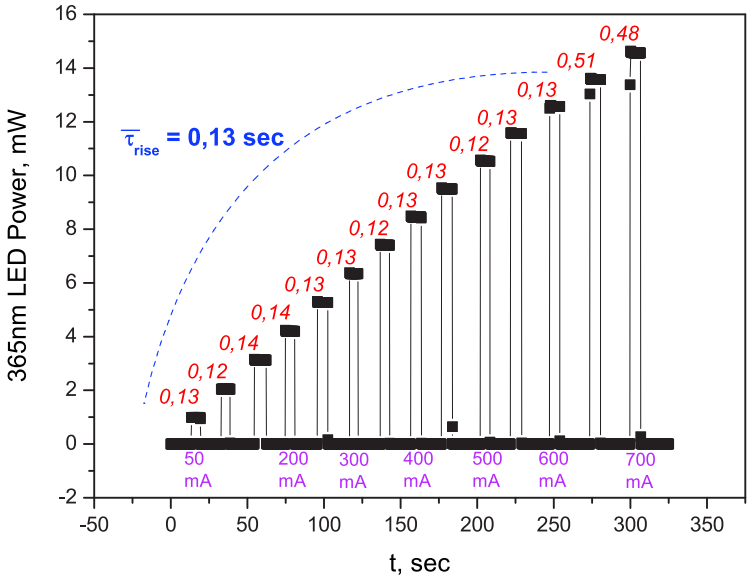

Figure 2.19: 365 nm LED rise time characterisation for a whole current range with 50 mA step.

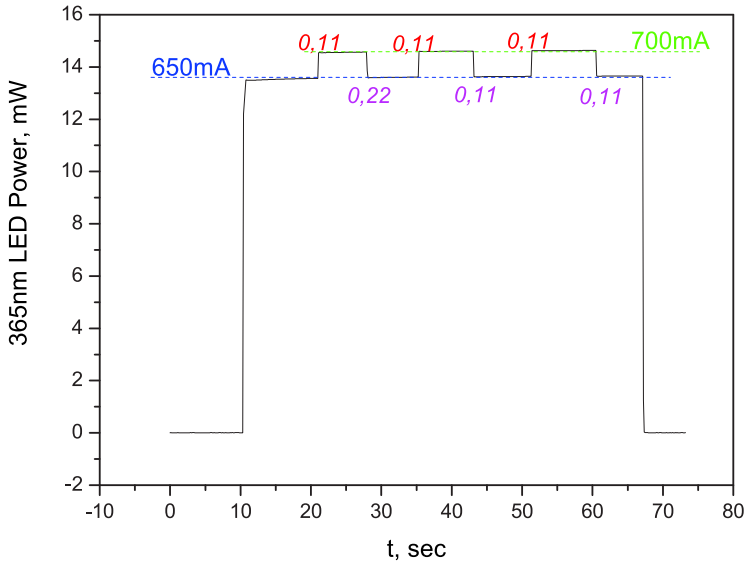

Figure 2.20: 365 nm LED rise and fall times measured for 50 mA current variation near its maximum.

2.9 Evaluation of sample heating due to light absorption

Since the light illumination can heat the sample (and possibly interfere with other measurements) one needs to evaluate the temperature change (exact value depends on light intensity, wavelength and sample's absorption coefficient). To give an answer to this question the wireless temperature measurements were performed with the *Therm-App TH* sensor (bolometer resolution 384×288 pixels) with the same illumination conditions. It can take an accurate temperature measurements and has a high sensitivity (NETD < 0.07°C). As a bolometer is only sensitive to the IR part of a spectrum (moreover, the corresponding IR filter is embedded into the final device by design) it becomes ideal for UV LED characterization, used throughout this thesis, as such configuration naturally eliminates the contributions of reflected and diffused UV irradiation. The results reveal that the maximal heating for both PMN-PT compositions is less than $1.9^{\circ}\,C$.

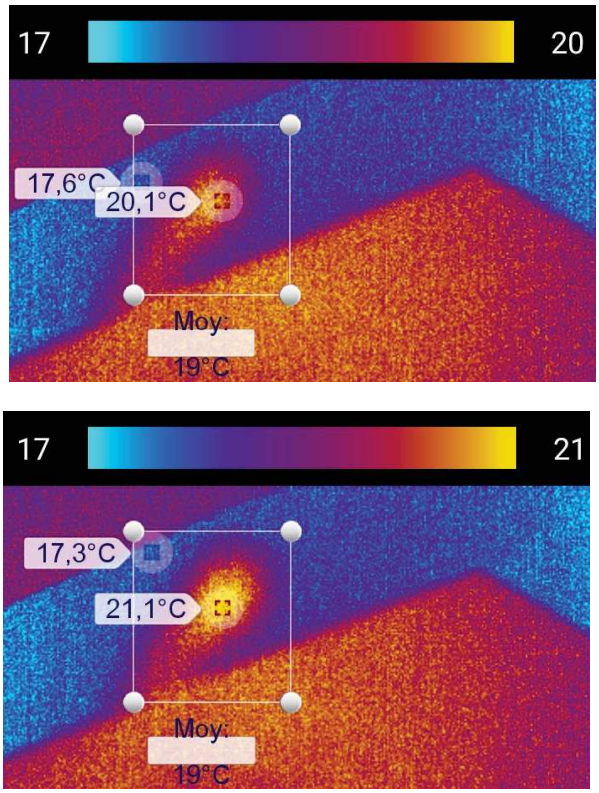

Figure 2.21: Sample's temperature in darkness (top) and under the constant 365 nm UV LED illumination (bottom) with focused beam (diameter $\approx$ 3 mm) of maximal intensity. Heating is evaluated to 1° K.

2.10 Quantum efficiency calculations

Quantum efficiency (or also known as *incident photon to converted electron ratio*) is one of the photovoltaic efficiency evaluation method. It is calculated as a ratio between the amount of photo-generated electrons to the number of absorbed photons of a particular wavelength:

$$\eta = \frac{n_e}{n_{ph}} \cdot 100\%, \tag{2.18}$$

The n_e can be measured as the sample's polarization change during the light pulse (see Fig. 2.22). The shape of a curve suggest the presence of the relaxations (time lags in the system's response): when the light pulse starts and ends – it takes some time for newly generated charges to distribute throughout the sample's volume, to form the screening layer and change the total polarization. In order to account for the "pure" generation stage the corresponding linear part is extracted (see the rectangle formed by ΔQ and Δt guidelines, in this case its diagonal will be the desired linear part). The charge variation ΔQ in this case is cased by the photons absorption during time Δt. So the number of photons absorbed by the sample in this case can be expressed as:

$$n_{ph} = \frac{P_s \cdot \Delta t \cdot \alpha \cdot \lambda}{hc}, \tag{2.19}$$

where P_s is a total light power on a sample (per second), Δt is the illumination time, α – absorption coefficient for the wavelength of interest (λ). And the corresponding number of generated electrons:

$$n_e = \frac{\Delta Q}{|e|}, \tag{2.20}$$

where $|e|$ is an elementary charge. So the final formula with pre-calculated values will be:

$$\eta\,[\%] \approx \frac{0.124 \cdot \Delta Q\,[nC]}{P_s\,[mW] \cdot \Delta t\,[s] \cdot \alpha\,[a.u.] \cdot \lambda\,[nm]} \tag{2.21}$$

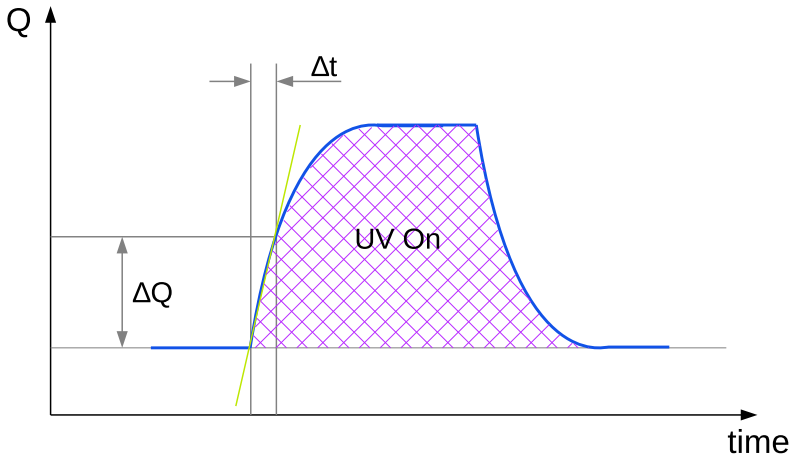

Figure 2.22: Schematics of the sample's charge change under above-bandgap light illumination.

2.11 Solar cell efficiency

The efficiency of a solar cell is determined as the fraction of incident light power which is converted to electricity:

$$\eta\,[\%] = 100\% \cdot \frac{P_{max}}{P_{in}}, \tag{2.22}$$

where P_{in} is the incident light power and P_{max} – the maximum power generated by the photovoltaic device. It can be extracted from the I-V curve, or calculated for a given FF (see below) and two characteristic points:

$$P_{max} = V_{oc} \cdot I_{sc} \cdot FF, \tag{2.23}$$

where V_{oc} is the open-circuit photovoltage, I_{sc} is the short-circuit photocurrent and FF – fill factor. It shows how close the maximum generated power (P_{max}) is to the theoretical one (P_{theor}, calculated as $V_{oc} \cdot I_{sc}$) and in this way it defines the quality of a photovoltaic device. Its value can be obtained from the I-V curve (see Fig. 2.23) like

$$FF = \frac{P_{max}}{P_{theor}} \equiv \frac{S_{max}}{S_{theor}} \tag{2.24}$$

Both η and FF characterize the solar cell power conversion efficiency and quality.

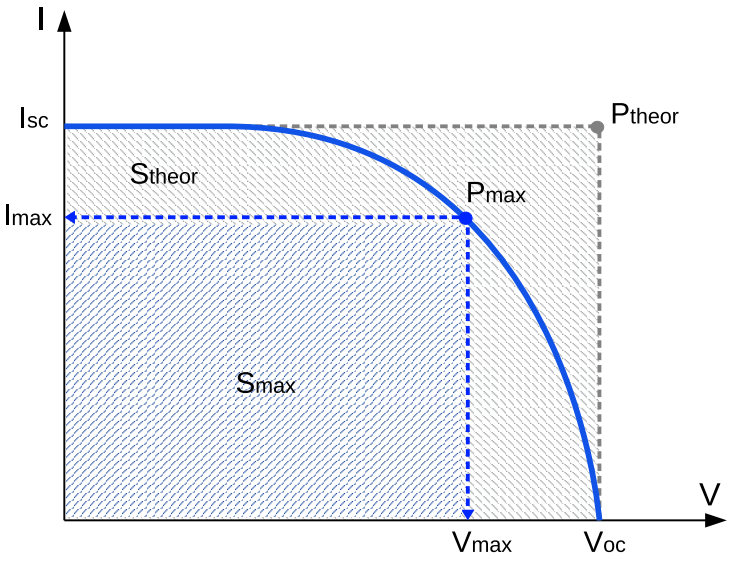

Figure 2.23: Schematics of the solar cell I-V curve under constant intensity illumination.

2.12 Sample preparation and characterization

Ferroelectric single crystals have been provided by *Crystal GmbH* (Germany) in the form of plates $10 \times 10 \times 0.3mm^3$ with [001] orientation and in a spontaneous polarization state. Top and bottom planes have been polished by a manufacturer with the laser. These plates were cut into smaller pieces of the desired sizes by using a diamond wire saw. Crystals' dimensions were measured with the *Axio Imager Microscope* (Carl Zeiss®) together with the AxioVision software. After being cleaned in ethanol, electrodes were formed on crystal's edges parallel to (100) plane by silver conductive paint (see Figure 2.24). With the same silver paste thin short (wire length affects the noise level) copper wires were attached to the formed electrodes. Other ends were soldered (largely improves the signal-to-noise ratio) to the wires with proper BNC-friendly connectors. Figure 2.25 shows the FE loop schematics with depolarized (here and after denoted as state "0") and two saturated states with opposite polarization – states "1" and "2".

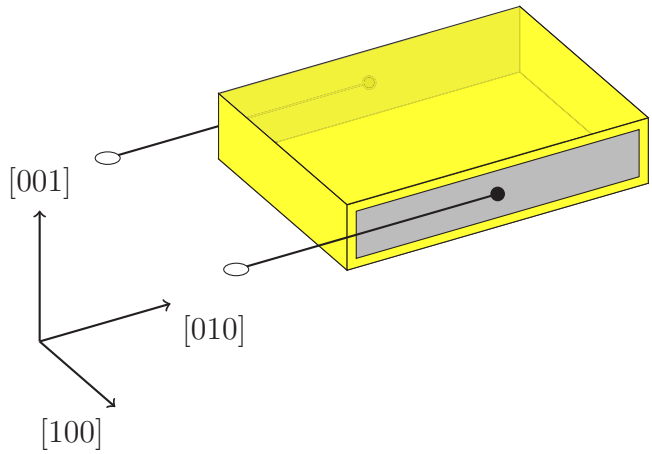

Figure 2.24: Measurements configuration.

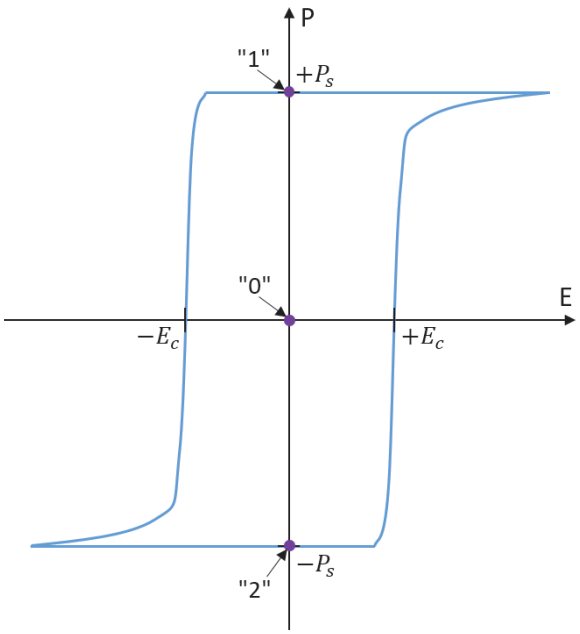

Figure 2.25: FE loop with polarization states notation used throughout this manuscript.

Chapter 3

Electrical control of photovoltaic effect

The ferroelectric materials can have multiple possible orientations of polarization vector (both length and orientation) – polarization states [170], that can be switched by external electric field. The possible orientations of the spontaneous polarization are multiple in sub-coercive region and generally depend on crystalline symmetry. Figure 3.1 schematically illustrates the possible spontaneous polarization states for tetragonal (a), orthorhombic (b) and (c) rhombohedral symmetries.

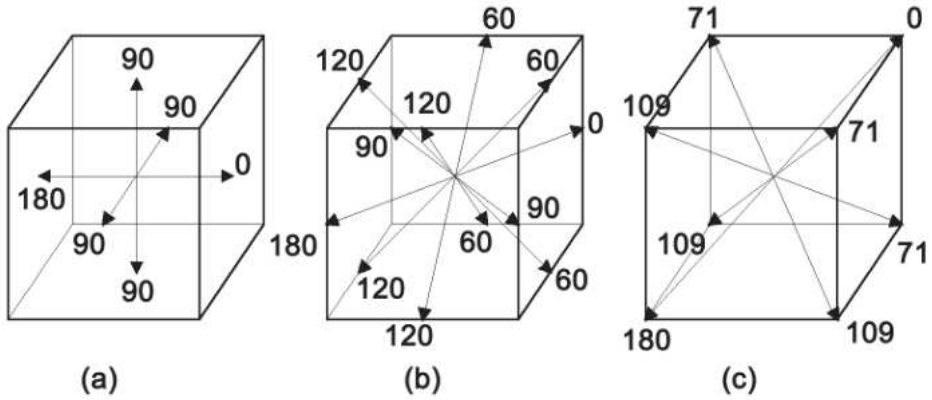

Figure 3.1: Possible directions of spontaneous polarization for the (a) tetragonal, (b) orthorhombic and (c) rhombohedral structures.

As it was already mentioned and will be shown below the photovoltaic efficiency (in terms of charges generation and separation) depends on the materials' intrinsic polarization state. Moreover all these structural particularities must be taken into

account during electrical poling. Therefore it is logical to assume that the strictly same poling procedure can result in different states if performed in different crystalline symmetries within the same FE compound.

Nevertheless, the 180 degrees polarization rotation at fixed temperature (same crystalline structure) should result in qualitatively same photovoltaic response because it results from symmetrical atomic displacement (see Fig. 3.2).

As it is illustrated by the above picture many different electric regimes have to be tested for the photovoltaic response modification. This chapter will show that it is indeed possible to have the photovoltaic properties modified for different electric states of the sample.

First of all the two states indicated as "1" and "2" corresponding to the remanent polarization states with opposite polarization will be examined and their photovoltaic performance will be also compared to the depolarization state for the both PMN-PT32% [001] and PMN-PT30% [001] single crystals.

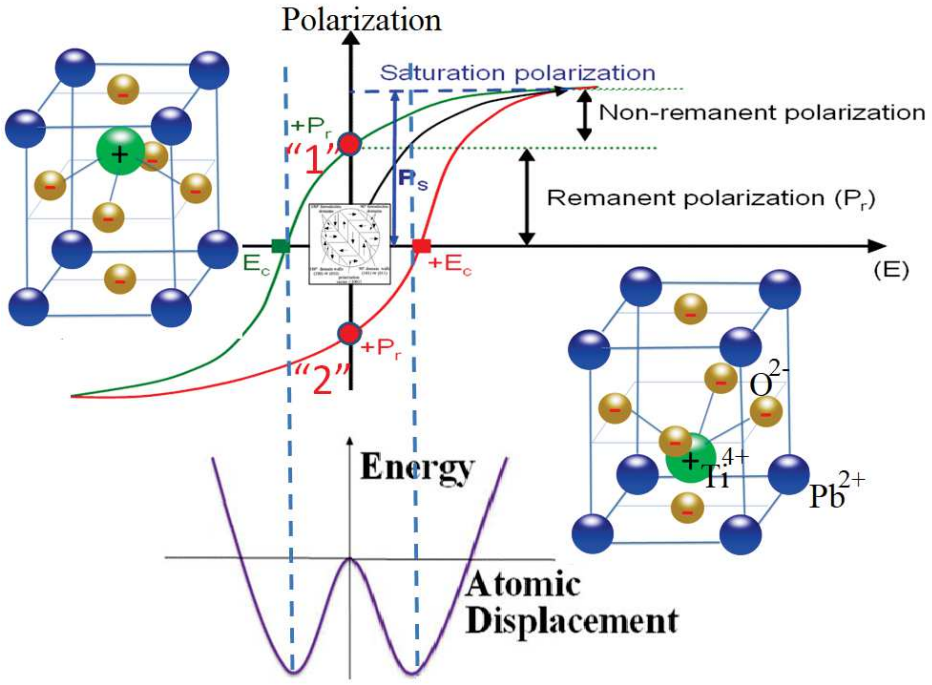

Figure 3.2: Ferroelectric hysteresis cycle and its different regimes with respect to electric field induced atomic movement.

3.1 Ferroelectric state dependence of photopolarization and photovoltage

3.1.1 The $Pb[(Mg_{1/3}Nb_{2/3})_{0.68}Ti_{0.32}]O_3$ (32%) single crystal

In PMN-PT family the spontaneous polarization oriented towards [111] (illustrated in Figure 3.3). However, for the sake of simplicity and for the reasons discussed previously (in chapter 2) the electric field poling and polarization/voltage/current measurements will be done in [100] orientation (see Figure 3.4).

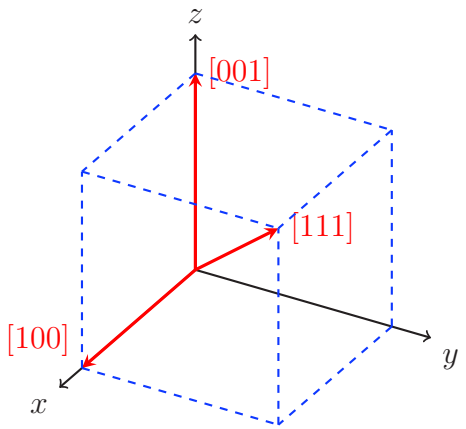

Figure 3.3: Spontaneous and poled polarization orientations.

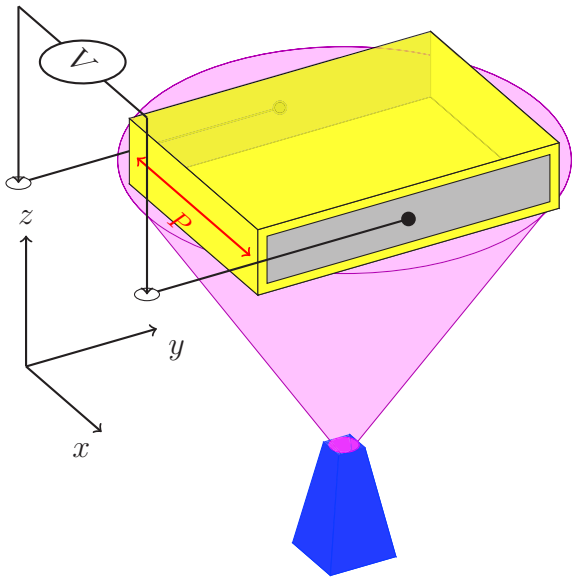

Figure 3.4: Experiment configuration.

The hysteresis loop of polarization versus electric field in this study is first taken at room temperature to verify ferroelectricity. The sample was afterwards irradiated with a 365 nm 13.67 mW LED in order to investigate the change in the FE polarization response. As this family is known to posses the pyroelectric properties[171–175] the temperature change of the sample under illumination should be taken into consideration. To be sure that changes in polarization/current are of photovoltaic origin the temperature of the sample was measured by a thermal camera under the maximum UV light intensity at 3 mm distance from fiber. The temperature profile suggests the maximum heating by 1.9 K under illumination. Then the same sample was putted into cryostat and heated by this amount and the recorded FE loop showed no noticeable difference compared to one at room temperature condition.

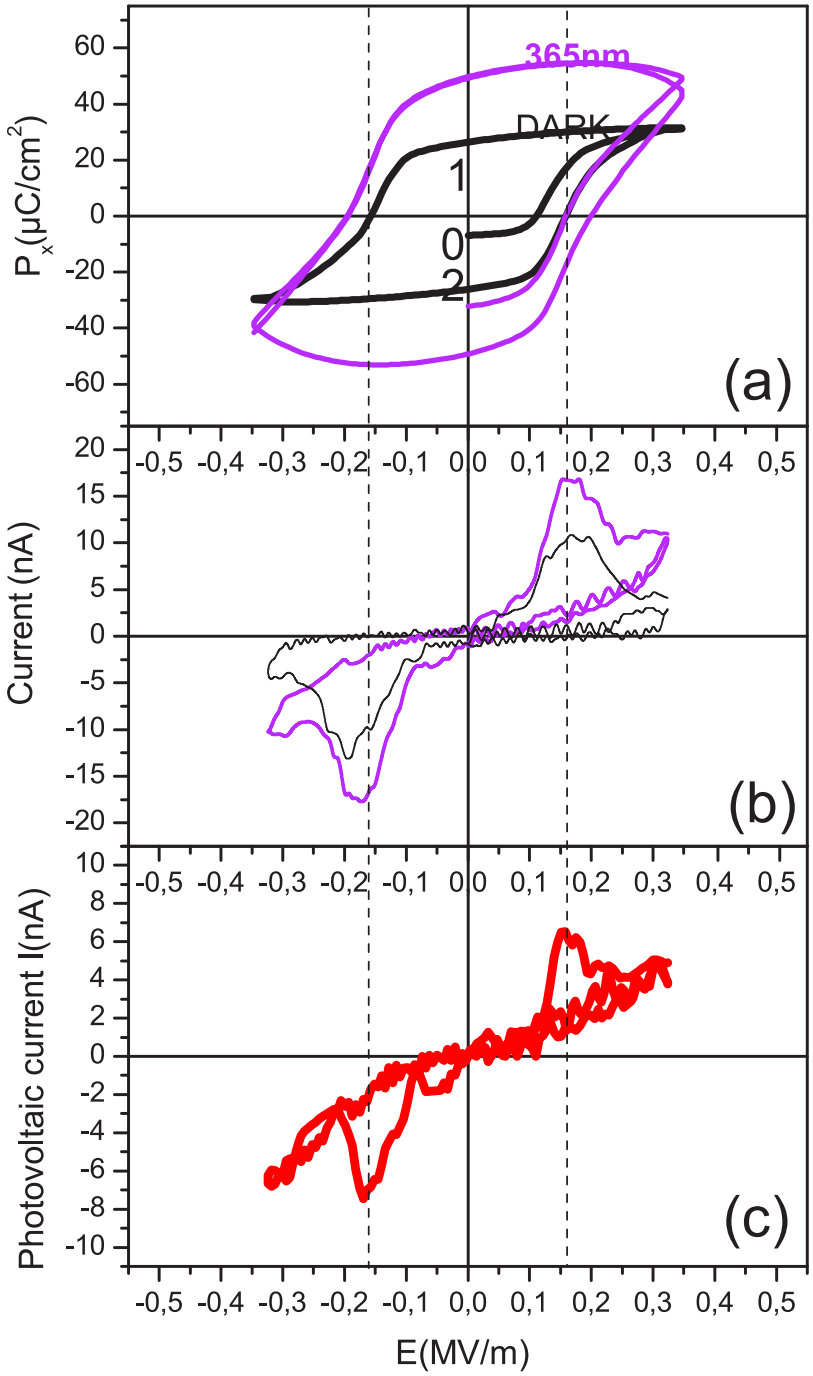

Figure 3.5: PMN-PT32% polarization (a), current(b) and photocurrent (c) measured in darkness and under UV light.

Figure 3.5 represents the FE properties of the sample under electric field applied along the [100] direction in darkness, and under illumination along the [001] direction. FE loop measured in darkness reveals a classical hysteresis with three polarization

states: initial spontaneous state (here denoted as "0") and two saturated states with opposite polarization ("1" and "2"). The literature suggest that by cycling the FE loops we introduce the defects into crystal[176–181] (leading to the "rounding" of the loop, increasing of coercive field, point defects relocation and eventually cracking) and at some point it becomes damaged. To know how many cycles our crystal can withstand the ferroelectric loop was recorded multiple times. As far as the sweep rate remains the same the ferroelectric loop showed no noticeable sign of fatigue at least up to ~ 20 cycles. This confirms the good quality of the FE crystal used in our research. Afterwards the FE loop was measured under illumination. The light irradiation induces a large change in the FE loop. The behaviour of the sample can be compared to the one discussed in the chapter 2.6. The sample becomes a leakier FE with an increase in both polarization and coercive field as illustrated in Figure 3.5(a). The FE loop under illumination (same compensation as for one in darkness) shows apparent polarization increase by a factor of ~ 4, but this is a result of the increased conductivity (the concentration of free carriers due to the photovoltaic effect). The observed light induced change in the ferroelectric loop largely exceeds the previous published results[68, 145, 182, 183]. The photo-carriers also contribute to the noticeable coercive field shift. This is better seen on the corresponding FE current in Figure 3.5(b). The pure photovoltaic current is the difference between those under the illumination and in darkness. Figure 3.5(c) reveals at least two important features. The first one is that the photocurrent, and therefore the bulk photovoltaic effect (BPVE), strongly depends on the FE state: the maximum of photocurrent is observed at the electric field corresponding to the FE dipole reorientation. The corresponding volt-ampere characteristics further illustrate the photo-induced change in electric properties Fig. 3.5(b). Such induced photocurrent should impact the remanent FE state as firstly reported by Iurchuk *et al.*[13].

The time dependence of the related photopolarization measured at the three states ("0", "1" and "2") shown in Figure 3.6 provides insight into the mechanism explaining how photopolarization properties relate to the ferroelectric state of the material. The sample was initially polarized positively (state "1"), by sweeping the electric field from -0.34 MV/m to $+0.34$ MV/m and to zero, and the polarization was then monitored during periodic illumination (at zero bias). The reduction of polarization is observed with the remanent effect. The illumination generates charges that distribute along the direction imposed by the sample's intrinsic electrical field (poling direction, [100]) decrease the intrinsic electric field of the material and hence the polarization. Note that

the decrease in polarization with zero bias should not be here confused for apparent increase of polarization in FE loop, where polarization has a contribution from Ohmic current integration under bias. The light effect in zero bias and light effect under electric field must be clearly separeted. The last one is obscured by photoconductivity (see background leakage contribution Fig. 3.5 and Fig. 2.6 (blue curve)). After turning off the light, charge trapping makes this decrease partly persistent (remanent effect, Figure 3.6) leaving the sample in a slightly reduced polarization state. Subsequent light pulses reveal only a transient (reversible) effect as they are of the same energy and the remanence was previously achieved.

Notably, the initial polarization state can be recovered electrically by bringing the ferroelectric system back to the point "1" again in darkness (by sweeping the electric field from -0.34 MV/m to $+0.34$ MV/m and to zero). As would be expected from the 180 deg symmetrical polarization rotation, a similar effect, but of opposite sign, is observed for the ferroelectric point "2" (obtained by sweeping the electric field from $+0.34$ MV/m to -0.34 MV/m and to zero) shown in the inset (c) of Figure 3.6. However, the sample depolarized state "0" obtainable by a damping oscillated voltage (similar to the one shown on Fig. 2.12) procedure shows no remanence, see Figure 3.6(b), in support of the photocarriers distribution hypothesis, as in this state an intrinsic electric field is screened by the domain structure.

To evaluate the charge generation efficiency the sample was putted into the polarization state "2" with the same procedure as used throughout this thesis (poling voltage $0\,V \rightarrow V_{max} \rightarrow -V_{max} \rightarrow 0\,V$). After the stabilization is reached, the "raw" charge was measured as a function of time while applying a single $50\,sec$ light pulse of maximal intensity (UV LED rates $700\,mA$ max supply current). The shape of a pulse (see Fig. 3.7) indicates the charge generation (linear part) followed by its saturation (critical density was reached leading to the inhibition of subsequent free-carrier generation). So from these considerations, taking into account the linear part (assuming charge generation only, inset in Fig. 3.7, the photovoltaic efficiency calculations from the Eq.(2.21) can be evaluated to $\eta \approx 2 \cdot 10^{-4}\,\%$.

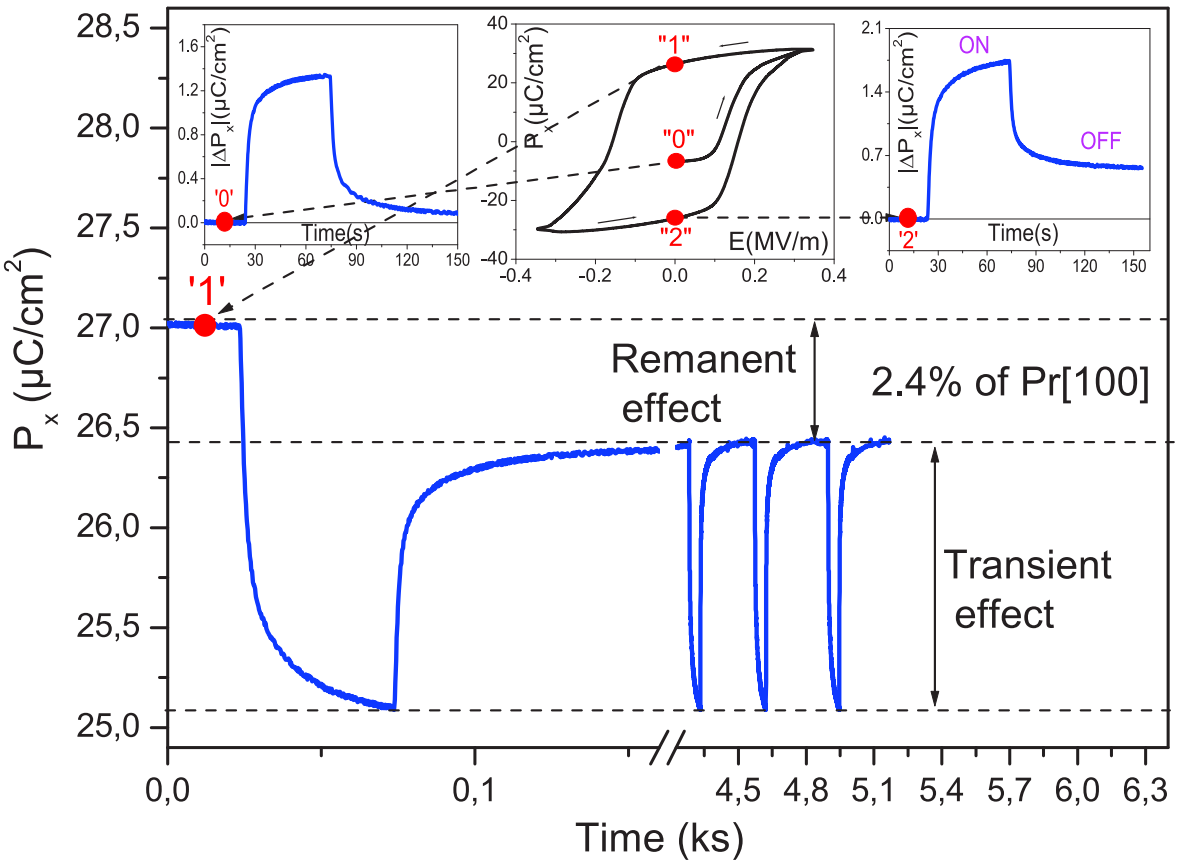

Figure 3.6: PMN-PT32% polarization evolution versus initial FE state under consecutive light pulses.

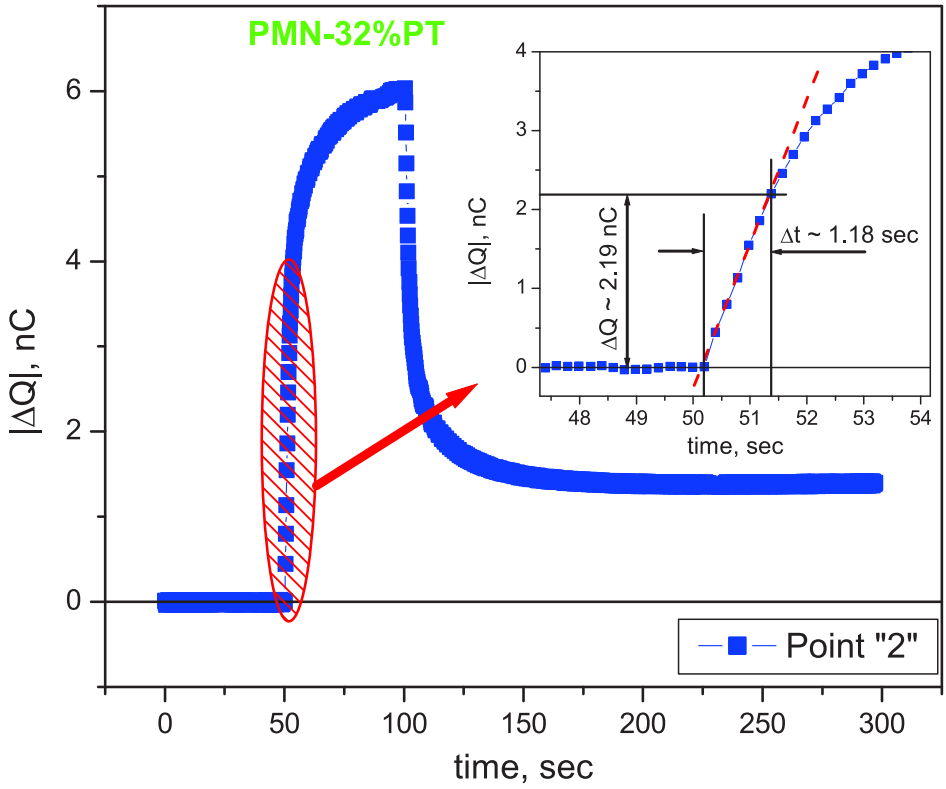

Figure 3.7: Charges generation efficiency in PMN-PT32% composition. Note that the linear part was taken for efficiency calculations.

3.1.2 The $Pb[(Mg_{1/3}Nb_{2/3})_{0.7}Ti_{0.3}]O_3$ (30%) single crystal

Because the above described PMN-PT32% compound belongs to the well-known family of ferroelectric crystals with multifunctional phase diagram, we have decided to test other members of this family for photovoltaic properties. In particular, a careful study of other compounds in the phase boundary region occurring between $30-35\%$ is very promising. Indeed we have found the existence of a photovoltaic effect in the PMN-PT30% compound which exceeds by more than one order of magnitude the effect reported for the PMN-PT32% counterpart. Here we describe and compare further photovoltaic and ferroelectric performances of the two compositions and detail on the light-induced charge dynamics responsible for this effect.

The sample of the same [001] orientation was supplied by the same source (Crystal-Gmbh) in square shape with edges along [010] and [100] directions. Electrodes were formed with silver paste covering the edges in the planes parallel to zy (see Fig. 3.4). The hysteresis loop of polarization versus electric field was taken at room temperature by using a quasi-static FE loop tracer similar to that described in [161], reducing FE fatigue by ultra-low frequency ($0.01\,Hz$) measurements. First of all the FE loop was measured in darkness (Fig. 3.8(b)). This step now should be recognized as an essential one in order to be able to compare the PV properties and determine their relation to the specific FE state. The same loop was then measured under light of same intensity as for the PMN-PT32% compound.

As it can be seen, the light induced effect is much larger then for PMN-PT32% compound. The FE loop measured in darkness along [100] direction reveals a classical hysteresis behaviour resulting in the two polarization states of about $\pm 29 \mu C/cm^2$, in agreement with the literature data. However, when illumination of $365\,nm$ light is applied the apparent polarization increases by more than 4 times. As a consequence of free charge generation by light, the sample becomes leakier FE with apparent increase in the both FE polarization and FE coercive force (Fig. 3.8(b)). The observed light-induced change in the ferroelectric loop largely exceeds in magnitude all previous observations [68, 145, 182, 183]. The corresponding volt-ampere characteristics further illustrate the photo-induced change in electric properties (see Fig. 3.9).
The main three effects arise under light illumination:

- the significant increase of current related to dipole reorientation (ferroelectric peak);

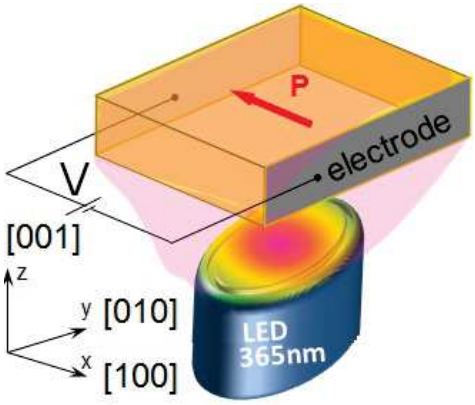

(a)

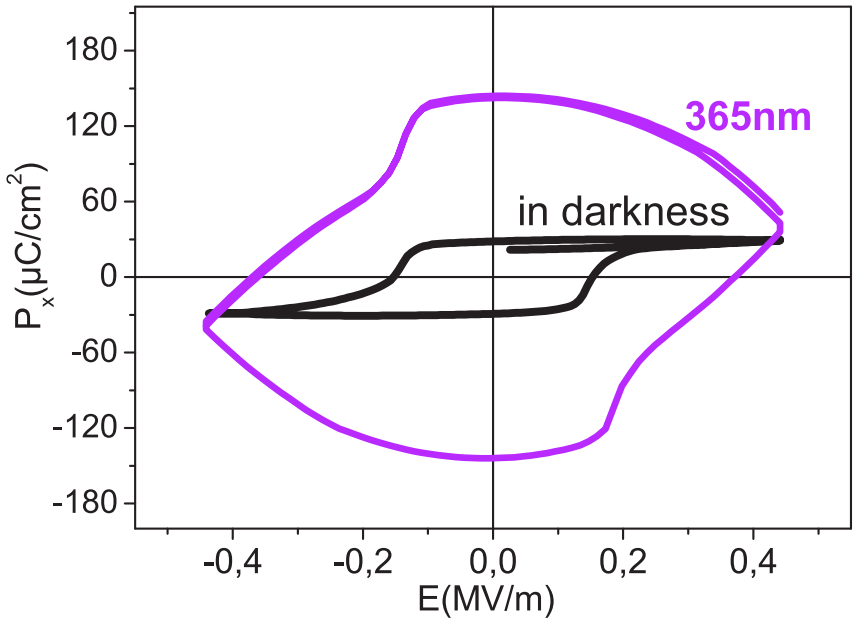

(b)

Figure 3.8: Schematic of the measurements with respect to crystal axis (a). The FE loop of the PMN-PT30% measured in darkness and under UV light (b).

- the general increase in the sample conductivity;
- a noticeable shift in abscissa of the FE loop as a result of light generated charges contribution to the total intrinsic electric field.

The difference between FE currents in darkness and under illumination is presented in Fig. 3.10. As it can be seen the maximum of the light induced effect is achieved

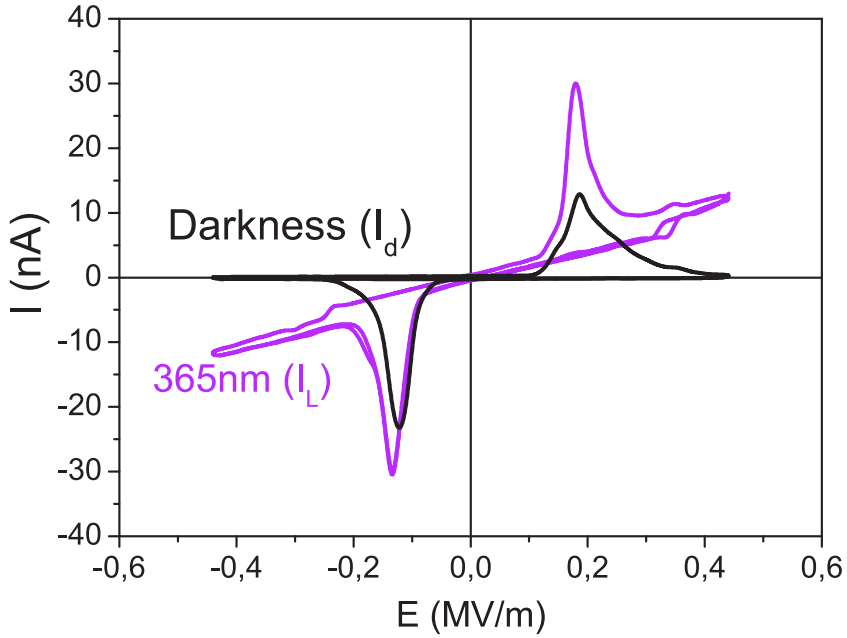

Figure 3.9: I-V loops of the PMN-PT30% measured in darkness and under UV light.

at the ferroelectric peak as in the case of the PMN-PT32% and can be considered as a general feature testifying for the strongly poling history dependent nature of PV effects in ferroelectrics. The tracing of basic parameters of the photovoltaic effect is better illustrated in the zoomed region (see Fig. 3.11). The initial values of short circuit photocurrent and open circuit photovoltage increase largely after poling with $\pm 1\, kV/cm$. In particular, there is also a noticeable down shift of the loop along y-axis, so the absolute value of I_{sc} after pooling with $+1\, kV/cm$ is smaller than the value of I_{sc} obtained after pooling with $-1\, kV/cm$. Same effect is also seen for open circuit photovoltage. Because I_{sc} and V_{oc} are used to evaluate photovoltaic efficiency, the electric tuning becomes possible.

At ferroelectric remanence the voltage change versus light intensity shows a 20-times larger effect than in the PMN-PT32% crystal (Fig. 3.12) in agreement with much larger effect of the light on the FE loop (see Fig. 3.13(a)). The nonlinear behaviour as a function of light intensity with a characteristic peak is observed for both compounds. The form of curves can be explained by the occurrence of two competing mechanisms: the light induced charge generation dominant at low light intensities and the charge recombination processes at higher intensities. These opposing processes give rise to

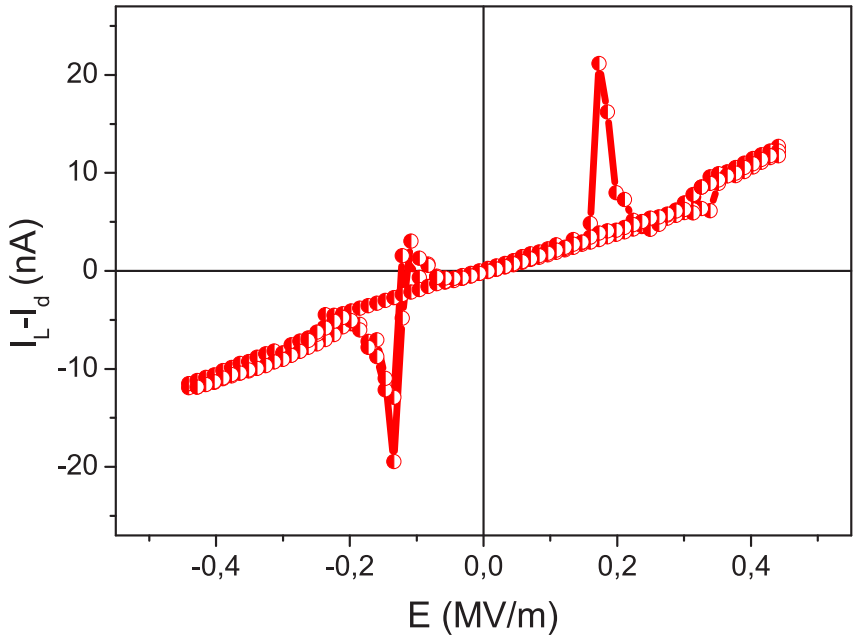

Figure 3.10: The difference between FE currents in darkness and under illumination for the PMN-PT30% crystal.

the peak as a function of light intensity at the value where numbers of generated and recombined carriers are expected to become comparable. The intensity dependence of the PV effects will be discussed in more details in the Chapter 4.

In order to get insight into the origin of the larger PV effect in the PMN-PT30% crystal one can start with polarization (intrinsic electric field) comparison for the two crystals. The role of polarization magnitude in the PV effect can be verified by comparing ferroelectric loops of both compounds in darkness (Fig. 3.13(a)). The PMN-PT30% compound with a larger photovoltaic effect indeed shows a slightly larger remanent polarization. However, the difference of $0.2\,\mu C/cm^2$ is rather too small to be responsible for the large difference in the photovoltaic properties reported in Fig. 3.12. The same argument can be pointed out for pyroelectric coefficients that do not change much for $Pb\left[(Mg_{1/3}Nb_{2/3})_{1-x}Ti_x\right]O_3$ composition for $0.3 < x < 0.32$ [173].

Another possible explanation can be based on the hypothetical difference in the optical absorption coefficients between the two compounds. However, the optical absorption is known to decrease with decreasing x in the $Pb\left[(Mg_{1/3}Nb_{2/3})_{1-x}Ti_x\right]O_3$ composition[184] in agreement with the fact that the PMN-PT30% crystals are more

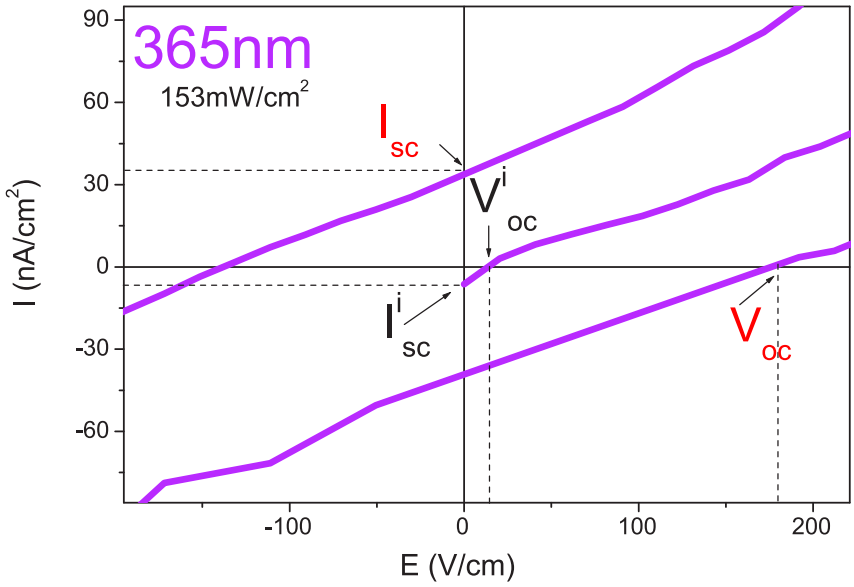

Figure 3.11: A zoomed evolution of the ferroelectric current under light in the remanent polarization state with $1\,kV/cm$ electric field amplitude.

transparent at ambient conditions (Fig. 3.13(b and c)). On the other hand, the composition of PMN-PT crystal is optimized to obtain large piezoelectric properties, reaching a maximum for $x = 0.3$, exactly at the lower morphotropic phase boundary[156]. Thus, thanks to the enhanced piezoelectric properties in the PMN-PT30% compound, the light-generated charges could contribute more efficiently to the electric field-assisted transformation between the thermodynamically equivalent phases at the morphotropic phase boundary. The light then induces changes in polarization that are connected to stress. Consequently, the larger the piezoelectric coefficient is – the larger the light-induced effect becomes (expected on the lattice deformation), which, in turn can modify the bandgap[17, 185, 186] of the material leading to the increased photovoltaic effect. Although this mechanism is possible, its contribution is unlikely to be dominant here because the piezoelectric coefficients do not differ by the order of magnitude in both compounds [156], although the PV sensitivity to deformation is indeed larger for the PMN-PT30% crystal (see Chapter 6). The intrinsic mechanism of light induced charge generation may also come into play deserving a separate study including symmetry dependent and defect dependent[187] arguments. Anyway, an enhancement in the photovoltaic effect of more than one order of magnitude that has been found in

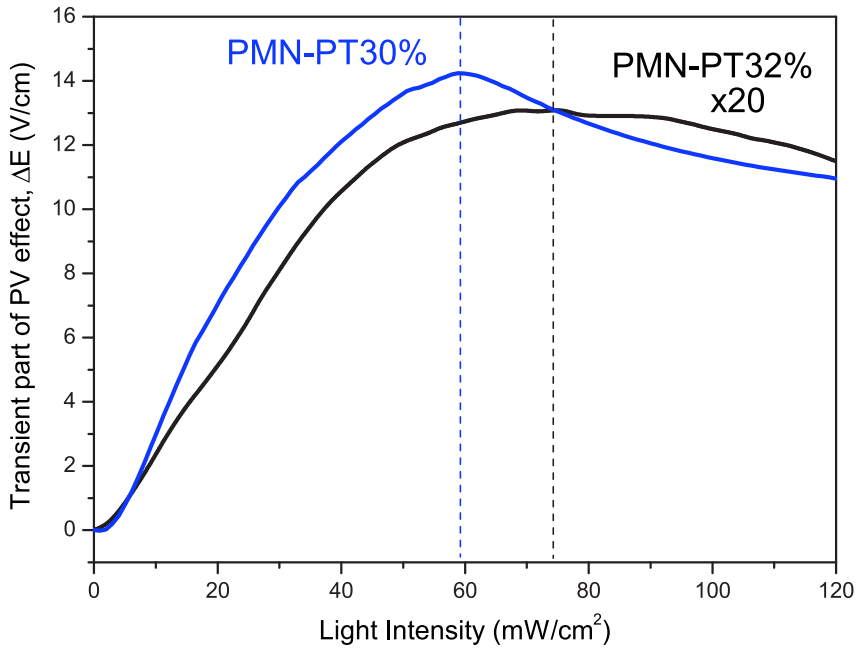

Figure 3.12: Comparison of photovoltaic effect for the PMN-PT32% and PMN-PT30% crystals at room temperature for samples in a remanent FE state.

the PMN-PT30% compound increases the number of photovoltaic crystals and demonstrates the composition-dependent tuning. This result should rapidly prompt a screen of other compounds of the same family as well as similar compositions[85, 188, 189] in which photovoltaic effects can occur thanks to acentricity[168] with the aim to better understand and optimize their photovoltaic properties.

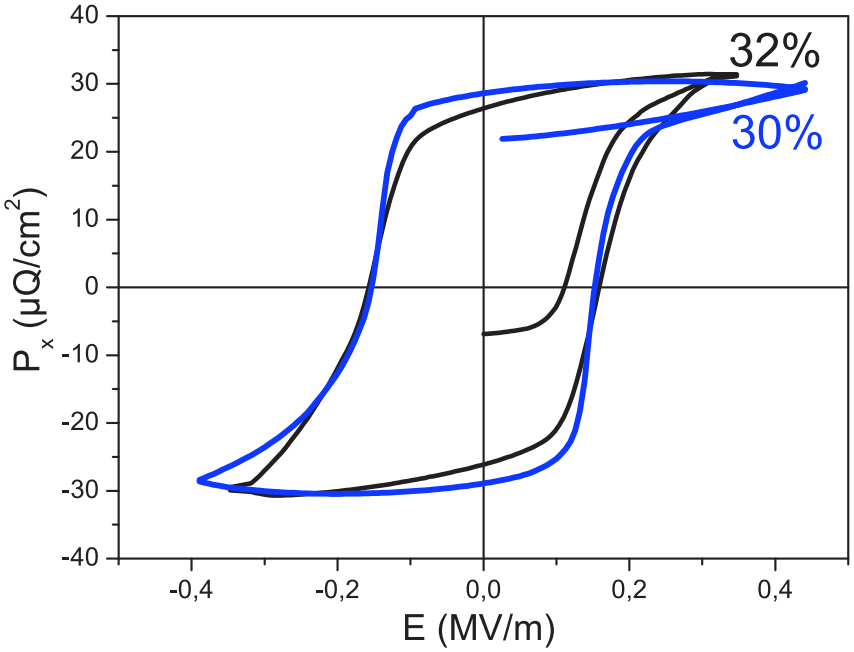

(a)

(b) (c)

Figure 3.13: Comparison of ferroelectric loops in darkness between PMN-PT32% and PMN-PT30% crystals (a). Figures (b) and (c) show pictures of the both crystals (32 % and 30 % compositions respectively) on a white background indicating larger absorption in the case of 32 % composition.

3.2 Extension of the obtained results to Bi_2FeCrO_6 films

Although the results initially reported for PMN-PT32% were qualitatively reproduced also for the PMN-PT30% compound the question can rise if they are extendable to other photovoltaic ferroelectrics. While the PMN-PT crystals provide an excellent model FE PV compound, the low photovoltaic efficiency does not permit to speak about their applications in PV elements. Therefore it was decided to test the results on another compound to see if our conclusions are possibly extendable to all PV and FE systems. For this purpose the Bi_2FeCrO_6 film was chosen due to its recently reported interesting PV properties possibly reaching 8% of PV efficiency. In order to perform the electrical measurements, a 98 nm thick Bi_2FeCrO_6 film was deposited onto Nb:STO substrate (NSTO) and covered by 100 nm thick transparent ITO electrode providing both good electrical conductivity and high optical transparency (Fig. 3.14 (right)). The 1 mm^2 area of the electrode was then contacted with a copper wire using a conductive epoxy (Fig. 3.14 (left)).

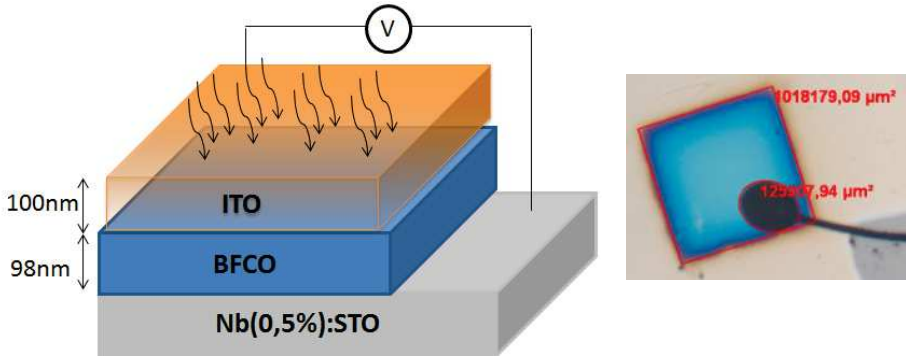

Figure 3.14: Schematic representation of the device used for the experiment (left) and a microscopic image (right) of the electrical contact indicating the active sample area.

The electrical measurements were first performed in darkness by sweeping voltage between $\pm 8\,V$ to test ferroelectricity (Fig. 3.15). At +6V a clear FE peak originating from the polarization reversal is observed (Fig. 3.15(inset)) even though the curve shows a large level of leakage current. Although the expected peak is not visible for negative voltages due to overwhelming ohmic conductivity the FE coercive field of $\sim 64\,MV/m$ extracted from the volt-ampere characteristic is in a good agreement with

the previous study[190] as well as the polarization switching can be evidenced by PFM measurements (Fig. 3.18).

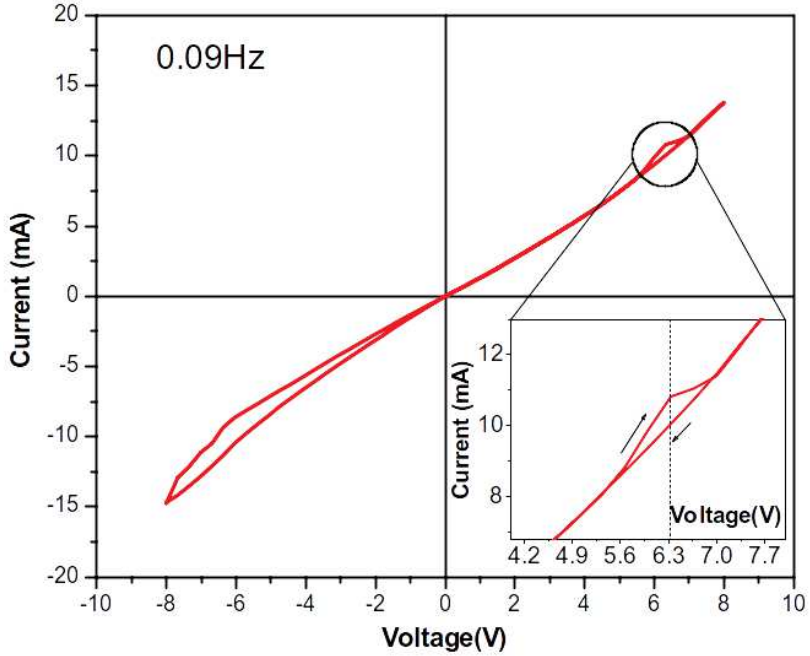

Figure 3.15: I-V loop of the BFCO film recorded in darkness.

In order to study the effect of light on the BFCO sample, a current-voltage measurement has been recorded in dark and under a $365\,nm$ wavelength excitation light emitted by a same light emitting diode (LED). Because the photovoltaic effect in ferroelectrics can be poling dependent[143–145] the sample was previously depolarized in darkness using an oscillating damped voltage procedure (similar to that shown on Fig. 2.12). After that the sample was exposed to $365\,nm$ and $153\,mW/cm^2$ of radiant power, and the current was recorded in the depolarized state during voltage sweep starting from zero to $+8\,V$. Afterwards voltage was swept from $+8\,V$ to $-8\,V$ (marked as positive to negative (P→N) sweep) followed by the reverse negative to positive (N→P) sweep (from $-8\,V$ to $+8\,V$) (Fig. 3.16). The FE-history dependence of the photovoltaic effect becomes clearly evident with an important short-circuit photocurrent (I_{sc}) evolution. The I_{sc} can be effectively tuned between 0.9 and $2.2\,\mu A$ depending on the poling sweep. Consequently, the qualitatively the similar (to the Fig. 3.10 for PMN-PT30%) but quantitatively larger effect of PV hysteresis is confirmed also for the Bi_2FeCrO_6 film. It also becomes evident that the presence of FE domains (depolarized state) clearly affects the photovoltaic effect. It has to be noted that the role of

domain walls in the PV effect was a subject of many studies[82, 112, 148, 149, 191]. In that respect, our results clearly demonstrate that the poly-domain (depolarized) state can indeed be advantageous for PV effect under specific conditions (if compared to random FE ground state or here to the state under the P→N electric field sweep). However, a proper electrical pooling (or here N→P sweep) can show even better photovoltaic response than the one of depolarized state. The insight into the PV hysteresis is therefore clearly needed to optimize the performance. A similar hysteretic behaviour is also detected for the open circuit voltage (V_{oc}) with an average value of $0.54\,V$. To get more insight into the photovoltaic memory effect, the open circuit voltage was measured as a function of time during periodic illumination of the sample (Fig. 3.17). Prior to measurements the sample was polarized positively by sweeping voltage from $-8\,V \rightarrow +8\,V \rightarrow 0\,V$. The sample was then first illuminated for 4 minutes and then the light was switched off for 8 minutes. Subsequently the LED was switched ON and OFF three more times (Fig. 3.17).

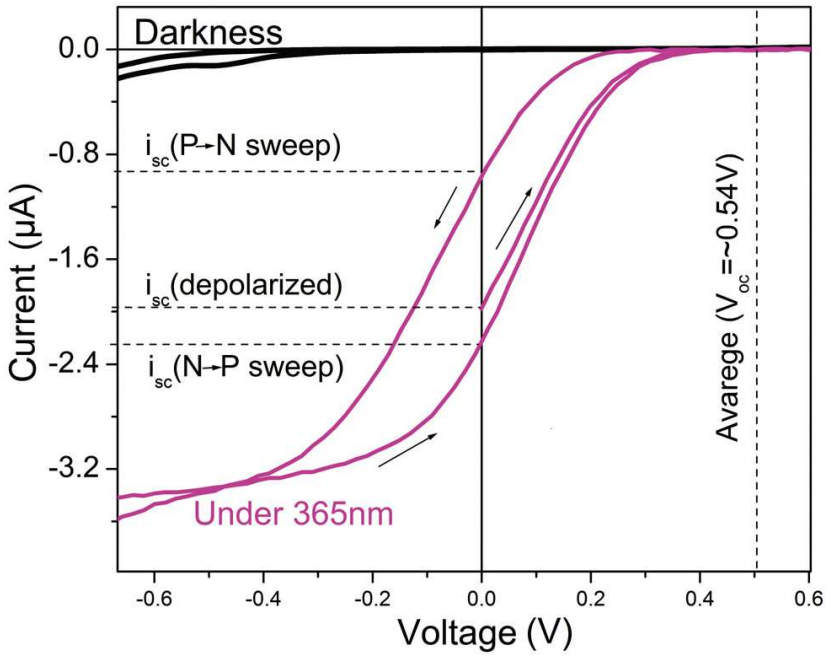

Figure 3.16: Current-voltage measurements on a BFCO sample, in darkness and under $365\,nm$ light irradiation.

The curve features show that at FE saturation the photovoltaic response is in fact a combination of the optically reversible (transient) and irreversible (remanent) effects. With the sample initially polarized positively, the first pulse of light induces

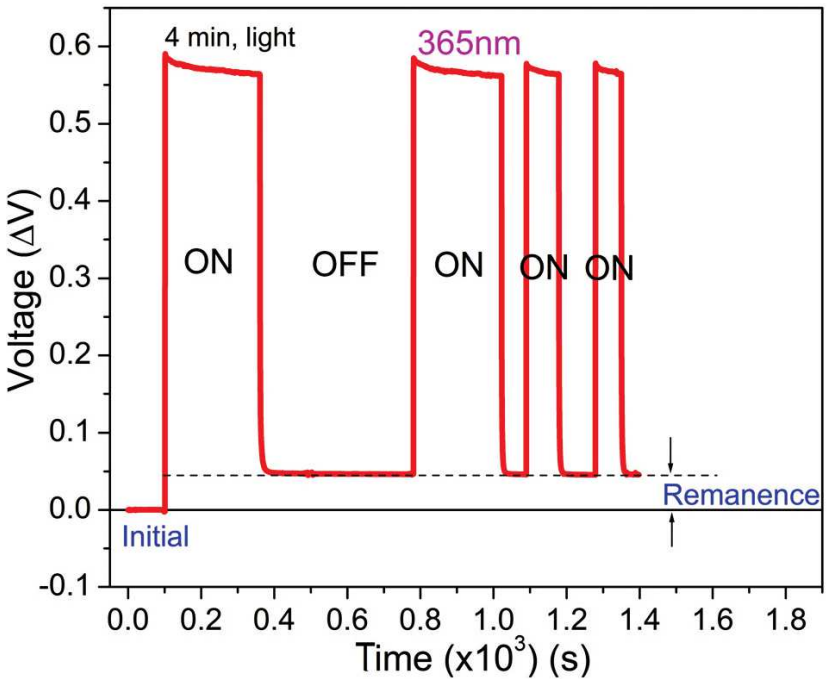

Figure 3.17: Transient and remanent photovoltaic effect for the BFCO sample.

a jump in photovoltage reaching a value of $0.56\,V$. This is followed by an interesting behaviour since when switching off the light, the voltage value did not drop down to initial starting point, but to a value of $50\,mV$ giving rise to a remanent voltage value. All the subsequent light pulses show the same reversible effect. This behaviour therefore confirms the one observed for PMN-PT crystals and can be attributed to the light induced change in the polarization state featuring both reversible and irreversible components, as in the case of PMN-PT crystals. In attempt to elucidate the observed phenomena, PFM measurements on the film surface free of the ITO electrode layer have been carried out. The ferroelectric nature of the film is confirmed by the presence of the electrically switchable polarization states (Fig. 3.18). Poling images were realized by applying $+8\,V$ (large square) followed by $-8\,V$ (small square) (Fig. 3.18). The electrically written FE domains clearly lose their contrasts after light exposure for 4 min (which is the same time used for the first pulse in Fig. 3.17). In agreement with Fig. 3.17 the further light exposure does not modify the PFM images and the initial contrast can only be recovered electrically. The observed behaviour can be explained as follows. For a sample initially polarized positively, the illumination generates carriers which distribute along the previously forced polarization direction.

The generated photo-carriers reduce the surface's charges, and consequently change

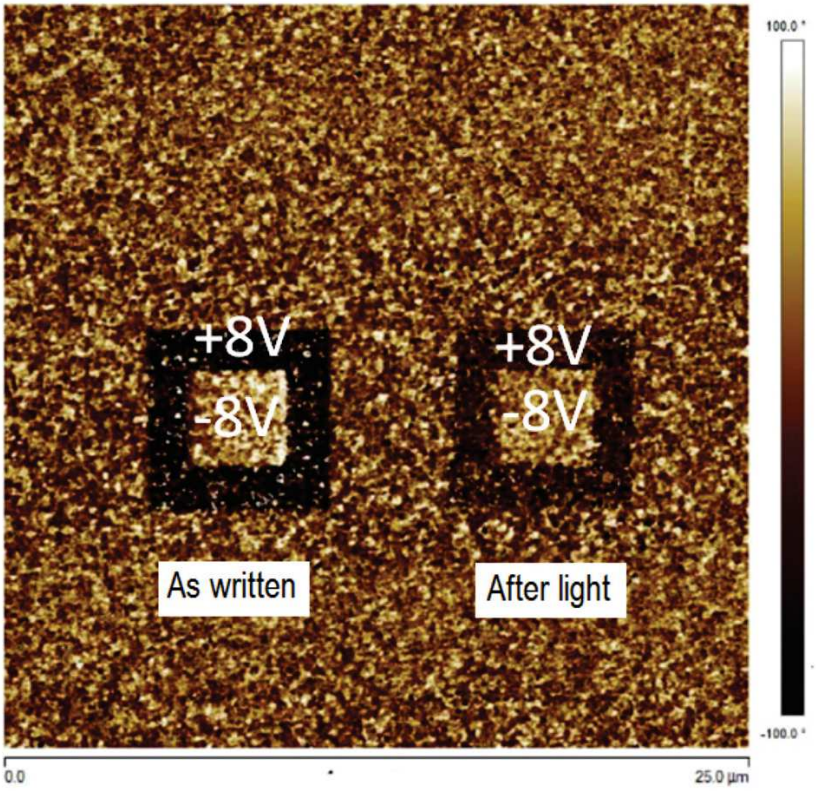

Figure 3.18: PFM poling (phase) images before and after exposure to 365 nm light.

the internal electric field of the material depolarizing the sample. Upon turning off the light, the carriers trapping makes this decrease partly persisting (remanent effect), leaving the sample in a different polarization state. All the subsequent pulses of illumination reveal only a reversible effect; these pulses are in fact of the same power and the corresponding trapping centres are already occupied. The hypothesis of carriers' trapping effect can be confirmed by measuring the photovoltage versus the light intensity (Fig. 3.19). The curve exhibits the non-linear behaviour with three different regions: a fast charge generation, an intermediate saturation and a slow relaxation. The latter can be possibly attributed to the charge trapping processes involved in the processes involved in the remanent effect in Fig. 3.17. It is noteworthy that the possible effect of light-induced increase of temperature in the sample during illumination was also discarded here. The measured temperature change using a thermal camera exhibited only a 1 K of temperature increase compared to the unexcited sample. The sample was then heated in a cryostat and it was found that such heating induces a negligible contribution to its pyro-current and voltage change compared to the light induced effects. The obtained results on the Bi_2FeCrO_6 film confirm hysteretic and therefore

electric field tunable nature of PV properties in ferroelectrics. The both remanent and transient components are present in the PV response as confirmed by independent PFM mapping before and after light.

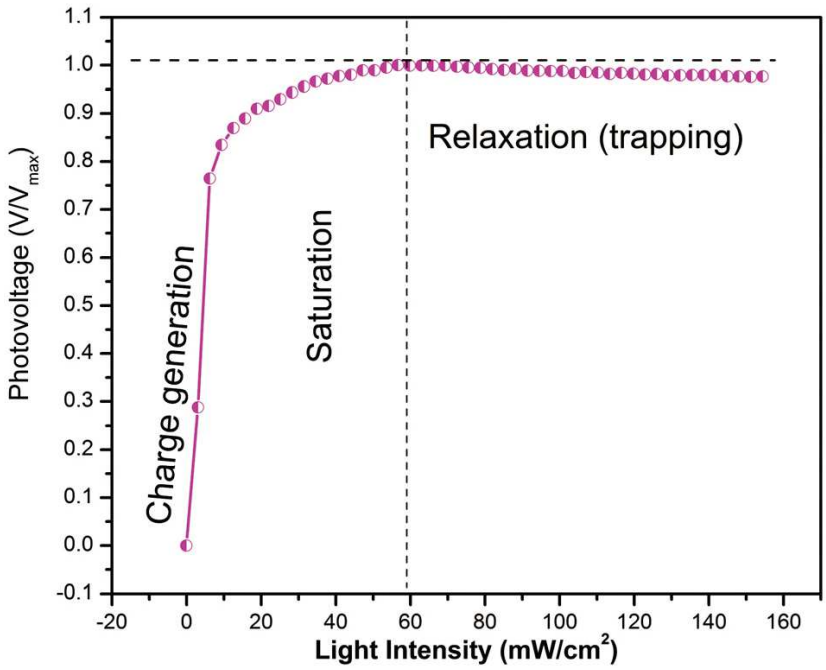

Figure 3.19: Relative change in voltage induced by the 365nm illumination plotted versus light intensity.

3.3 Electric poling dependence of PV properties from Volt-ampere characteristics

The PV cell performance is usually characterized using ordinary I-V measurements to extract short-circuit photocurrent (I_{sc}) and open circuit voltage (V_{oc}). These measurements are generally used to characterize semiconductor-based solar cells. Due to their semi-conductive nature only small electric field can be applied. Moreover, the semiconductor solar cells are not supposed to have any memory effects, contrary to ferroelectrics. These particularities should be taken into account when applying characterization methods of semiconductor solar cells to FE-based PV elements. Moreover, in the case of FE, the electric current can involve different contributions coming from different type of charge movement: domains in sub-coercive region, dipoles at coercive region with everything occurring on the background Ohmic current in the entire electric field region. Therefore it is clear that electric field poling and its magnitude applied during I-V measurements can influence the PV properties evaluated from the classical current-voltage dependences.

In this section we will apply standard PV characterization to the PMN-PT30%

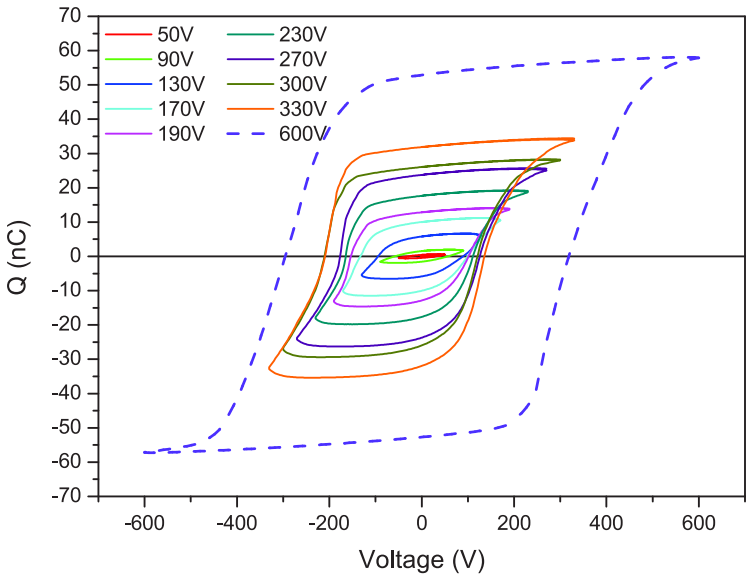

Figure 3.20: Intermediate polarization states measured in darkness in sub-coercive mode (dashed line shows full FE loop).

crystal and will demonstrate a poling dependence of the extracted PV parameters i.e. short-circuit photocurrent (I_{sc}) and open circuit photovoltage (V_{oc}). To investigate dependencies (in PMN-PT30%) the sample was depolarized (by using the dumping field procedure, similar to the one showed in Fig. 2.12) and FE loops were traced in darkness to determine and illustrate the chosen working electric field region (Fig. 3.20).

As can be seen from Figure 3.11, only the initial I-V curve is starting near zero, after returning from over-coercive value the residual current value is observed. To minimize parasitic capacitance the sample was wired with very short and highly conductive copper wires (15 cm long) and only one junction was made to the sample using silver paste for each electrode. Therefore our offset in the current, which appears after poling, can be related to the displacement current in ferroelectrics. As it is evident the FE displacement current can overwhelm the PV current and complicate I-V characteristics of PV and FE samples. To get rid from the FE displacement current contribution the sample was depolarised and classical PV characterization was performed at fixed light intensity but for different poling fields. The sample was poled in darkness with the same rate as for FE loop measurements to avoid damage. The extracted from such I-V measurements (see Fig. 3.21) short-circuit photocurrent (I_{sc}) and open circuit voltage (V_{oc}) are plotted versus electric field magnitude in (Fig. 3.22) and Fig. 3.23 respectively, starting from the smallest and gradually increasing it till coercive voltage. Then the corresponding theoretical and maximal powers were calculated and traced versus poling voltage magnitude (see Fig. 3.24). From those current loops the additional parameters can be calculated (according to the chapter 2.11): maximal power (eq.(2.23), compared to theoretical one showed in Fig. 3.24) and photovoltaic efficiency (eq.(2.22), in Fig. 3.25).

Obtained results show a linear-like behaviour of both photocurrent and photovoltage increasing with the poling field. This can be explained by the increased contribution of the intrinsic FE field that helps in charge separation process. The opposite is also true, when the sample is in depolarized state the overall intrinsic field is minimal. Such domain configuration maximises the recombination cross-section and in turn minimizes the PV effect.

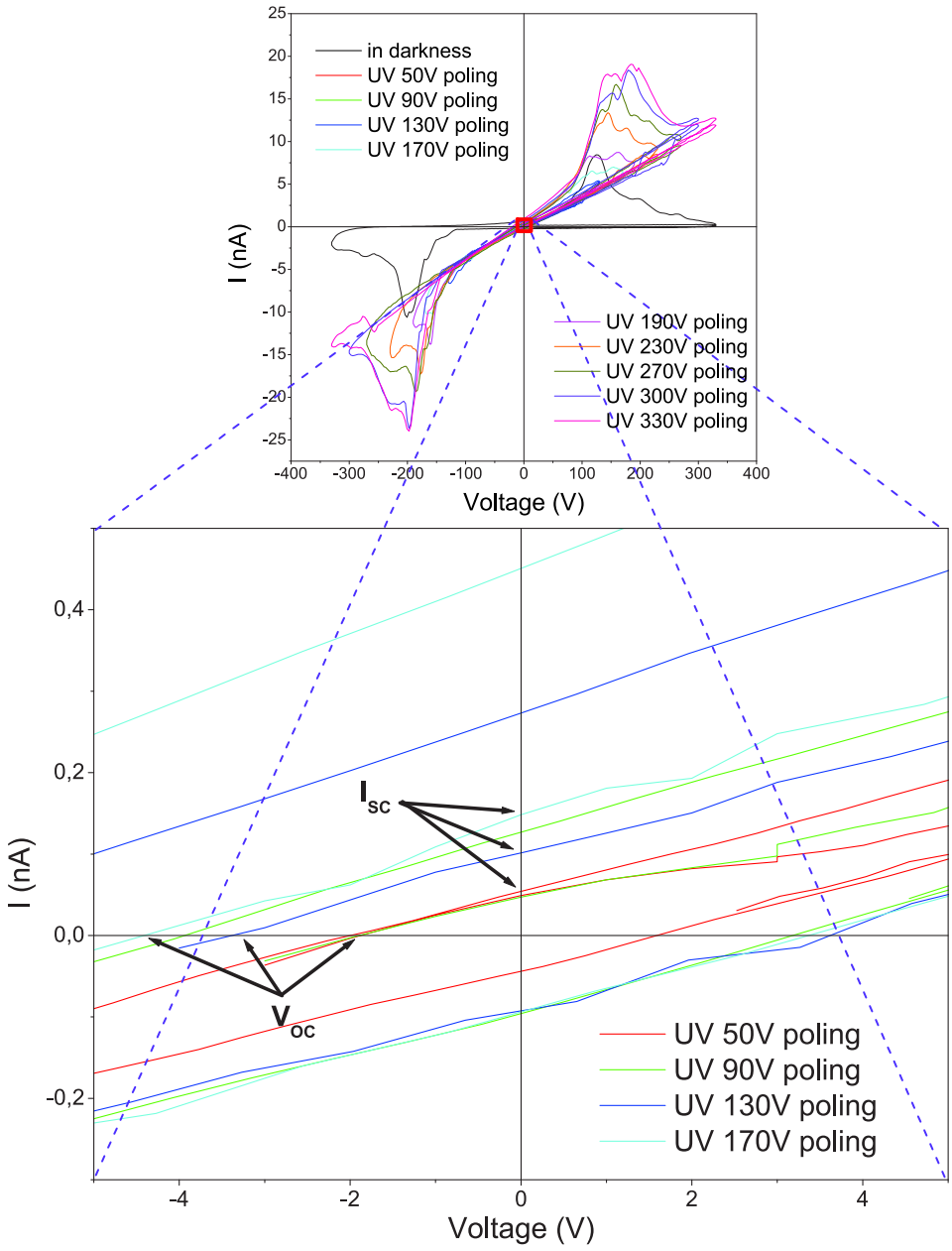

Figure 3.21: I-V loops for the depolarized PMN-PT30% sample under the fixed UV intensity illumination (top). Bottom graph shows the zoomed region for the first 4 poling voltages.

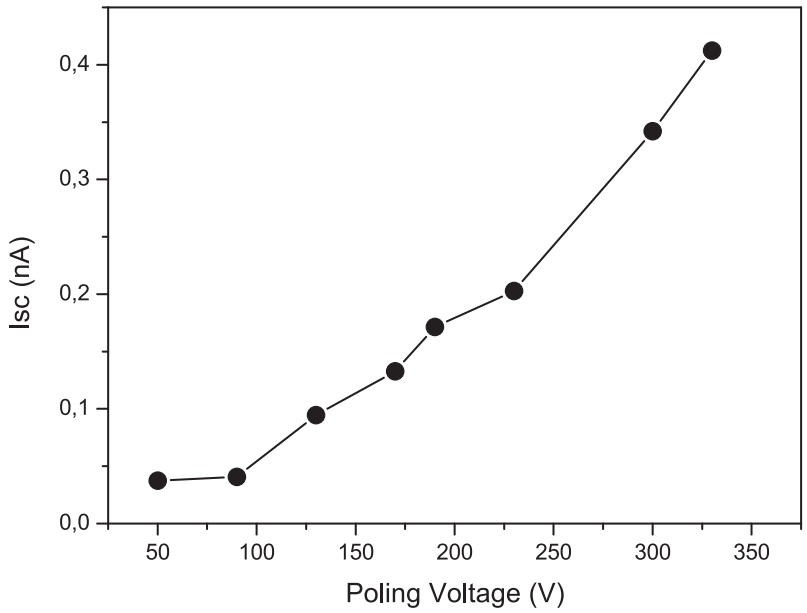

Figure 3.22: Short-circuit photocurrent (extracted from Fig. 3.21) for different poling voltages.

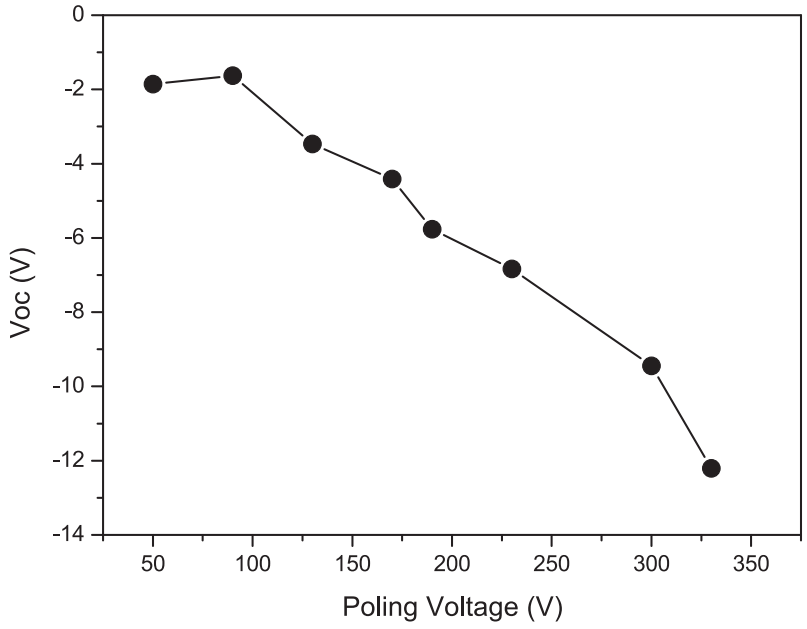

Figure 3.23: Open-circuit photovoltage (extracted from Fig. 3.21) for different poling voltages.

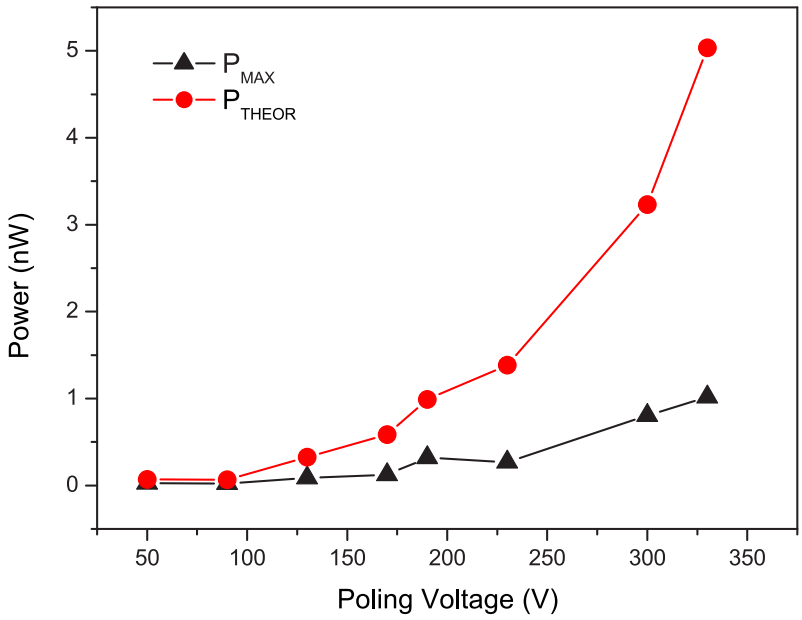

Figure 3.24: Maximum (black) and theoretical (red) generated photovoltaic power dependence on poling voltage for initially depolarized sample.

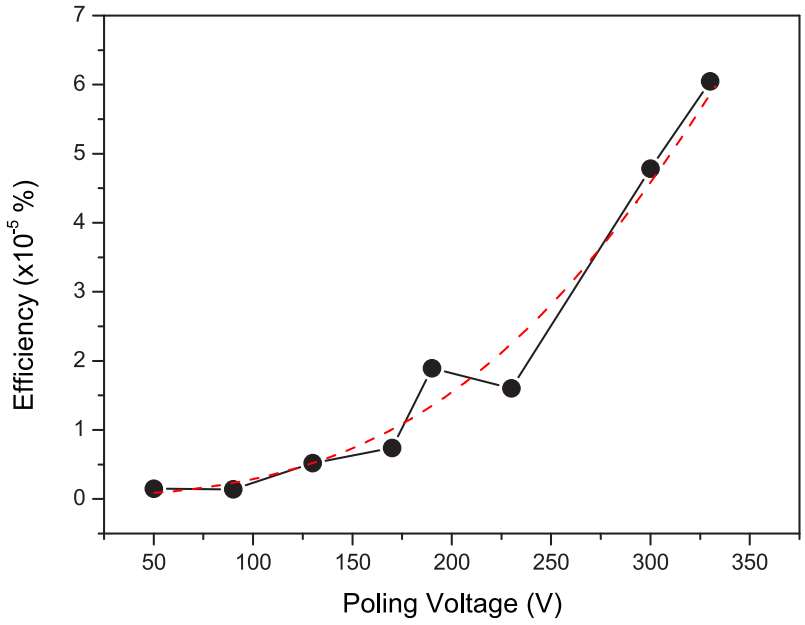

Figure 3.25: Photovoltaic efficiency dependence on poling voltage for initially depolarized sample.

3.4 Conclusions

First of all, the PV effect was found in the $Pb\left[(Mg_{1/3}Nb_{2/3})_{0.68}Ti_{0.32}\right]O_3$ crystal. The PV effect has revealed a hysteretic nature with the photocurrent being maximal near FE dipole reorientation electric field. The hysteretic nature results in the electric field tuning of the PV response and induces the possibility of the remanent PV effects resulting from photopolarization. Stimulated by this discovery, crystal from the same family of compounds, namely PMN-PT30% composition, was tested and had manifested a much larger photovoltaic response although qualitatively similar to one observed for the initial PMN-PT32% compound.

The reported here hysteretic nature and electrical tunability can be extended to other FE and photovoltaic materials as evidenced by experiments on the BFCO film. Obtained results clearly stand for the large tunability potential of the FE and photovoltaic materials by electric field. One should also mention the important influence of the ferroelectric history, in general, on the overall photovoltaic efficiency. So the keen selection and preparation of the FE state is an important step to optimize the performance. The second fact is that the presence of FE domains (found in depolarized state) clearly affects the photovoltaic effect and showed results contribute to the understanding of this issue. Moreover, it becomes clear that to compare PV effects between FE compounds, they must be in well defined FE remanent states obtained after FE saturation. Described properties are expected to be a general and technologically important for electrically switchable features for photovoltaic ferroelectric-based solar elements.

Chapter 4

Optical control of photovoltaic effect in the $Pb[(Mg_{1/3}Nb_{2/3})_{0.7}Ti_{0.3}]O_3$ crystal

As it was mentioned in the previous chapter the extraction of the basic photovoltaic parameters (i.e. circuit photocurrent I_{sc} and open circuit voltage V_{oc}) is usually performed via I-V measurements at fixed frequency of electric field cycling. However, as far as FE materials are concerned (see Chapter 2.6 and Chapter 3) such a characterization is hysteretic and can also be frequency dependent. Moreover, not only charge generation, but also recombination processes must be taken into account, especially because PV cells are supposed to operate at static (DC) regime. However, the extraction of PV parameters are usually performed using I-V measurements at certain rate (frequency) and charge generation and recombination processes may occur at different time scales. Therefore such measurements cannot reveal photocarriers dynamics at zero bias (i.e. the real PV cell operating regime). Furthermore, the measurements are often performed in a one way (i.e. light intensity increase only) while the photovoltaic effect can be of hysteretic nature[146], as most of the FE-based properties, and therefore electric field poling dependent[143, 144, 146]. In this Chapter, we describe the both zero bias light intensity dependence of photovoltaic properties and their sweep rate (frequency) dependence yet at different FE states and measurement frequencies. The presence of the photocarrier generation, distribution and relaxation processes governing the photo-response will be revealed and analyzed.

4.1 Light intensity dependence of the sub-coercive IV measurements

Because of larger PV effect in the case of the $Pb\left[(Mg_{1/3}Nb_{2/3})_{0.7}Ti_{0.3}\right]O_3$ single crystal, all measurements were focused on this compound. To evaluate light intensity dependence of the PV effect, the current-voltage characteristics were first recorded for the sample in the same geometry (Fig. 3.4). Because most of PV measurements in FE in literatures are done for spontaneous (or not presized) FE states, the sample was first depolarized. For this the sample was first moved to zero state where equilibrium between negative and positive FE domains is stabilized (see Fig. 3.2). The pre-programmed depolarization procedure similar to the one shown in Fig. 2.12 was used. After that the I-V loops were recorded for sequential light intensities increase without overcoming coercive voltages (Fig. 4.1(a) and (b)). By comparing qualitatively the I-V characteristics measured on the BFCO film and on PMN-PT30% single crystal one can point out the possible displacement current contribution to the hysteresis opening near zero voltages. Therefore the corresponding short-circuit current (I_{sc}) and open circuit voltage (V_{oc}) were extracted only for the initial part of the loop(zoomed Fig. 4.1(b)).

The extracted photocurrents and open circuit voltages are depicted in Fig. 4.2 and Fig. 4.3 respectively. The both photocurrents and photovoltages approach to saturation, however with the different slope. The difference between intensity dependence of I_{sc} and V_{oc} are known for many photovoltaic FE with the V_{oc} being more representative. The usually linear intensity dependence of I_{sc} in literature can be explained by either insufficient light intensities used or required corrections as commented by other authors[27, 192]. This is apparently not the case for the present study. As discussed in the previous Chapter the I-V measurements for insulating FE and PV samples can be tricky and sometimes may even require modification of the electric circuit (adding a parallel resistor)[57]. Nevertheless, due to small values of photocurrents the photovoltages dominate in the obtained PV generated power (see Fig. 4.4).

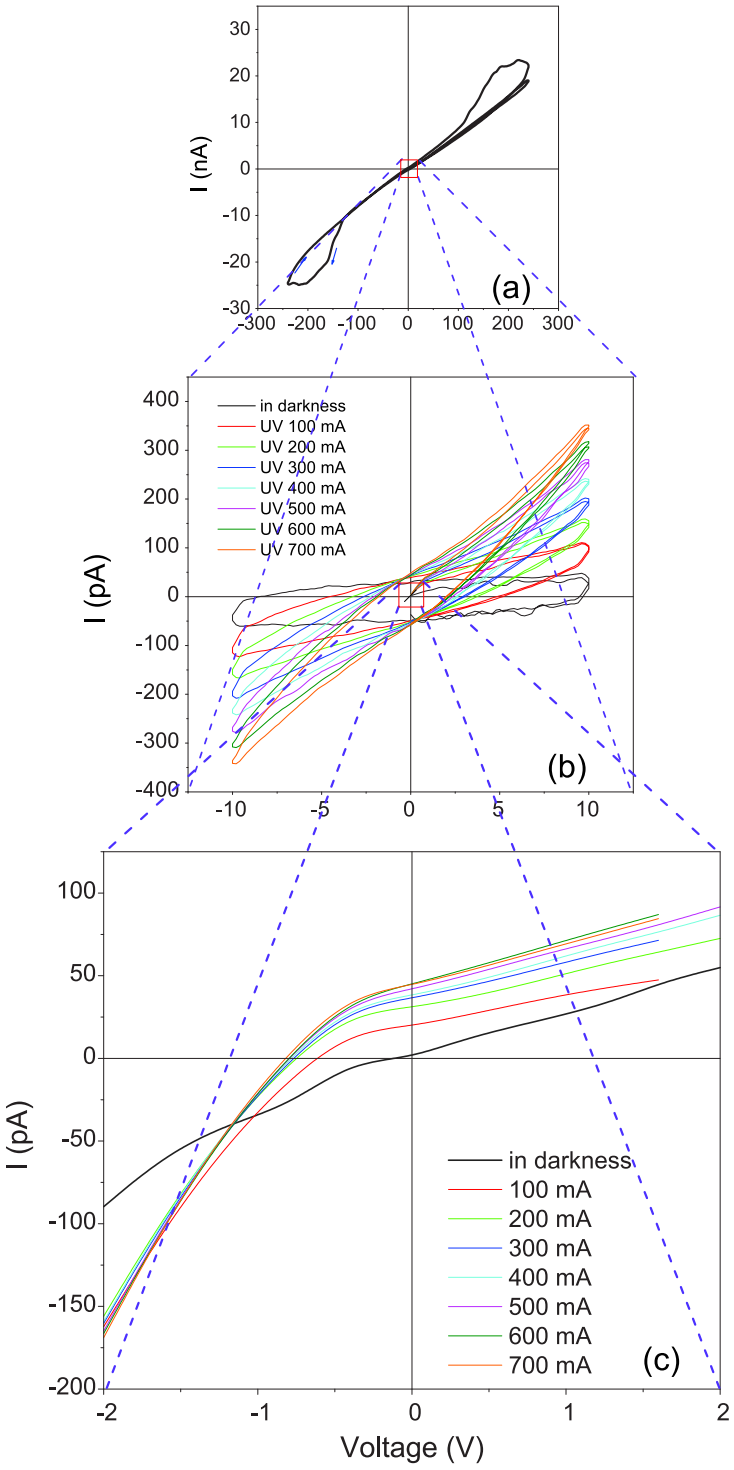

Figure 4.1: Classical Volt-Ampere measurements on depolarized sample in sub-coercive mode under different light intensities.

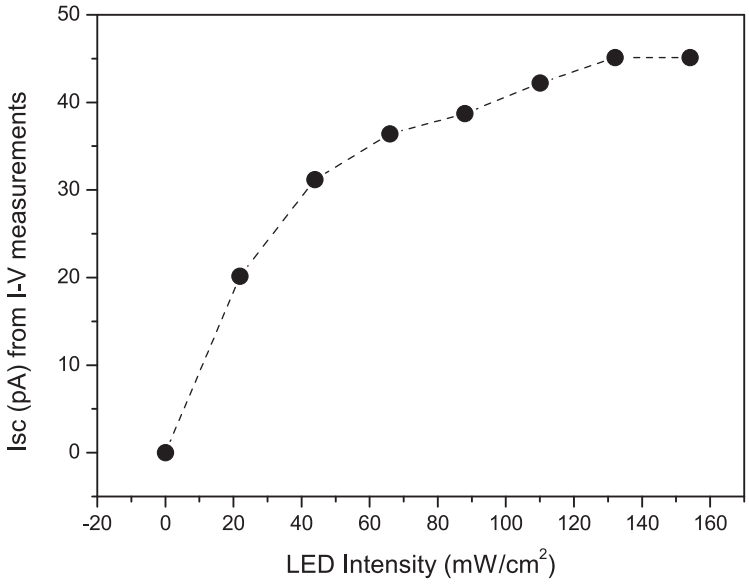

Figure 4.2: Short-circuit photocurrent (I_{sc}) as a function of light intensity extracted from Fig. 4.1(c).

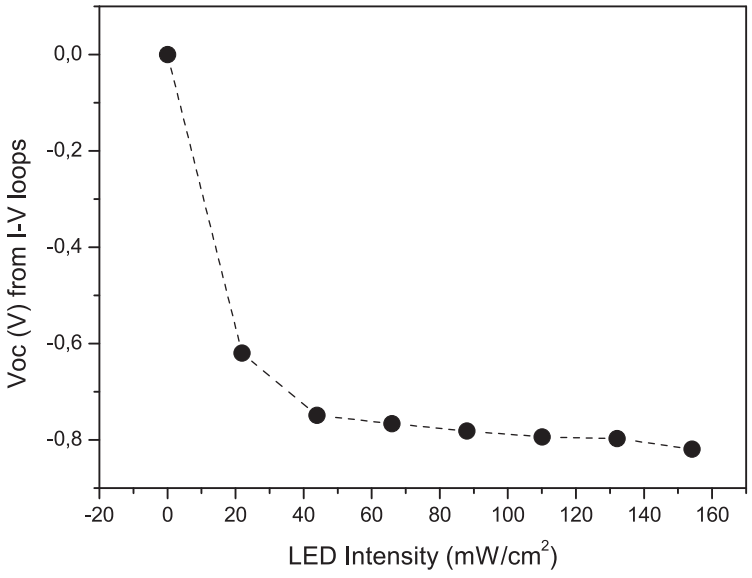

Figure 4.3: Open-circuit photovoltage (V_{oc}) as a function of light intensity extracted from Fig. 4.1(c).

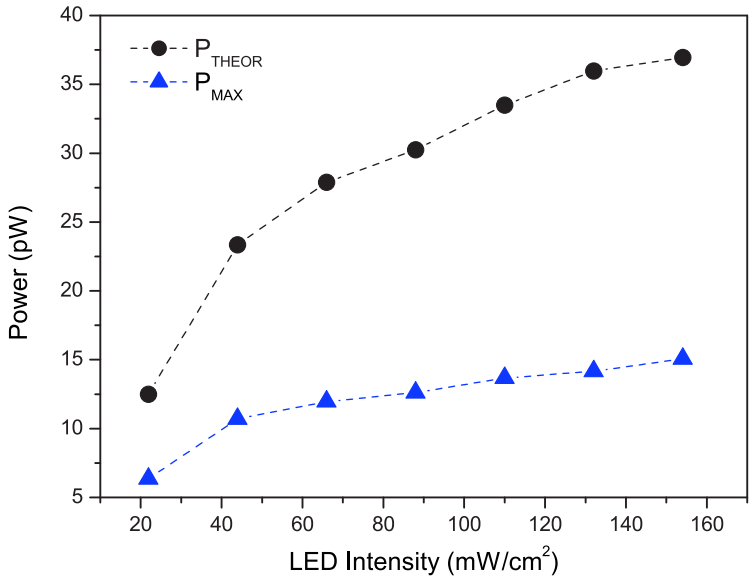

Figure 4.4: Theoretical (black) and maximal (blue) power generated by sample at different light intensities.

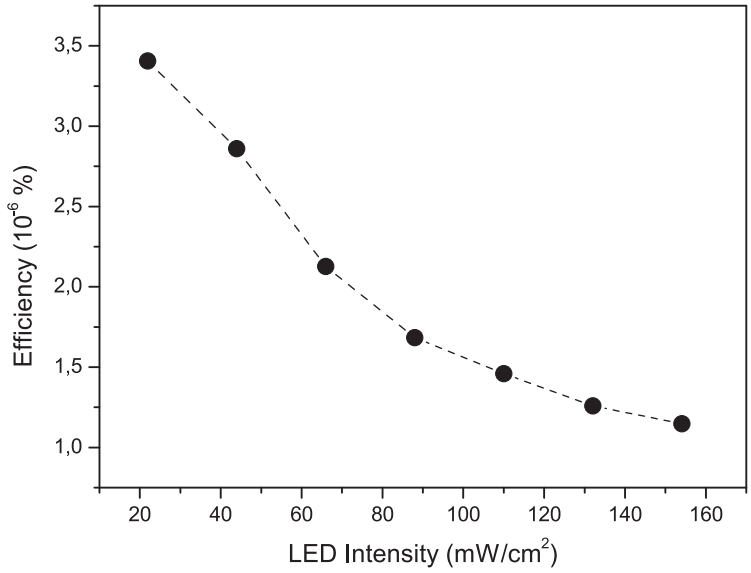

Figure 4.5: PV efficiency (in sub-coercive mode and depolarized state) dependence on monochromatic (UV) illumination intensity.

The efficiency (Fig. 4.5, from Eq.(2.22)) decrease with the intensity while both I_{sc} and V_{oc} increase and saturate (starting from $\sim 20\,mW/cm^2$). The efficiency drop could be explained by quicker saturation of V_{oc} (that dominates over I_{sc} in insulating FE samples). As was shown in previous chapters, the hysteresis nature of the majority of physical properties in FE can also occur in PV response. The signature of such a hysteresis versus light intensity is rarely observed, although can be found in old literature[31]. Such experiments are illustrated in the next section and reveal an interesting physics related to the charge carriers dynamics under light excitation.

4.2 Light intensity dependence evaluated at FE remanence

To study how PV properties depend on the light intensity without external electric field cycling, the light intensity dependence was measured at zero bias for different FE states. The sample was depolarized and current was recorded while sweeping light intensity at $0.01\,Hz$ from zero to $154\,mW/cm^2$ and back to zero (grey curve on Fig. 4.6). The effect on the electric current is small and trend is linear over the entire intensity range.

However, the behaviour changes drastically after polarization. For the polarized sample, after cycling the external voltage $0\,V \rightarrow +600 \rightarrow -600 \rightarrow +600 \rightarrow 0\,V$ (induces remanent polarization state "1", see Fig. 3.2). During the polarization the FE loop was monitored and was confirmed to be in a good shape to insure that the polarizations was switched properly. By keeping the same conditions (light sweep rate, $f = 0.01\,Hz$), the current was re-measured while changing the light intensity up and down (blue curve on Fig. 4.6). Now the effect becomes strongly non-linear and history dependent (positive $\leftrightarrow$ negative branches).

The clear difference of the PV response is observed for depolarized and remanent states. First of all, it becomes evident that the poled (here remanent state "1") is advantageous for the effective photo-generated charge separation. By contrast, well-balanced, by the specially designed depolarization procedure, depolarized state tend to suppresses the PV effect. In the ideally depolarized state the polarization UP and polarization DOWN domains cancel out the charge distribution leading to negligible PV response. In this state the system can be qualitatively compared to anti-ferroelectric ordering, in which the PV effect is not expected. The one more self-rising conclusion comes from the fact that the well balanced depolarized FE state (total electric polarization is zero) is energetically unfavourable and therefore sooner or later leads to non-zero resulting spontaneous polarization. Consequently, very same FE compound found in different spontaneous FE state can display different PV properties. In that respect, only PV properties in same verified remanent states can be representative.

The current loop for remanent ferroelectric state itself reveals interesting dynamics of the charge carriers separated by intrinsic electric field (blue line on Fig. 4.6). Although such a behaviour was not reported previously and is unknown feature of PV ferroelectrics we belief it is an intrinsic signature of the reversible charge generation-

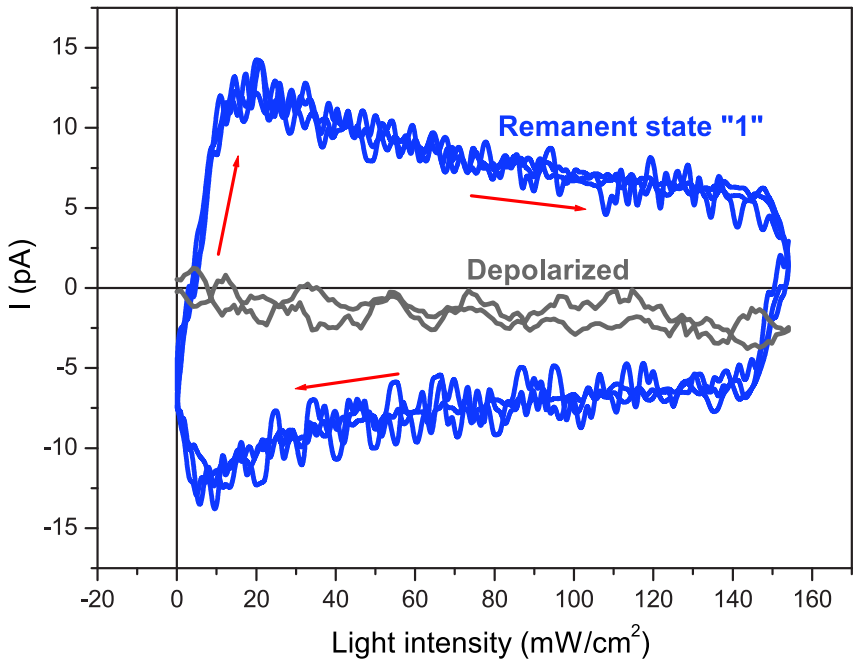

Figure 4.6: Light intensity dependence of the current induced by light for depolarized (grey) and remanent (blue) FE states.

relaxation processes under light. Its intrinsic origin can be indirectly supported by the fact that no such behaviour exists for the depolarized state. As light intensity increases there is a linear increase of the current absolute value that can be subscribed to charge generation under light. This process eventually gets saturated and excess of carriers starts to recombine reducing the speed and the magnitude of the current. As light intensity decreases, this process is reversed, and the majority of carriers become free again, but now move in the opposite direction, in agreement with the sign change of the photocurrent.

The photocurrent loop is also found to be highly frequency dependent of the light intensity cycling (see Fig. 4.7). Although the qualitatively similar behaviour is observed, for faster measurement rates (especially for magenta curve, where the intensity step is bigger) the effect gets bigger because we capturing more photo-carriers moving as they do not have enough time to distribute throughout the crystal and screen/recombine.

When polarization is switched to state "2" (the sweep from $0\,V \rightarrow +600 \rightarrow -600 \rightarrow 0\,V$) the polarity of the effect is inverted as expected from the symmetrical 180° polar-

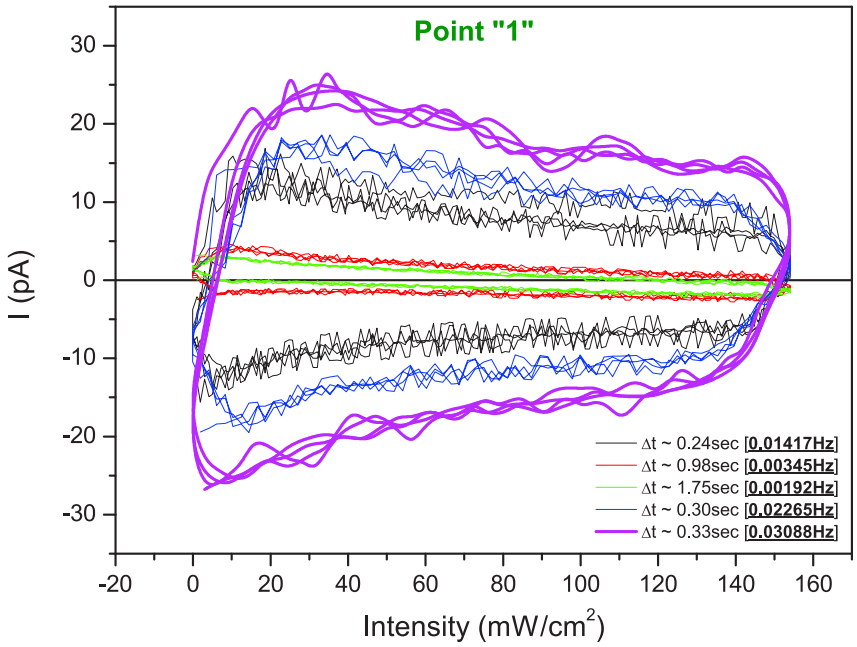

Figure 4.7: Speed (frequency) dependence (Δt is a time delay between points, frequency defined as (total time of $0 \rightarrow max \rightarrow 0$ intensity sweep)$^{-1}$) of the photocurrent loops measured at FE remanence (state "1").

ization rotation (see Fig. 4.8). The single way intensity sweep (i.e. $0 \rightarrow 154\,mW/cm^2$) initially shows a linear part in a small intensity range (where mostly the charge generation dominates) overlapping with the decay part under the higher intensities (recombination > generation). The observed behaviour can also be concluded from kinetics of the photocurrent reported in [37] (Fig. 4.9).

The speed of photocarrier movement decays with time. So the measurement time (time constant) should influence the results. The diminishing of loop opening while increasing the integration time (see Fig. 4.10) therefore is in agreement with carriers having more time to recombine. And vice-versa, at higher sweep rates more carriers moving before some part recombines thus increasing the magnitude of effect and loop opening. The same is true for the photovoltaic effect captured at different rates (Fig. 4.11 in remanent state "1" and Fig. 4.12 in remanent state "2").

The form of photovoltage reflects the same behaviour as current dependence: at high speed we have close to linear curve with no saturation. But if we increase the time constant thus allowing charges to separate/trap the saturation occurs. On the way

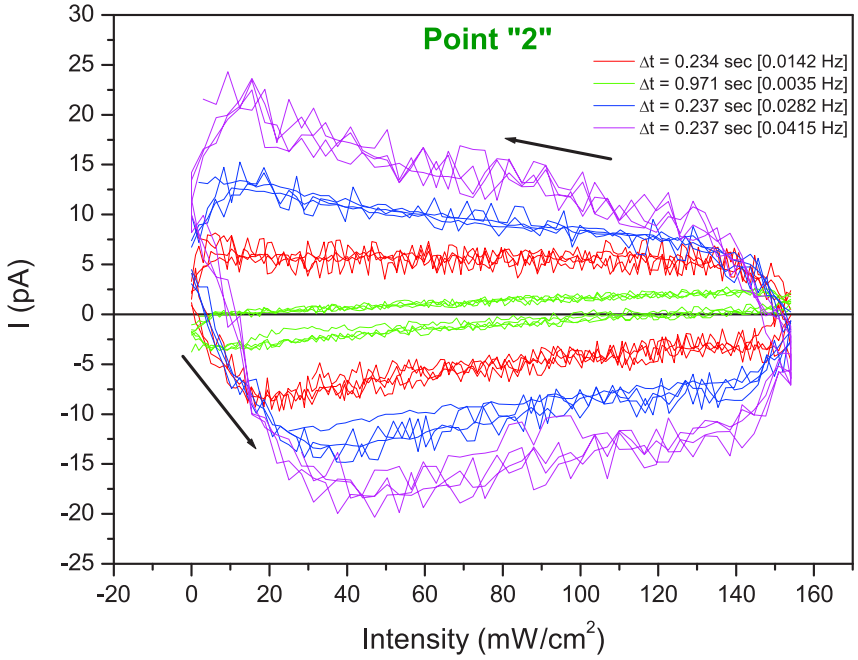

Figure 4.8: Speed (frequency) dependence of the photocurrent loops measured at FE remanence (state "2").

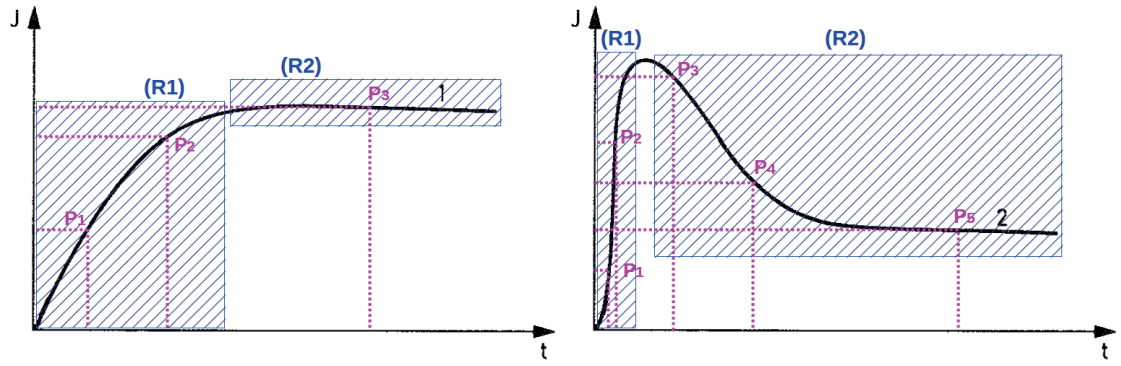

(a) (b)

Figure 4.9: Bulk photovoltaic current kinetics (for fluctuations localized on shallow (a) and on deep (b) levels) in n-type ferroelectric crystal (theoretical investigation discussed in[37], original image taken from there). Working point (time constant for light intensity sweeps) selection (from regions R1, R2) affects the measured current magnitude.

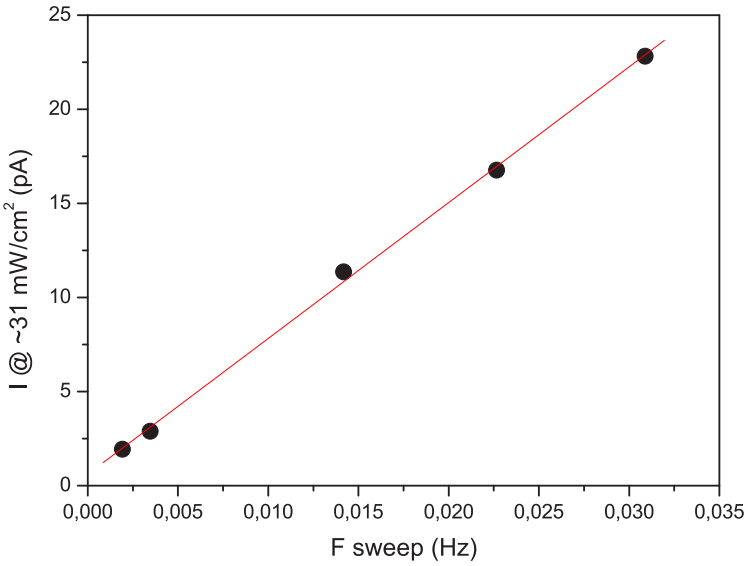

Figure 4.10: Photocurrent loop opening dependence on light intensity sweep frequency (extracted from Fig. 4.7 at 31 mW/cm^2).

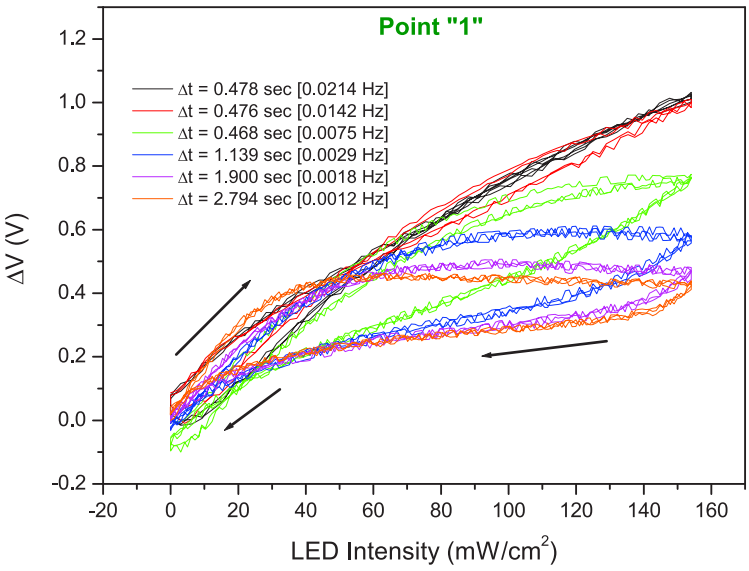

Figure 4.11: Speed (frequency) dependence of the photovoltage loops measured at FE remanence (state "1").

back (while decreasing the intensity), the trapped carriers becomes free and started to

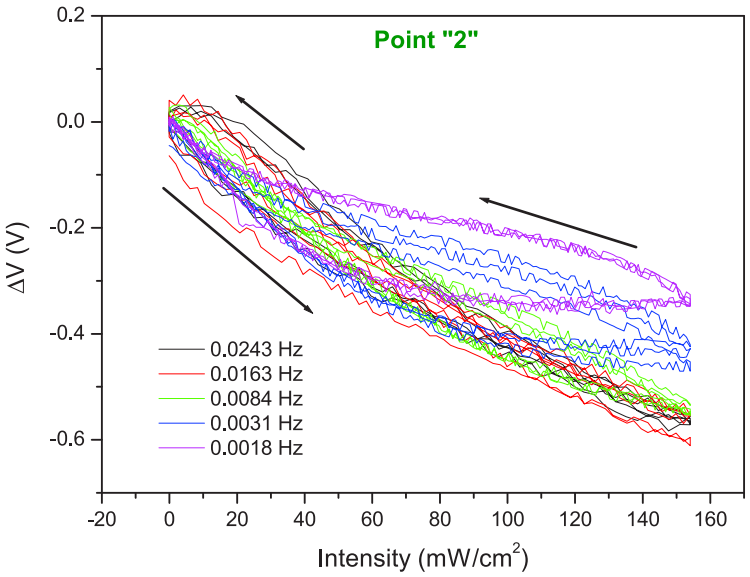

Figure 4.12: Speed (frequency) dependence of the photovoltage loops measured at FE remanence (state "2").

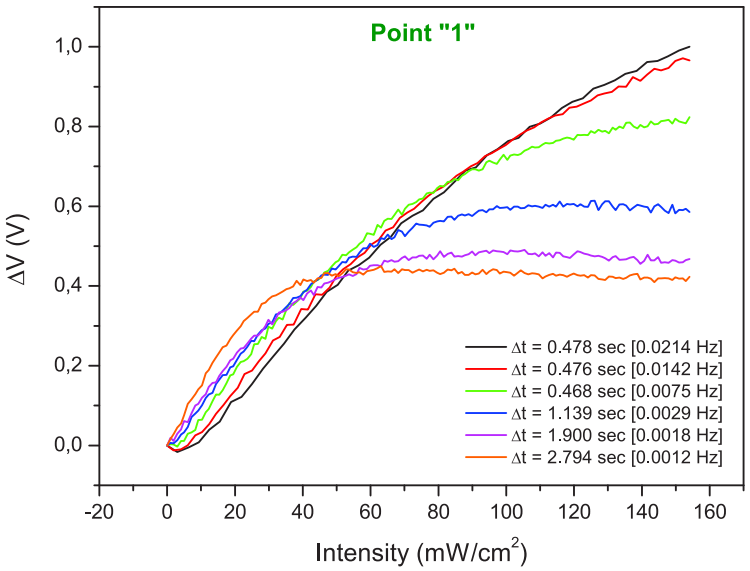

Figure 4.13: Photovoltage for single-way intensity sweep (extracted from Fig. 4.11) at remanent FE state "1".

rearrange themselves to minimize the free energy. Some part starts to move in the

opposite direction (matching the current dynamics, see Fig. 4.7 and Fig. 4.8) diminishing the measured voltage and closing the loop in darkness. Although the intensity dependence of PV current (Fig. 4.7 and Fig. 4.8) clearly depend on measurement speed its sign change upon decreasing intensity looks to be intrinsic because no sign change is observed for depolarized state (grey curve in Fig. 4.6).

The relaxation properties are better seen in Fig. 4.13 for intensity increase only. It has to be noted that decrease in V_{oc} has been reported for some studies[193, 194] but are not usually given a deeper analysis in the literature. In the light of the above results it is becoming very interesting to study the frequency dependence of the PV effects in FE in order to explain often different results obtained in the similar samples. As illustrated in the Fig. 4.13 such a frequency dependence can lead to important difference in the magnitude of the effect.

4.3 Conclusions

The light intensity dependence of the both extracted from I-V measurements I_{sc} and V_{oc} parameters usually show a linear dependence with approach saturation. Although the both hysteresis in photocurrent [31] and the reduction of V_{oc} after saturation were reported [65, 193, 194], they were not given a deeper analysis. However, the reduction in PV properties after saturation can be related to charge trapping in FE. Because I-V measurements under light simultaneously involve both electrical and optical excitations, the zero bias measurements are more convenient to study the photocarriers dynamics.

From experimental results described in this section it becomes clear that first of all one should separate the photovoltaic effects in spontaneous and saturated states. It is evidenced that in saturated states the charges are separated more efficiently while in depolarized states they are screened by domain structure. Since completely depolarized state is not energetically favourable in FE, usually there is some non-zero spontaneous polarization that determines PV response. In that regard, FE loop should be measured to ensure FE saturation. If this is not the case, or FE properties are poor the PV characterisation risk to be device-dependent and deviate from sample to sample.

Secondly, the light intensity dependent PV characteristics may show hysteresis, meaning that light intensity can be used as an external parameter controlling remanent effects. In particular, it becomes possible to find a balance between charge generation and recombination properties (as described in the perspectives section). Interestingly, the zero bias measurements provide insight into the fascinating photo-carriers dynamics occurring on different time scales and demonstrating that a larger intrinsic electric field (FE remanence) is advantageous for PV effect. Such unprecedented dependences also reveal competition between photo-carriers generation, distribution and recombination processes.

Chapter 5

Temperature control of photovoltaic effect

The semiconductor based PV cells generally, reduce their performance with increase of temperature due to increased internal carrier recombination rates[195]. However, in the case of more insulating FE photovoltaic materials temperature dependence of PV effect is less known. In fact, in the case of PV and FE materials the PV effect is attached to and supposed to exist only in the crystallographically acentric structures. Moreover, different types of acentric structures can be more, or less favourable for the PV effects as will be indirectly pointed out in the Chapter 6. Such acentric structures can exist in certain temperature windows and therefore changing temperature one can change the PV response drastically. This chapter is devoted to temperature dependence of the PV effect for the both investigated PMN-PT compounds. The presence of a rich phase diagram and MPB region in PMN-PT with sequential transitions makes these compounds ideal candidates for temperature dependent studies of PV properties. Fridkin *et al*[39] showed that BPVE in $LiNbO_3$, $KNb0_3$ and $Ba_{0.25}Sr_{0.75}Nb_20_6$ ferroelectrics is highly non-linear with temperature. Then Watanabe *et al*[69] also demonstrated the non-linear behaviour of PV effect in PZT/STO epitaxial films. Later, it was showed by Bogomolov *et al*[80] that the current response of $Sn_2P_2S_6$ semiconductor ferroelectric films under illumination consists of both the unsteady (attributed to pyroelectric effect) and quasi-steady (photovoltaic) components. Each of those has its own temperature dependence: one is decreasing, the other – increasing (and reaches its maximum near the Tc) during heating. In its turn, Yang *et al*[84] reported the tunability of the PV properties (both I_{sc} and V_{oc}) in monodomain $BiFeO_3$ films by temperature. How-

ever, the Curie temperature of this pattern compound is too high to investigate what is happening near the polar transition. Because the PMN-PT family was considered mainly in the context of sensor/actuator usage, its piezoelectric and dielectric properties were well studied as a function of temperature also. Because the PV properties of these compounds were reported only recently by us, their temperature dependence was unknown. To bridge the gap in understanding of the temperature dependence of photovoltaicity in this material (32% and 30%) the obtained results are discussed below.

5.1 The $Pb[(Mg_{1/3}Nb_{2/3})_{0.68}Ti_{0.32}]O_3$ single crystal

From the previously discussed results (see Chapter 3) the PV response enhances with increasing of the poling voltage and reaches its maximum in monodomain state. In this state PV properties become dependent on the crystalline structure reorganization during the phase transitions due to the changes in intrinsic electric field. The monodomain FE state becomes also beneficial as it eliminates an additional parameter (sub-coercive FE domain structure and its behaviour during phase transitions) and makes it easier to compare the efficiencies. Moreover, the domain structure is known to modify a temperature dependence of dielectric permittivity[156]. Therefore prior to measurements the sample was first warmed-up in darkness $19K$ above its Curie temperature (Tc $\approx 420K$) and then cooled under over-coercive electric field applied along the [100] direction. The electric field then was set to zero and the dielectric permittivity was measured as a function of time to reach stability. The same procedure was applied to measure polarization and induced electric charge was monitored by electrometer as a function of time to reach the isothermal polarization stability. The temperature dependence of the dielectric permittivity and electric polarization of the $Pb\left[(Mg_{1/3}Nb_{2/3})_{0.68}Ti_{0.32}\right]O_3$ is shown in Figure 5.1(a). Three characteristic transitions at T_1 ($\approx 352K$), T_2 ($\approx 375K$), and Tc ($\approx 420K$) are clearly observed in both measurements. While T_2 and Tc are related to the rhombohedral-tetragonal and the tetragonal-cubic transitions [196], respectively, the domain-structure-related anomaly at T_1 is known to appear as a function of poling [156]. Taking into account that light can modify the transition temperatures [182, 183, 197], the photovoltage was measured for several temperatures, near the above-mentioned critical points where anomalies in the electric properties are observed. To ensure a monodomain FE state the same preparation sequence was cycled. Then the photovoltage versus light intensity (described in Chapter 4) was recorded under each stabilized temperature value while heating-up the sample. From each these curves the corresponding transient (reversible) part was extracted and plotted (some of them) as a function of light intensity while mentioning its corresponding temperature (see Figure 5.2). The results show that even at room temperature the transient part (defined in Section 3.1) of the photovoltage exhibits more than one order of magnitude larger spectral efficiency (see Section 2.10) than for previously reported WO_3-doped crystal [153]. The photovoltaic isotherms reveal non-linear behaviour as a function of light intensity with a characteristic peak. The

form of isotherms suggests the occurrence of two competing mechanisms: the light-induced charge generation dominant at low light intensities which is superposing to the charge recombination processes at higher illumination intensities. These opposing processes give rise to the peak as a function of light intensity at the value where numbers of generated and recombined carriers become comparable. Because the peak position versus intensity changes with temperature, the maximal photovoltaic change and its linear part have been extracted from the photovoltaic isotherms and plotted versus temperature (see Figure 5.3). The photovoltaic effect shows singularities at all three transition temperatures and reveals more than a threefold enhancement near Tc, then vanishing in the paraelectric temperature region. This behaviour confirms that photovoltaicity of ferroelectric origin exists in the electrically polar phase only. The generally larger photovoltaic effect in the tetragonal phase may be connected with the larger polarization (efficiency dependence demonstrated in Chapters 3 and 4) in this phase and also possibly due the bandgap temperature dependence reported for similar compounds [188].

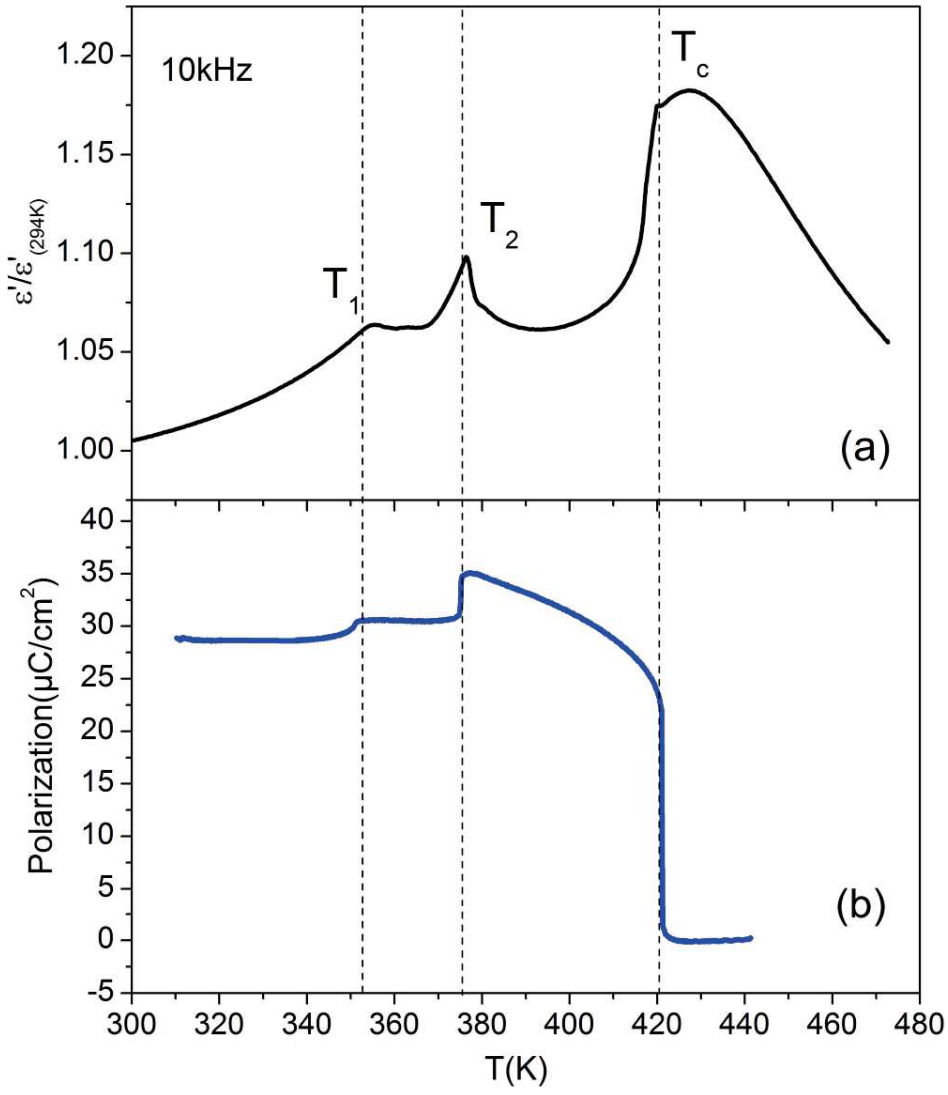

Figure 5.1: PMN-PT32% dielectric permittivity (a) and polarization (b) as function of temperature.

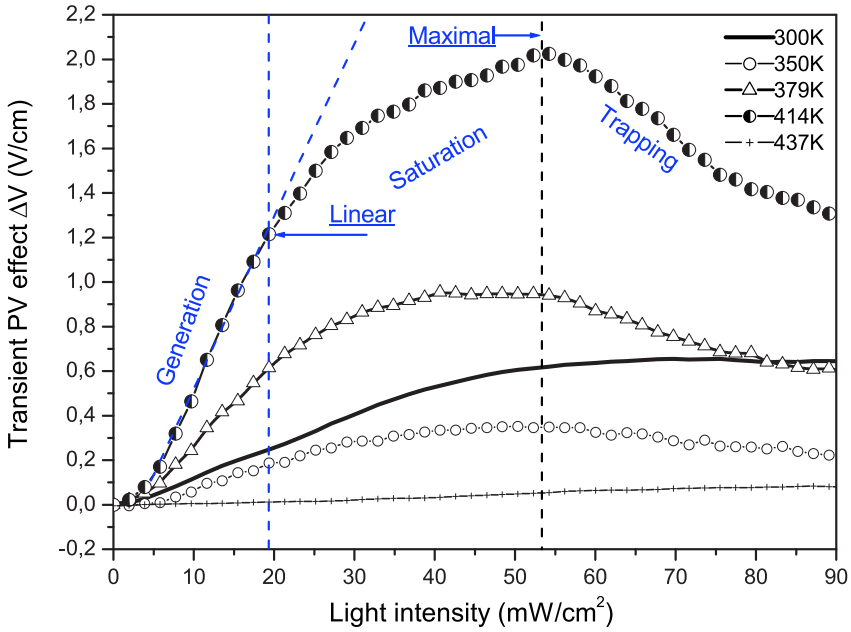

Figure 5.2: PMN-PT32% transient part of photovoltage as function of intensity under different temperatures.

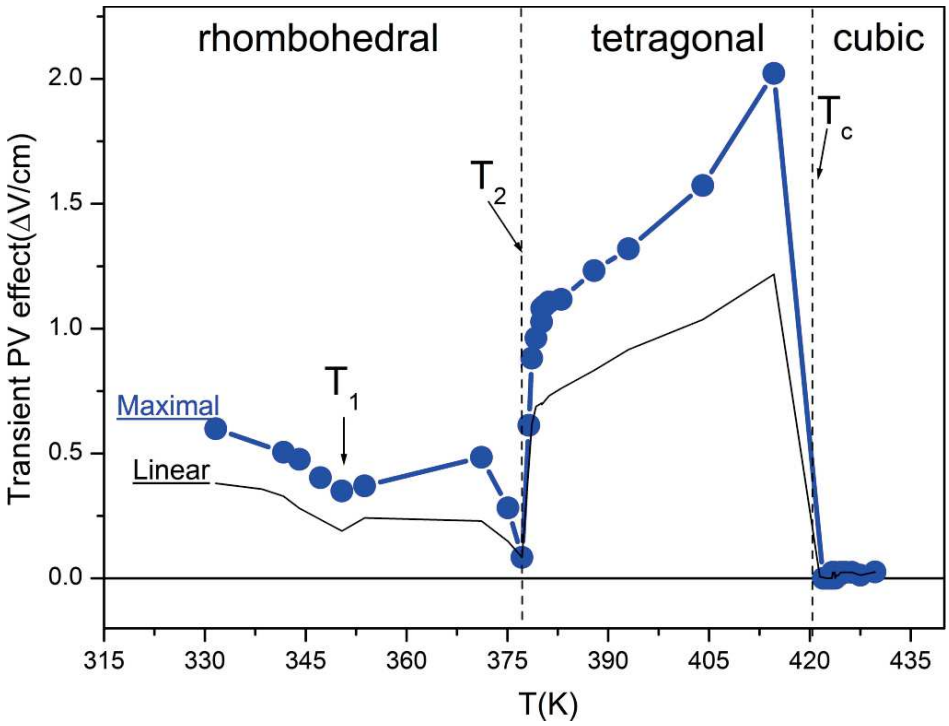

Figure 5.3: PMN-PT32% closer look into photovoltaic effect tuning with temperature.

5.2 The $Pb[(Mg_{1/3}Nb_{2/3})_{0.7}Ti_{0.3}]O_3$ single crystal

The same characterization sequence was used for the 30% compound. Firstly, the sample was putted into the monodomain state with the same poling field and heating – cooling rates. Then, the external electric field was set to zero and the dielectric permittivity was measured as function of time. After stabilization was reached the temperature-dependent measurements were performed. Firstly, the dielectric permittivity was recorded in darkness while heating-up and cooling the sample (see Figure 5.4(a)). The obtained dependence shows two singularities in the dielectric permittivity that are manifesting the phase transitions expected for this compound, followed by a broad peak (common for relaxor PMN) in paraelectric state. To be able to juxtapose the obtained results, the same initial state should also be used for polarization measurements. After the stabilization of prepared monodomain state, confirmed by the polarization versus time measurements, the temperature evolution of sample's polarization was evaluated in darkness while heating (see Figure 5.4(b)). Polarization shows the corresponding phase transitions with a slight improvement in the tetragonal phase and vanishes at the Curie temperature. The same procedure was conducted for the photovoltage versus temperature measurements (see Figure 5.5) under the same poling and lighting conditions as was discussed earlier. The curve shows large improvement in photovoltage in the tetragonal phase. This effect might be related to the higher polarization at this phase (due to the lattice rearrangement) and bandgap variations near the Curie temperature.

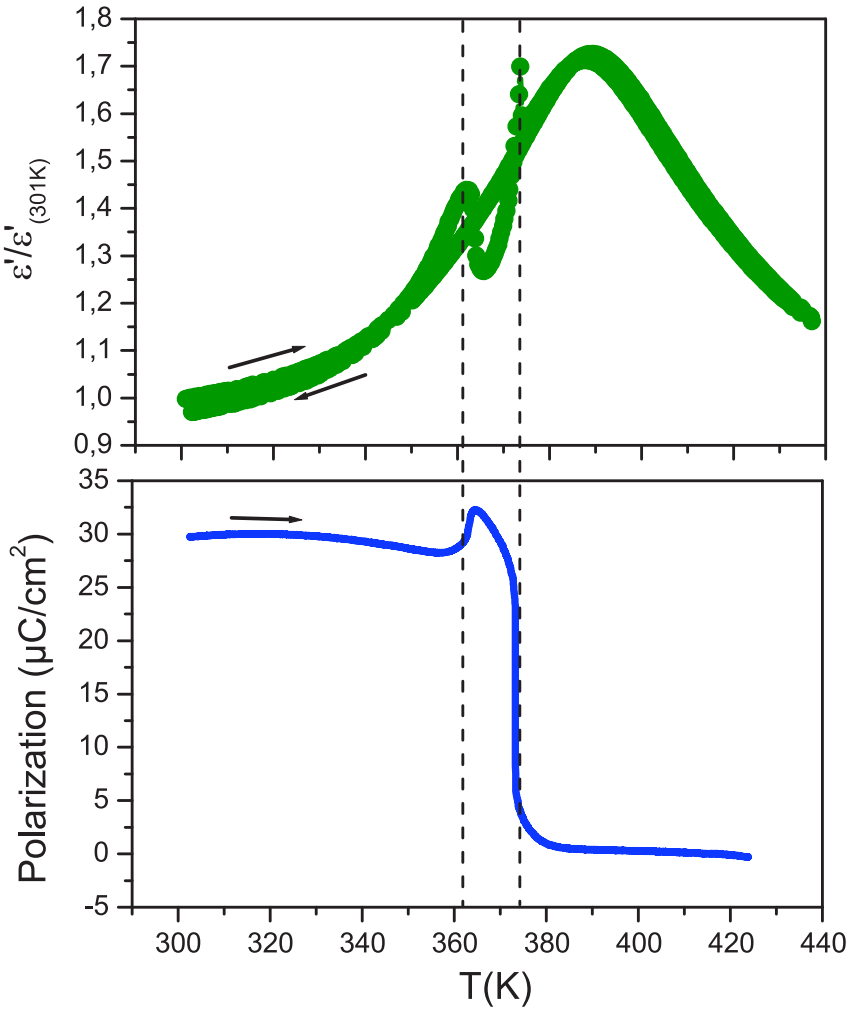

Figure 5.4: PMN-PT30% dielectric permittivity (a) and polarization (b) as function of temperature.

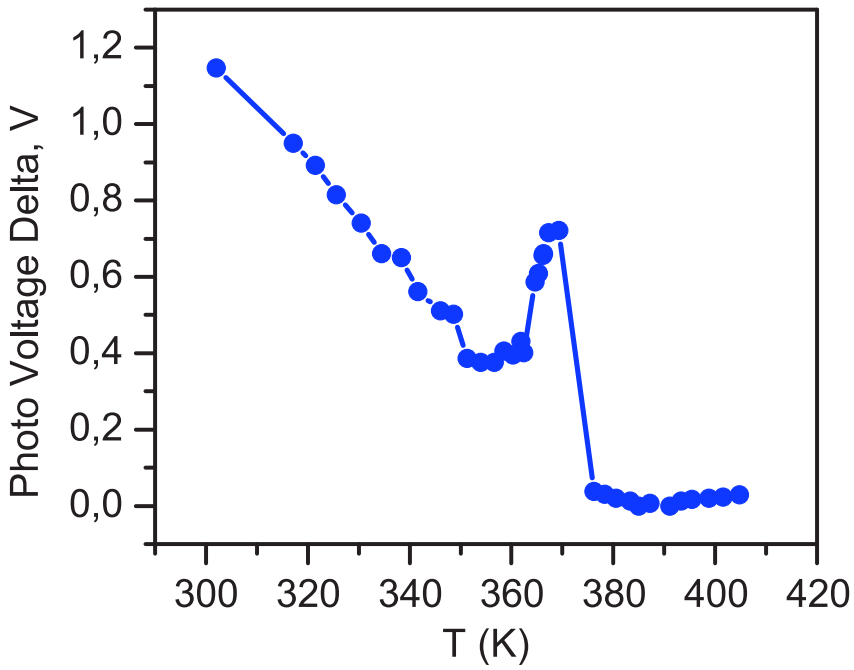

Figure 5.5: PMN-PT30% (sample's length was 1.6 mm) closer look into photovoltaic effect tuning with temperature.

5.3 Conclusions

To conclude this section,one can fist point out that the PV effect found in the two studied compounds with 32% and 30% compositions persists in a wide temperature range above room temperature. The PV effect disappears when crystals are warmed above their corresponding FE Curie temperature where structure becomes centrosymmetric. Although some very small photo-response (see the isotherm of 437 K in Figure 5.2) can still be observed just after the polar to non-polar transition, it disappears with further warming. The clear disappearance of photovoltaic effect above FE Tc is an important observation, confirming that PV origin in FE is related to acentric polar structures. Interestingly, as temperature increases, each sequential crystalline phase manifests a modified PV response. Moreover, all structural transitions show singularities in PV properties reducing or increasing the PV effect. Such structural dependent effects deserve a separate study for establishing PV property engineering. Just before the FE Tc the photovoltaic effect increases more than 2 times for the 32% compound and can be assumed to be a general feature in PV FE. Indeed, the similar increase, although smaller, was also detected for the PMN-PT30% crystal near Tc. Such an increase of PV near Tc, where fluctuations start to occur, can be qualitatively understood in terms of driving the sample out of thermodynamic equilibrium where system becomes more sensitive to external perturbations. Although more theoretical inside would be beneficial here, the results clearly suggest the technologically important way to increase PV effect in FE by moving the system closer to its FE Curie temperature. All obtained results clearly demonstrate the possibility of PV effect tuning in our FE crystals as a function of temperature and may provide a way for PV engineering.

Chapter 6

Strain control of photovoltaic effect

Considering that the temperature-induced change in lattice parameters can modify the PV effect, it was decided to examine a usage of a non-thermal external mechanical strain, as an additional control parameter.

Fact that for the PMN-PT30% single crystal the PV effect was found to be larger compared to the PMN-PT32% one (Chapter 3.1.2) suggests possible stress dependence of photovoltaicity. Motivated by these results I have performed the stress dependent measurements of the photovoltage at room temperature. The results of this investigations are presented in this Chapter.

6.1 Uniaxial compressive strain

First of all, the uniaxial deformation was applied along X crystalline direction as shown in Fig. 6.1 below. The technical arrangements as shown in Fig. 2.17 were connected to micro-stepper motor and controlled by computer. The mechanical deformation was monitored by resistive strain gauge (Fig. 2.16) sensitive to the deformation mostly along X axis. The voltage was also monitored along the same direction while illuminating the sample from a top.

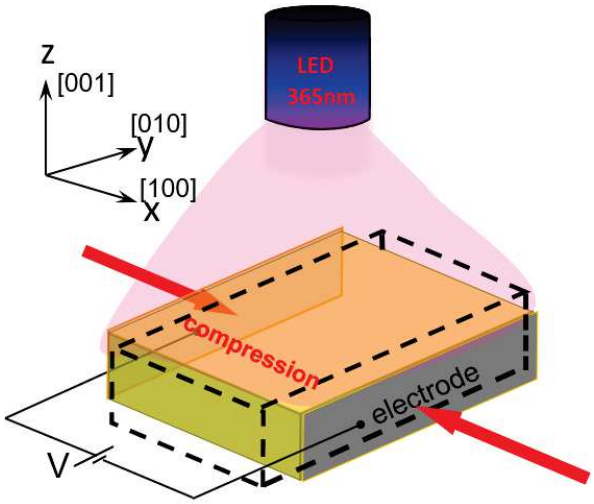

Figure 6.1: Schematics of the compression with respect to crystalline axis of the PMN-PT30% crystal.

As compression increases a clear reduction in the photovoltage is observed (Fig. 6.3).

The V_{oc} values extracted at the given intensity from these measurements are plotted against the relative deformation in Fig. 6.4. After stressing the sample the initial state was recovered, therefore the experiment was proven to be in the elastic regime (see Fig. 6.2) and no detectable damage occurred.

The effect of the external strain on photovoltaic properties of PMN-PT crystals is not known in literature to the best of this author knowledge and only tentative explanation can be made at this stage. The first possibility is that certain crystalline symmetries are more favourable for photovoltaics then others due to possible modification in the bandgap. Indeed, we have demonstrated this by the temperature dependent studies (see Chapter 5) exploiting the series of phase transitions in these successful compounds. Another related explanation can be given taking into account the energy

required to expulse by light initially bonded charges in the crystalline lattice. It can be tentatively assumed that in the compression state the Van-der Waals-type of inter-atomic interactions (which depend on distance, $E \sim r^{-6}$) are stronger and therefore unfavourable for photovoltaics. If this is true, the increase in the inter-atomic distances should have an opposite effect to the one induced by the dominant compression (i.e. increase of the PV effect). Because the tension is technically difficult to apply to the sample – the alternative procedure described in the next section have been used.

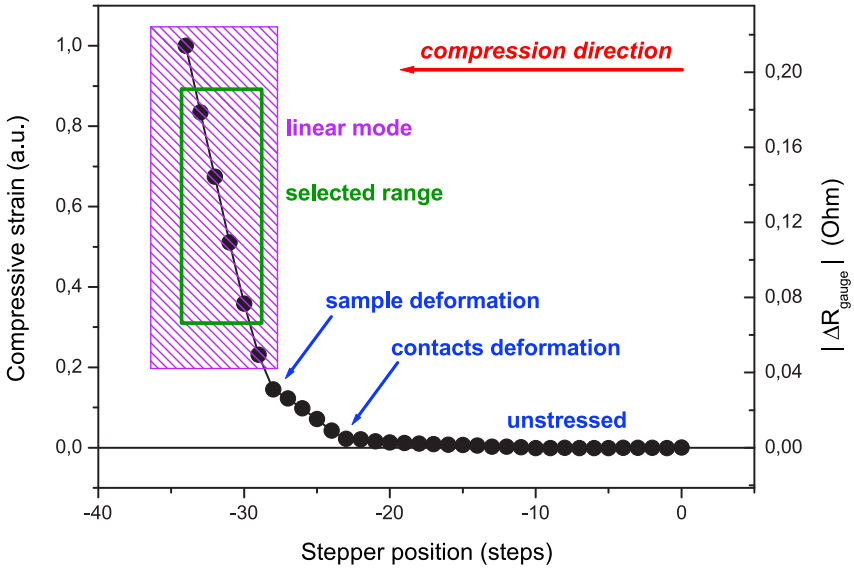

Figure 6.2: Stepper motor calibration. Magenta box shows elastic regime of sample deformation. Green rectangle represents the strain range selected for the stress dependent studies.

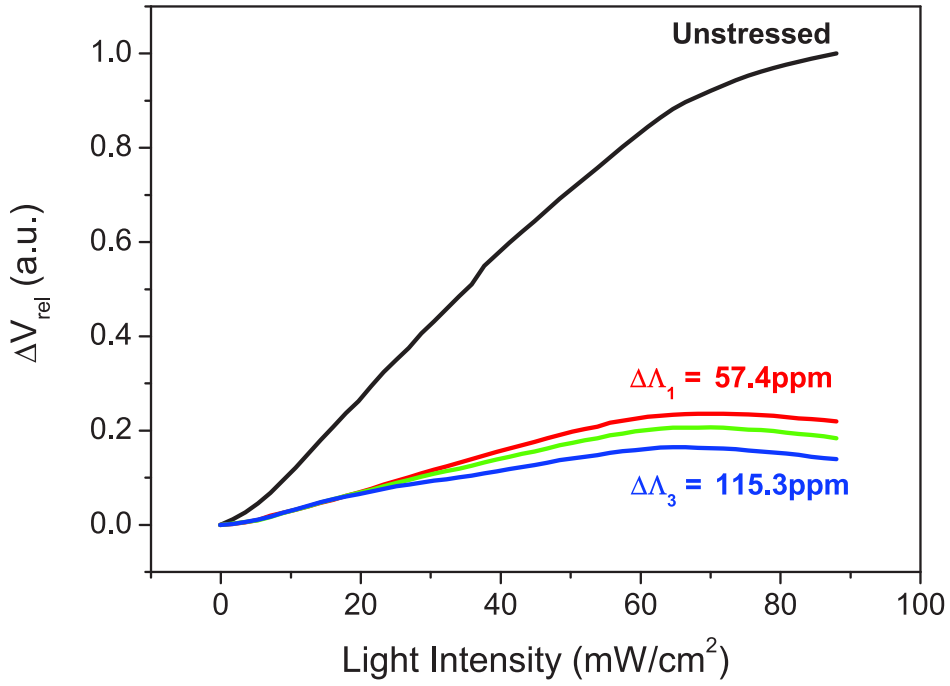

Figure 6.3: Transient part of PMN-PT30% photovoltage (scaled to the maximum in unstressed state) in unstressed state and under three different strain values.

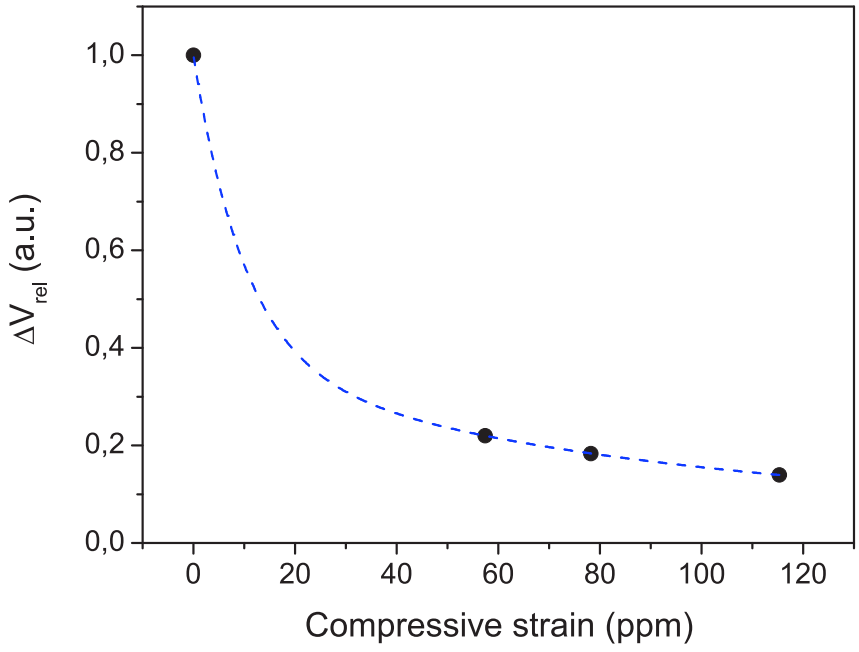

Figure 6.4: PMN-PT30% photovoltaic effect tuning by compressive strain (ppm defined in Eq. (2.17)).

6.2 Triaxial tensile strain (Tension by vacuum)

To introduce tension regarding ambient pressure the samples was placed in the vacuum. To this end the sample was placed into *INSTEC* cryostat with an optical window for optical excitation. The light power loss via the optical window was evaluated to be less than 5% and was corrected for the resulting light intensity used for sample excitation. The change in voltage induced by light was monitored along the same direction while illuminating the sample from a top (same geometrical conditions). Interestingly, indeed the increase of PV effect has been detected under pumping (Fig. 6.5 and Fig. 6.6). The both compounds increase PV effect with reduction of atmospheric pressure. Interestingly, the PMN-PT30% crystal where piezoelectric effect is larger, show a larger (23%) increase in PV response.

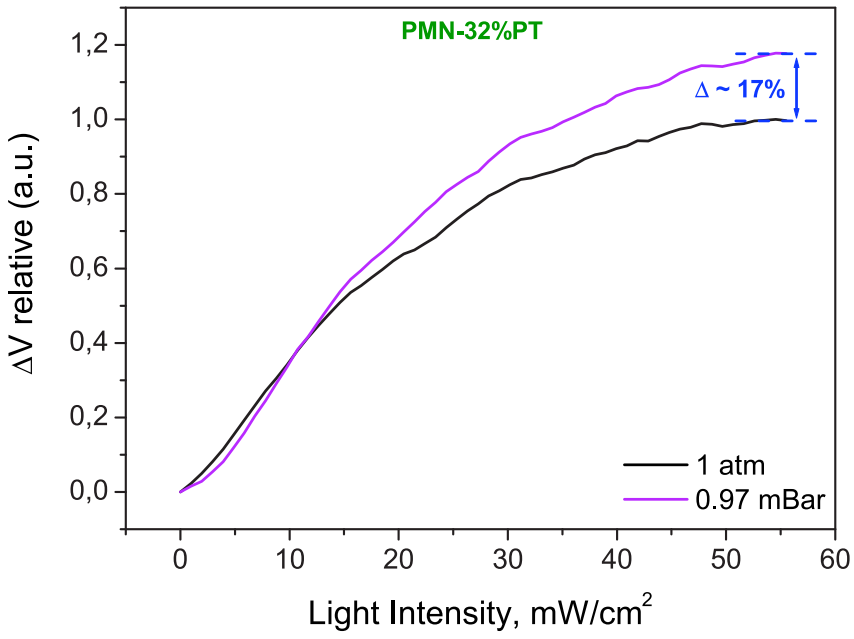

Figure 6.5: PMN-PT32% photovoltaic effect tuning by pressure.

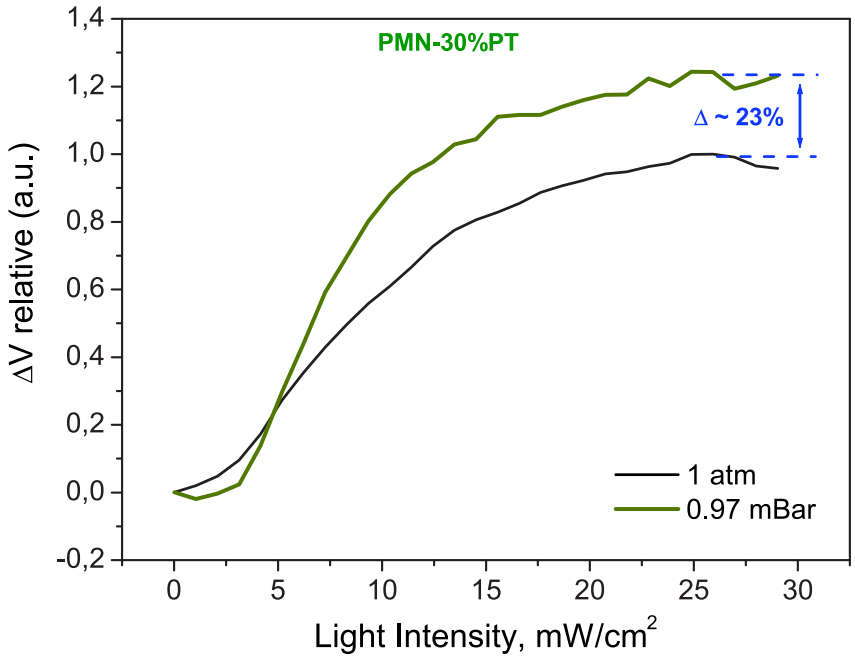

Figure 6.6: PMN-PT30% photovoltaic effect tuning by pressure.

6.3 Conclusions

Motivated by piezoelectric properties of the investigated compounds the investigation of the deformation dependent photovoltaic properties revealed highly strain dependent PV performance. The compression in elastic regime largely reduces the PV effect reaching the saturation near 70 ppm. Although, at this stage the exact mechanism of this effect is unclear, it is logical to assume that the stress can make the system more, or less acentric. The possible role of interatomic bonds in the observed effect can also be considered. While compression (smaller interatomic distances) decreases the PV effect the opposite expansive effect induced by vacuum does the opposite. However, additional experiments are required to establish the reliable conclusion. Interestingly, the PV effect in the crystal with larger piezoelectric properties is more sensitive to the deformation comparing to its less piezoelectric counterpart. The reported above functionaries should also contribute to understanding the role of piezoelectricity in the PV effect.

Chapter 7

Conclusions and perspectives

Unlike relatively well-established semi-conductive PV industry, the ferroelectric-based photovoltaics is still under the way for maturity. In this respect examining fundamental PV properties of FE requires inexpensive materials, preferably in single crystal form, to sort out possible extrinsic contributions related to the solar cell design. Therefore, finding new photovoltaic compounds among inexpensive and widely available ferroelectric crystals should be regarded as an important result contributing to the state-of-the-art in the field of photovoltaicity of ferroelectrics. Although the photovoltaic efficiency remain low in the reported here compounds (comparing to other materials, see Table 1.1), the reported here PMN-PT crystals can serve as a model materials allowing for fundamental insight into the photovoltaic property in FE.

Firstly, the PMN-PT32% was found to be photovoltaic with the much larger effect than for the related WO_3-doped PMN-PT36% compound, demonstrating that the doping is not indispensable PV condition for this family of crystals. Afterwards, another member of this family the PMN-PT30% was chosen for PV investigations due to its particular position on the phase diagram. The PMN-PT30% was found to show a ~ 20 times larger photovoltages. The both compositions were further studied in order to demonstrate the possibility of tuning their photovoltaic properties by the external stimuli methods: electric field, ferroelectric history, light intensity, temperature and even mechanical stress. The ferroelectric characterization under light and in darkness demonstrated widening of FE loops for both compounds under UV illumination. From such measurements the difference between FE current under light and in darkness, first of all, revealed the hysteretic nature of the PV effect with a clear hysteresis in photocurrent.

Secondly, the photocurrent found to be maximal near the electric field corresponding to FE dipole reorientation. The hysteretic nature is of great importance because it results in the electric field tuning of the PV response. The hysteretic nature and electrical tubability features have been verified and confirmed also for the BFCO films, known to be closer for industrial applications. Obtained results clearly show a large tunability potential of FE and photovoltaic materials by electric field. The measured poling dependence of the PV parameters confirms the PV effect increase with increasing polarization (i.e. intrinsic electric field).

The third outcome of electrical characterization concerns FE domains. The depolarized state clearly affects the photovoltaic effect and different spontaneous states (domains configuration) can have different PV response. However, proper electric poling can overcome in magnitude the PV effect of spontaneous FE state containing domains. This feature is expected to be a general and technologically important for many photovoltaic ferroelectric compounds. Also asymmetry of the FE coercive field with regard to zero bias should be taken into account because electrical poling of the same magnitude, but different sign can result in different PV response.

The light intensity dependent characterization of the PV effect in FE is also particular. The light intensity dependent studies extracted from the current-voltage characteristics show a classical behaviour with approach to saturation. However, such measurements involve both electrical and optical excitations at the same time, unfavourable for separate study of the optical effect. For pure optical excitation the intensity dependence should be preferably measured at zero external applied field in the well-defined FE state. In this case the dynamics of photo-carriers clearly involving charge generation and distribution processes can be revealed. Interestingly, the zero bias measurements also manifests the fascinating FE-state dependence, demonstrating that larger intrinsic electric field is advantageous for PV effect. Not only light-induced charge generation, but also post-recombination processes, yet occurring at different time scales can govern the photo-response. Consequently, reducing recombination centres should result in their efficiency improvement.

For the both studied PMN-PT compounds with 32% and 30% of PT the PV properties exist in a wide temperature range well above room temperature, making them possible candidates for PV cells components. The PV effect disappears when crystals are warmed above corresponding FE Curie temperature where structure becomes centrosymmetric, confirming that PV origin in FE is related to acentric polar struc-

tures. As temperature increases, each sequential acentric crystalline phase manifests a modified PV response. Moreover, all structural transitions show singularities in PV properties reducing or increasing the PV effect. Such structural dependent effects deserve a separate study for establishing on-demand PV property engineering. Just before the FE Tc the photovoltaic effect increases more than two times for the 32% compound and can be assumed to be a general FE feature in PV FE. Indeed, the similar increase was also detected for the PMN-PT30% crystal near Tc. Such an increase of PV near Tc, where fluctuations of primary order parameter start to occur, can be qualitatively understood in terms of driving the sample out of thermodynamic equilibrium where system becomes more sensitive to external perturbations. These observations suggest the technologically important way to increase PV effect in FE.

Fact that more piezoelectric compound also shows a larger PV response should also be taken into account for the FE solar cell development. In attempt to verify if piezoelectric susceptibility can be used as an additional tuning parameter of PV properties the deformation dependent studies have been conducted. The compression in the elastic regime largely reduces the PV effect. However, vacuum induced lattice expansion increases the PV response. Additionally, the PV effect in the crystal with larger piezoelectric properties is more sensitive to the deformation comparing to its less piezoelectric counterpart: the same deformation level does bigger impact on the PV effect in the more piezoelectric PMN-PT30% compound. Consequently, the reported here strain dependent functionalities should add a new degree of freedom to the PV tunability.

Although the discovered PV effect is more than one order of magnitude larger in spectral efficiency than for previously reported WO_3 doped PMN-PT [153], it still remains far from applications in PV. In this respect one should mention that PV effect is known to be thickness dependent[198]. While transversal geometry used here with respect to light propagation is favourable to avoid extrinsic contributions the longitudinal geometry should offer yet larger PV effect.

More generally, the results obtained during this PhD thesis clearly provide a roadmap for the large tunability of PV properties in FE that arises from the ferroelectric nature of these compounds. The results can stimulate the scientific community for additional studies of similar FE materials and to expand the existing BPVE models. More generally, by combining different strategies, as above mentioned, the photovoltaic response can be greatly enhanced.

7.1 Optical magnetization control (MRAM)

The PMN-PT complex was optimized to deliver the high electrostriction and, as it was shown here, it also can change polarization under light. So the reasonable action is to take advantage of these properties to control, for example, magnetic anisotropy either via direct or strain-mediated mechanisms. Being combined with the strain sensitive (due to magnetostriction effect) magnetic structure: single layer (like BFO+Ni [13], PMN-PT30%+Ni [199] see Figure 7.1) or, for optimization purposes, multilayer GMR/TMR structures. Such "sandwich" structure allows the optical control (writting and possibly erasing, under certain conditions) with electrical readout (and erasing) of saved information. This type of a device could be used in non-volatile magnetic storages (preferred due to speed considerations) and MRAM.

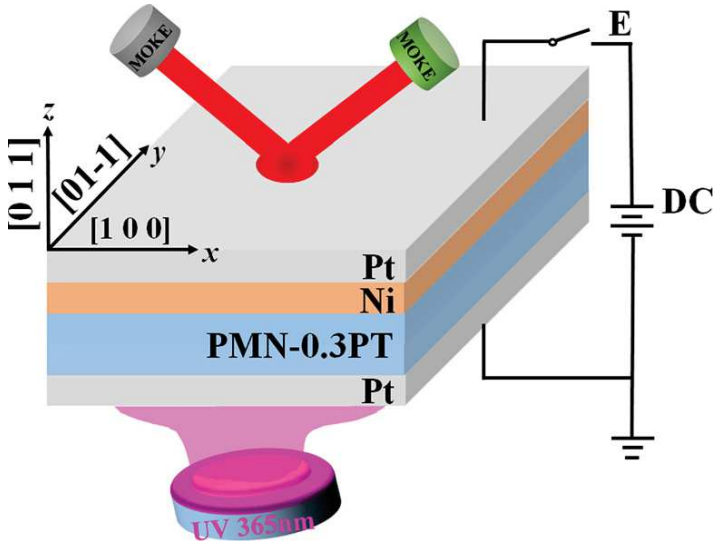

Figure 7.1: Experimental setup for strain-mediated control of magnetization (taken from [199]).

7.2 Optical control of charge-sensitive structures

The possibility of optical control of electrical polarization can be magnified and detected by 2D overlayers. As was showed in[200], specifically designed optical stimulus modifies the surface charges density. Thus, with an appropriate deposited structure, forming a memory cell. For this role, graphene is the best candidate, as it possesses both the high doping and strain (another ferroelectric degree to use) sensitivity. These stimuli modify its conductivity and such change is registered electrically (resistance change $\rightarrow$ voltage variation $\rightarrow$ ADC/comparator capture). This design characterised by the all-optical control (full write/erase) and electrical readout (and possible erasing) of saved information.

As it follows from our recent publication[145], light intensity can become an additional degree of freedom exploiting the light-dependent photo-depolarization effect in PMN-PT crystals opening the selective charge trapping possibility. Such mechanism is very beneficial as it allows changing the graphene doping (interfacial charges density) and thus offers the multiple resistive states (useful for new generation of high density information storage) and one can move the working point to the desired resistance level (increasing the signal-to-noise ratio and readout speed), see Figure 7.2. This light-induced charge generation process occurs at intensities $< 20\,mW/cm^2$ (leading to the decrease in graphene resistance) and eventually reaches its saturation at larger intensities (graphene's layer resistance increases) when the excess photo-carriers start to recombine, thus reducing the remanent polarization, which is reflected in the resistance readout of the graphene overlayer (see Fig. 7.3). Because some of the charges have recombined irreversibly the repeatable optical writing of the graphene resistive state becomes possible. Moreover, by finely controlling the illumination intensity (and more generally, its history) one finds the balance between these two competing processes and gets a control over the doping procedure. Taking for example two light intensities and a single-pulse approach, the resulting resistance switching is demonstrated by Fig. 7.4.

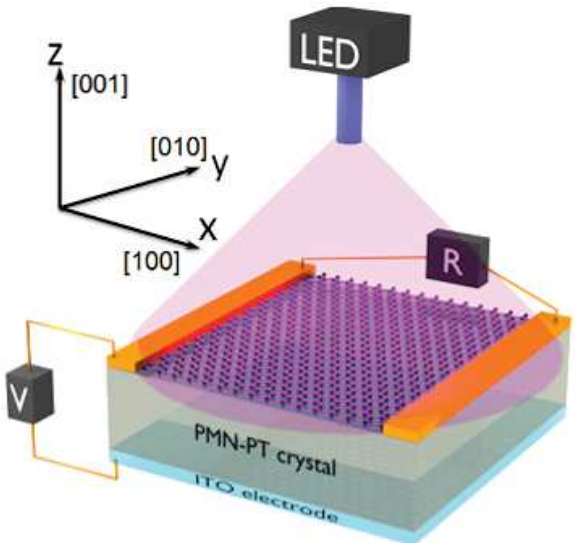

Figure 7.2: Experimental setup for PoC.

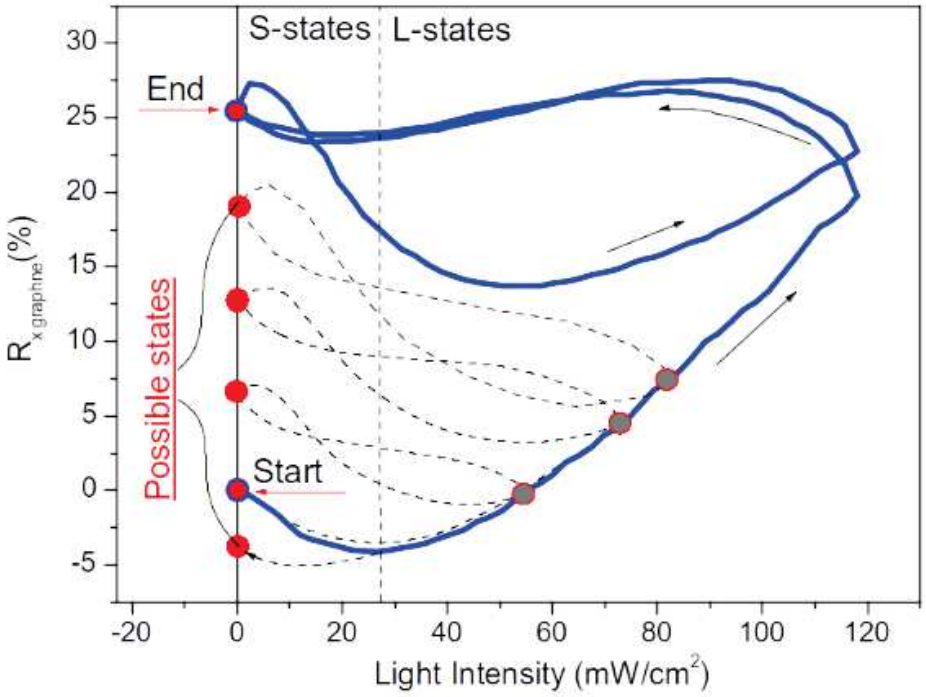

Figure 7.3: Light intensity sweeps that demonstrate the existence of multiple light written states (depending on the maximum light intensity).

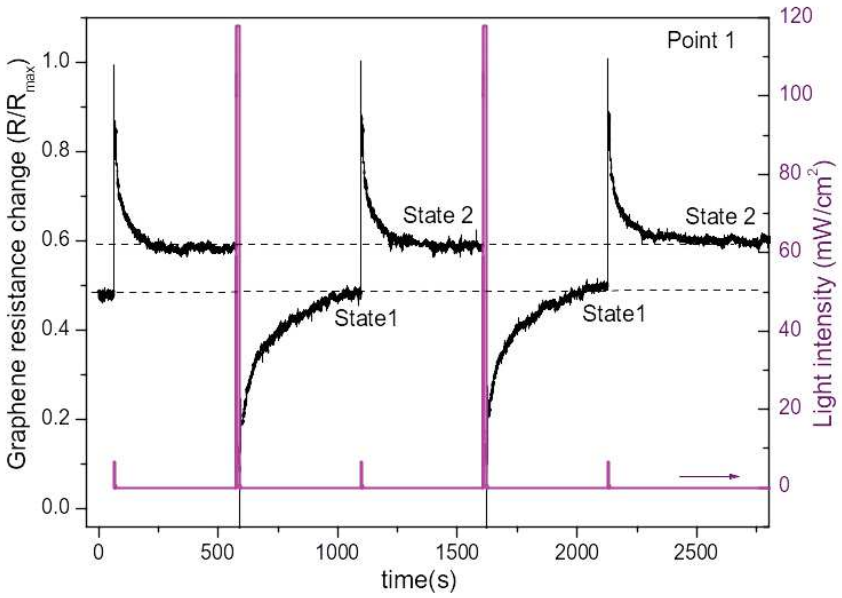

Figure 7.4: Optical writing and erasing of graphene resistive states with UV light.

List of publications

1. **A. S. Makhort**, F. Chevrier, D. Kundys, B. Doudin and B. Kundys, *"Photovoltaic effect and photopolarization in $Pb[(Mg_{1/3}Nb_{2/3})_{0.68}Ti_{0.32}]O_3$ crystal"*, Phys. Rev. Materials, **2**, 012401, 2018

2. A. Quattropani, **A. S. Makhort**, M. V. Rastei, G. Versini, G. Schmerber, S. Barre, A. Dinia, A. Slaoui, J.-L. Rehspringer, T. Fix, S. Colis and B. Kundys, *"Tuning photovoltaic response in Bi_2FeCrO_6 films by ferroelectric poling"*, Nanoscale, **10**, 13761-13766, 2018

3. **A. Makhort**, G. Schmerber and B. Kundys, *"Larger photovoltaic effect and hysteretic photocarrier dynamics in $Pb[(Mg_{1/3}Nb_{2/3})_{0.70}Ti_{0.30}]O_3$ crystal"*, Mater. Res. Express, **6**, 066313, 2019

4. D. Kundys, A. Cascales, **A. S. Makhort**, H. Majjad, F. Chevrier, B. Doudin, A. Fedrizzi, B. Kundys, *"Optically Rewritable Memory in a Graphene-Ferroelectric-Photovoltaic Heterostructure"*, Phys. Rev. Applied, **13**, 064034, 2020

Résumé en français

Introduction

La demande toujours croissante de sources d'énergie propres et efficaces identifie l'industrie photovoltaïque comme une solution alternative importante. Cependant, de nos jours, le marché photovoltaïque est dominé par les cellules solaires constituées de semi-conducteurs. Cette industrie est actuellement face à sa limite fondamentale d'efficacité pour l'architecture à bande interdite unique. Donc, le développement de nouveaux paradigmes et matériaux de cellules PV devient un défi de recherche important. Les matériaux ferroélectriques sont des candidats intéressants pour les futures applications PV en raison de leur potentiel de dépasser les limites fondamentales de la bande interdite simple de cellules solaires conventionnelle à base de semi-conducteurs. Bien que l'effet photovoltaïque dans les ferroélectriques ait été démontré par Chynoweth [1] en 1956, le nombre de composés PV connus est actuellement bien au dessous de 40. La renaissance dans ce domaine de la recherche a commencé après la découverte de l'effet PV dans le multiferroïque $BiFeO_3$[2]. Depuis, nous témoignons des nombreux rapports chaque année consacrés aux matériaux et structures photovoltaïques ferroélectriques contribuant au développement d'un domaine de recherche intéressant en science des matériaux. Un tel intérêt rapidement croissant est d'une coté le résultat de la consommation d'énergie au cours de la dernière décennie (croissance rapide de l'infrastructure d'Internet : centres de données, serveurs, appareils IoT et autres, nécessitent plus d'électricité chaque année) et d'autre part, une volonté de réalisation d'un concept énergétique respectueux de l'environnement. La tendance générale de la

recherche sur le photovoltaïque est très bien illustrée par le nombre d'articles de recherche publié chaque année, voir Fig. 8.1 (les données ont été obtenues à partir de l'archive WebOfScience).

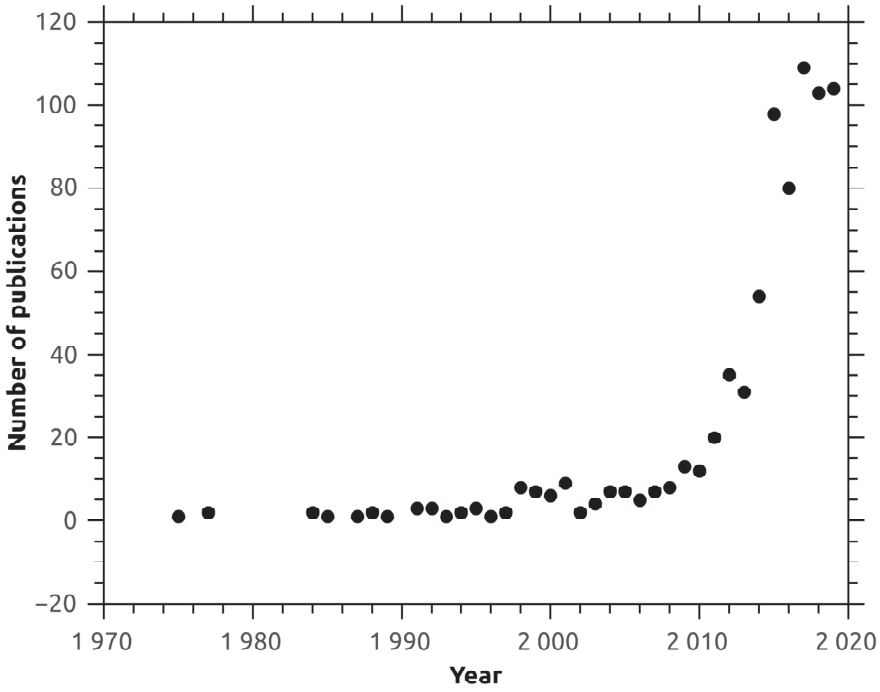

FIGURE 8.1 : Schéma illustrant un intérêt croissant pour les matériaux FE et photovoltaïques.

Puisque la valeur de la tension générée par une cellule semi-conductrice de type p-n ne peut pas dépasser sa valeur de bande interdite, la technologie nécessite maintenant une réalisation d'architectures de plus en plus compliquées, impliquant des approches multi-bandes. Cependant, cette stratégie augmente les coûts et provoque des problèmes d'endurance des cellules solaires, donc les solutions et matériaux alternatifs doivent être adaptés. Parce que les paires électron-trou sont séparées seulement dans une région étroite à l'intérieur de la jonction p-n, l'architecture à bande interdite unique est fondamentalement limité à PCE = 33.7% par une limite de Shockley-Queisser [3]. Ce se traduit par une efficacité de séparation plus faible et stimule la conception des structures avec plusieurs jonctions p-n dans la cellule. Par conséquent, les matériaux électriquement polaires où chaque cellule unitaire cristalline peut générer des charges (et une séparation de charge se produit dans la masse en raison de l'existence d'une polarisation électrique), voir Fig. 8.2, sont des candidats intéressants pour de futures

applications photovoltaïques.

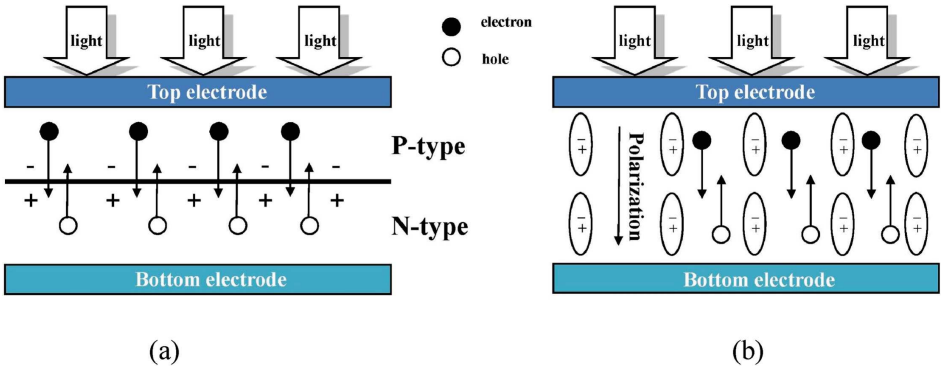

FIGURE 8.2 : Illustration d'une principe de fonctionnement d'un semi-conducteur classique à bande interdite unique. Cellule de type p-n (a) et celle basée sur FE (b). Image de la réf. [4].

Bien que une séparation de charge plus efficace et des photo-tensions plus importantes sont avantageux dans ces matériaux, comprendre les propriétés physiques pour adapter leur réponse photovoltaïque reste moins connu. Les expériences consacrées à la compréhension de base des propriétés physiques doivent être ciblées sur les composés modèles les plus simples possibles et les plus largement disponibles, pour éviter les contributions extrinsèques. Par conséquent, ces thèses, tout d'abord, rapportent les deux nouveaux composés photovoltaïques qui sont largement disponibles et peu coûteux et deuxièmement, aborde également les problèmes de réglage PV en ferroélectrique ainsi que la dynamique des porteurs de charge induite par la lumière. La nature d'hystérésis de la réponse photovoltaïque est révélée. Avec le caractère non linéaire de l'effet PV en fonction de l'intensité lumineuse, nos résultats permettent d'optimiser les performances PV des futures cellules solaires à base de matériaux ferroélectriques. En plus de la description des deux nouveaux composés PV de la famille cristaux ferroélectriques PMN-PT, il est démontré la possibilité d'influencer propriétés photovoltaïques dans les ferroélectriques par des stimuli externes, comme le champ électrique, l'histoire ferroélectrique, l'intensité lumineuse, la température et les contraintes mécaniques. Il est illustré comment la réponse photovoltaïque peut être améliorée en combinant différentes stratégies.

Influence de la température sur l'effet photovoltaïque

Les cellules PV à base de semi-conducteurs réduisent généralement leurs performances avec l'augmentation de la température en raison de l'augmentation des taux de recombinaison des porteurs internes [195]. Cependant, dans le cas de matériaux photovoltaïques FE plus isolants, la dépendance de l'effet PV à la température est moins connue. En fait, dans le cas des matériaux PV et FE, l'effet PV n'est attaché et supposé exister que dans les structures cristallographiquement acentriques. De plus, différents types de structures acentriques peuvent être plus, ou moins favorables aux effets PV comme cela sera indirectement souligné dans le Chapitre 6. De telles structures acentriques peuvent exister dans certaines fenêtres de température et par conséquent, en modifiant de température, on peut changer radicalement la réponse PV. Ce chapitre est consacré à la dépendance de l'effet PV à la température pour les deux composés PMN-PT étudiés. La présence d'un diagramme de phase riche et d'une région MPB dans PMN-PT avec des transitions séquentielles rend ces composés des candidats idéaux pour les études des propriétés PV dépendant de la température.Fridkin *et al*[39] a montré que BPVE dans $LiNbO_3$, $KNb0_3$ et $Ba_{0.25}Sr_{0.75}Nb_20_6$ FE est hautement non linéaire avec la température. Puis Watanabe *et al*[69] ont démontrés le comportement non linéaire de l'effet PV dans les films épitaxiaux PZT/STO. Plus tard, Bogomolov*et al*[80] a montré que la réponse de courant des films ferroélectriques semi-conducteurs $Sn_2P_2S_6$ sous illumination se compose à la fois de composants instationnaires (attribués à l'effet pyroélectrique) et quasi-stables (photovoltaïques). Chacune de ces composants a sa propre dépendance à la température : l'un qui décroît, l'autre – augmente (et atteint son maximum près de la Tc) pendant le chauffage. À son tour, Yang *et al*[84] a rapporté la possibilité d'accorder des propriétés PV (à la fois I_{sc} et V_{oc}) dans les films $BiFeO_3$ monodomaines en fonction de la température. Cependant, la température de

Curie de ce composé est trop élevée pour étudier ce qui se passe près de la transition polaire. Parce que la famille PMN-PT a été considérée principalement dans le contexte de l'utilisation des capteurs/actionneurs, ses propriétés piézoélectriques et diélectriques ont également été bien étudiées en fonction de la température. Les propriétés PV de ces composés n'ayant été signalées que récemment, leur dépendance à la température était inconnue. Pour combler l'écart dans la compréhension de la dépendance des propriétés photovoltaïque à la température dans ce matériau (compositions : 32% et 30%), les résultats obtenus sont discutés ci-dessous.

Monocristal de $Pb[(Mg_{1/3}Nb_{2/3})_{0.68}Ti_{0.32}]O_3$

D'après les résultats discutés précédemment (voir le Chapitre 3), la réponse PV augmente avec l'augmentation de la tension de polarisation et atteint son maximum dans l'état monodomaine. Dans cet état, les propriétés PV deviennent dépendantes de la réorganisation de la structure cristalline pendant les transitions de phase en raison des changements du champ électrique intrinsèque. L'état monodomaine ferroélectrique devient également bénéfique car il élimine un paramètre supplémentaire (structure des domaines ferroélectriques sous-coercitifs et sa comportement lors des transitions de phase) et facilite la comparaison des rendements. Par conséquent, avant mesurer, l'échantillon a d'abord été réchauffé dans l'obscurité $19K$ au-dessus de sa température de Curie (Tc $\approx 420K$) puis refroidi sous un champ électrique coercitif appliqué le long de la direction [100]. Le champ électrique a ensuite été mis à zéro et la permittivité diélectrique a été mesurée en fonction du temps pour atteindre la stabilité. La même procédure a été appliquée pour mesurer la polarisation et la charge électrique induite a été surveillée par un électromètre en fonction du temps pour atteindre la stabilité de polarisation isotherme. La dépendance à la température de la permittivité diélectrique et de la polarisation électrique de $Pb\left[(Mg_{1/3}Nb_{2/3})_{0.68}Ti_{0.32}\right]O_3$ est montrée dans Figure 8.3(a). Trois transitions caractéristiques à T_1 ($\approx 352K$), T_2 ($\approx 375K$) et Tc ($\approx 420K$) sont clairement observées dans les deux mesures. Alors que T_2 et Tc sont respectivement liés aux transitions rhomboédrique-tétragonale et tétragonale-cubique [196], l'anomalie liée à la structure des domaines à T_1 est connue d'apparaître comme une fonction de champ électrique [156]. Tenant compte du fait que la lumière peut modifier des températures de transition [182, 183, 197], l'effet photovoltaïque a été mesuré pour plusieurs températures, à proximité des points critiques mentionnés ci-dessus où des anomalies dans les propriétés électriques sont observées. Pour garantir un état FE monodomaine, la même séquence de préparation a été réutilisée. Ensuite, la tension photovoltaïque en fonction de l'intensité lumineuse (plus de détails dans Chapitre 4) a été enregistrée sous chaque valeur de température stabilisée tout en chauffant l'échantillon. De chacune de ces courbes, la partie transitoire (réversible) correspondante a été extraite et tracée (certaines d'entre elles) en fonction de l'intensité lumineuse en mentionnant sa température correspondante (voir Figure 8.4). Les résultats montrent que même à la température ambiante, la partie transitoire (définie à la Section 3.1) de la tension photovoltaïque présente une efficacité spectrale (voir la Section 2.10) supé-

rieure de plus d'un ordre de grandeur à celle du cristal dopé par WO_3précédemment rapporté [153]. Les isothermes photovoltaïques révèlent un comportement non linéaire en fonction de l'intensité lumineuse avec un pic caractéristique. La forme des isothermes suggère l'apparition de deux mécanismes concurrents : la génération de charge induite par la lumière, dominante à de faibles intensités lumineuses, qui se superpose aux processus de recombinaison de charge à des intensités d'éclairage plus élevées. Ces processus opposés donnent lieu au pic en fonction de l'intensité lumineuse à la valeur où les nombres de porteurs générés et recombinés deviennent comparables. Parce que la position du pic en fonction de l'intensité change avec la température la tension maximal générée et sa partie linéaire ont été extraits des isothermes photovoltaïques et tracés en fonction de la température (voir Figure 8.5). L'effet photovoltaïque montre des singularités aux trois températures de transition et révèle plus d'un triple rehaussement près de Tc, puis disparaît dans la région de température paraélectrique. Ce comportement confirme que la photovoltaïcité d'origine ferroélectrique n'existe que dans la phase électriquement polaire. L'effet photovoltaïque généralement plus grand dans la phase tétragonale peut être lié à la plus grande polarisation (dépendance de l'efficacité démontrée dans les Chapitres 3 et 4) dans cette phase et aussi peut être lié à la dépendance attendue de la température de la bande interdite rapportée pour des composés similaires [188].

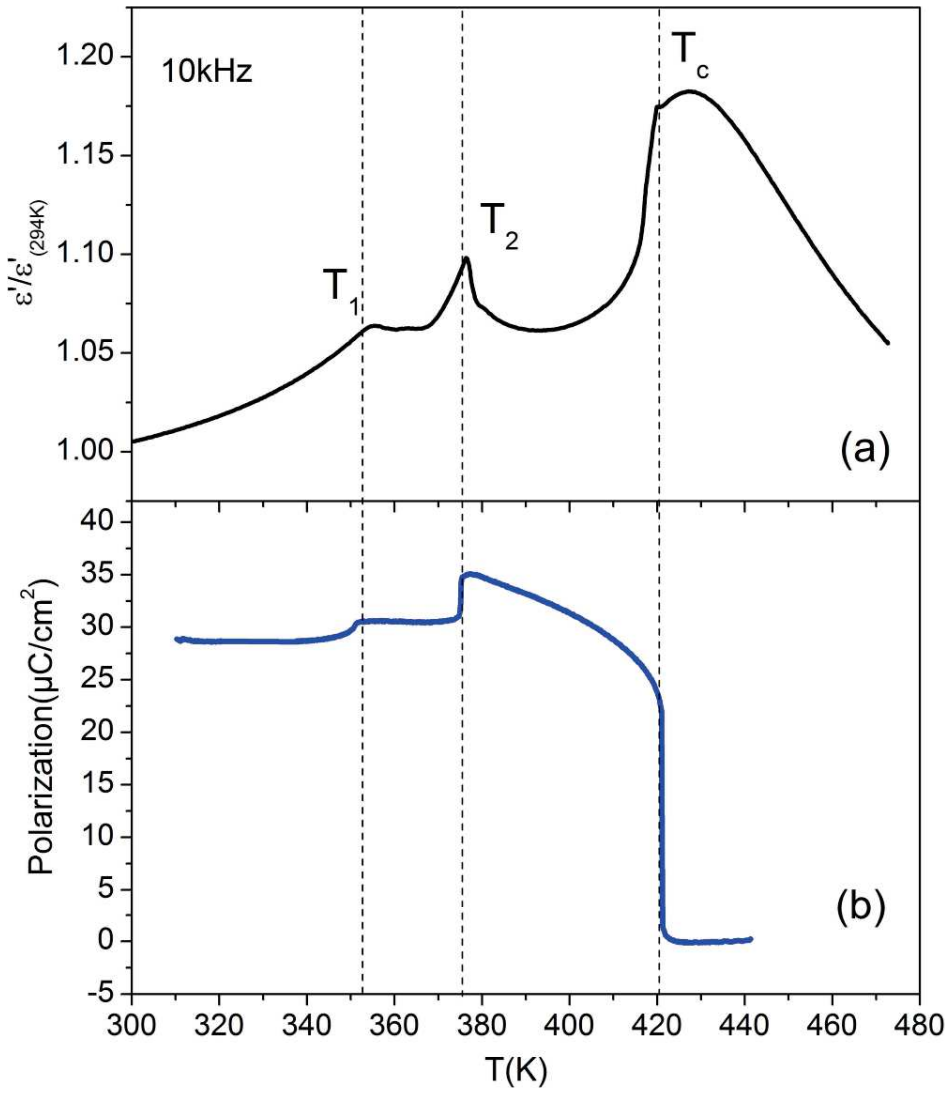

FIGURE 8.3 : Dépendance à la température de la permittivité diélectrique (a) et polarisation (b) d'un composé PMN-PT32%.

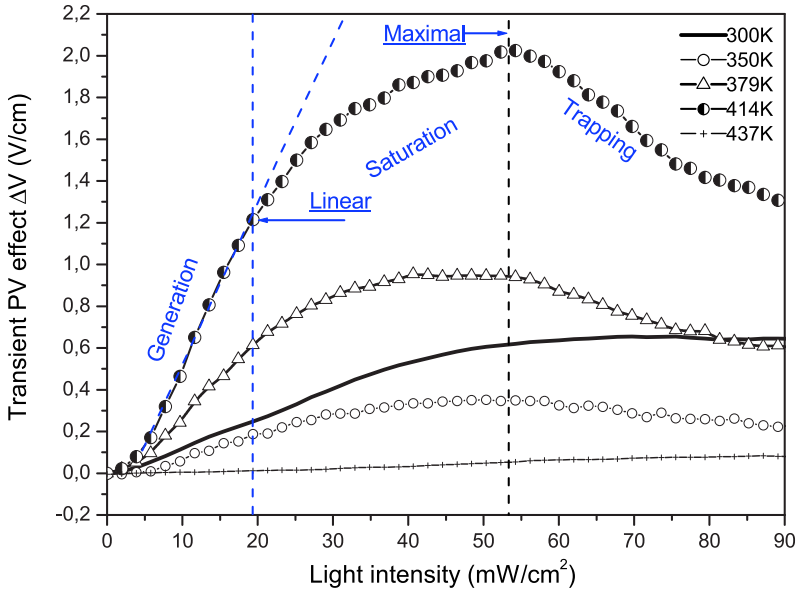

FIGURE 8.4 : La partie transitoire de tension photovoltaïque en fonction de l'intensité lumineuse mesurée pour températures différentes d'un composé PMN-PT32%.

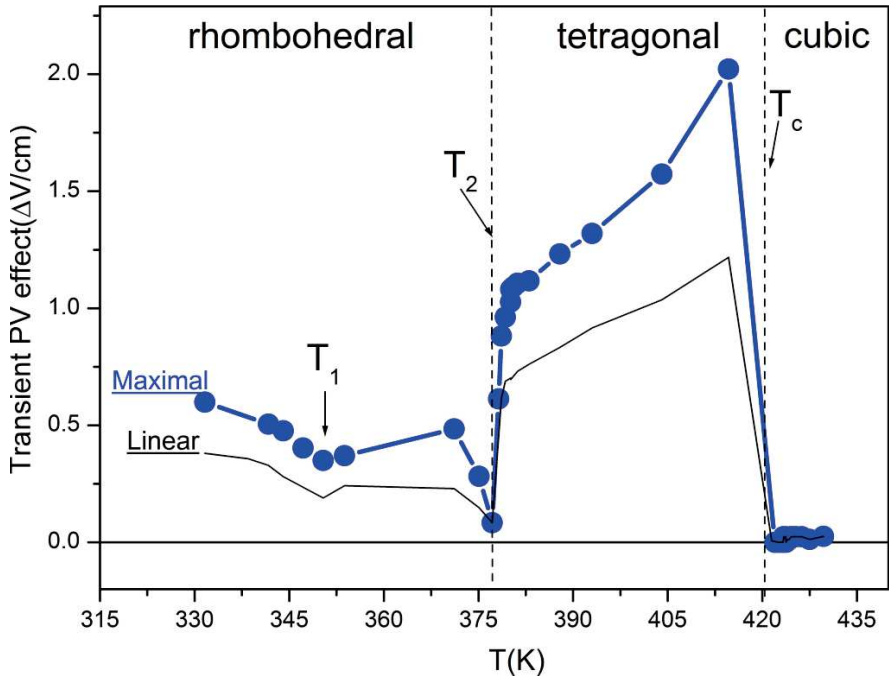

FIGURE 8.5 : Vue sur la dépendance de l'effet photovoltaïque à la température d'un composé PMN-PT32%.

Monocristal de $Pb[(Mg_{1/3}Nb_{2/3})_{0.7}Ti_{0.3}]O_3$

La même séquence de caractérisation a été utilisée pour le composé 30%. Premièrement, l'échantillon a été mis à l'état monodomaine avec le même champ de polarisation et les mêmes vitesses de chauffage – refroidissement. Ensuite, le champ électrique externe a été mis à zéro et la permittivité diélectrique a été mesurée en fonction du temps. Une fois la stabilisation atteinte, les mesures dépendant de la température ont été effectuées. Premièrement, la permittivité diélectrique a été enregistrée dans l'obscurité pendant le chauffage et le refroidissement de l'échantillon (voir Figure 8.6 (a)). La dépendance obtenue montre deux singularités dans la permittivité diélectrique qui manifestent les transitions de phase attendues pour ce composé, suivies d'un pic large (commun pour le relaxeur PMN) à l'état paraélectrique. Pour pouvoir juxtaposer les résultats obtenus, le même état initial doit également être utilisé pour les mesures de polarisation. Après la stabilisation de l'état monodomaine préparé et confirmée par les mesures de polarisation en fonction du temps, l'évolution de la polarisation en fonction de la température a été évaluée dans l'obscurité en chauffant l'échantillon (voir Figure 8.6 (b)). La polarisation montre les transitions de phase correspondantes avec une légère amélioration dans la phase tétragonale et disparaît à la température de Curie. La même procédure a été menée pour les mesures de tension photovoltaïque en fonction de la température (voir Figure 8.7) dans les mêmes conditions de polarisation et d'éclairage que celles évoquées précédemment. La courbe montre une grande amélioration de tension photovoltaïque dans la phase tétragonale. Cet effet pourrait être lié à la polarisation plus élevée à cette phase (due au réarrangement du réseau) et aux variations de la bande interdite près de la température de Curie.

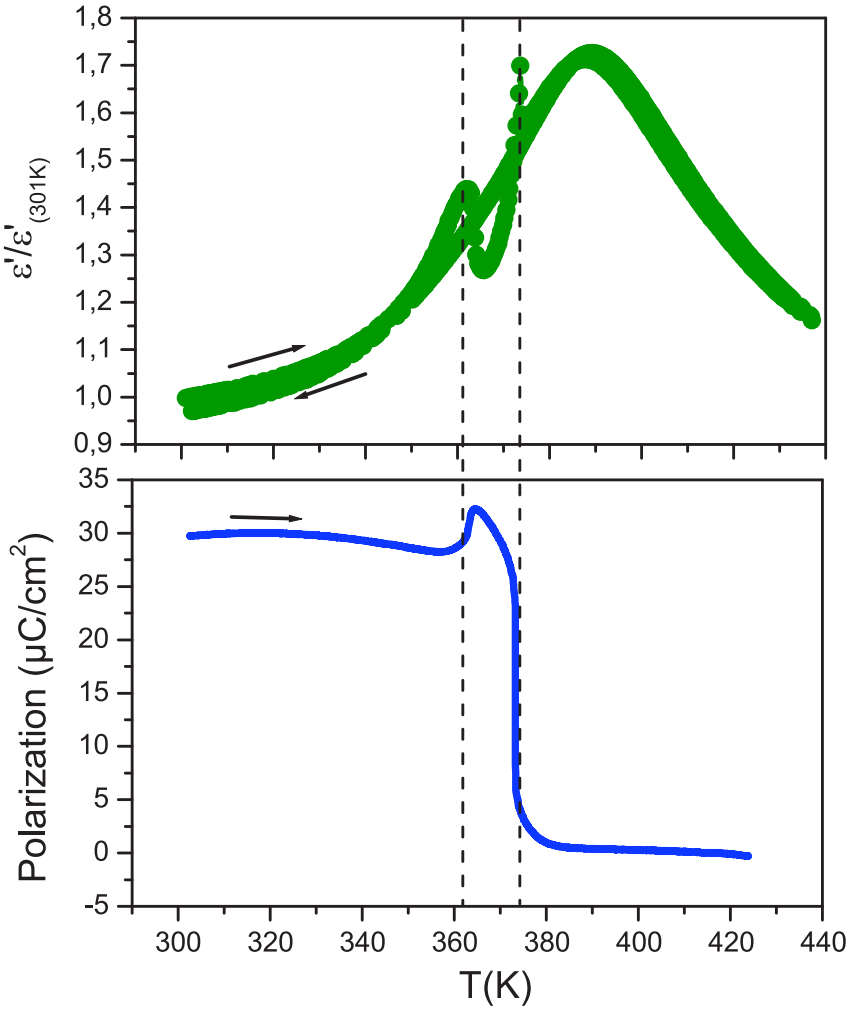

FIGURE 8.6 : Dépendance à la température de la permittivité diélectrique (a) et polarisation (b) d'un composé PMN-PT30%.

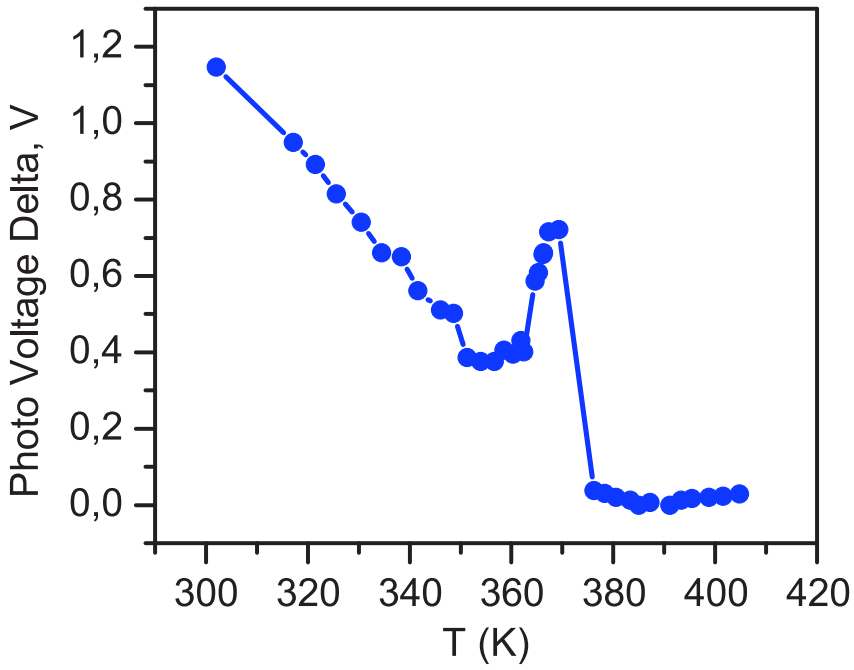

FIGURE 8.7 : Vue sur la dépendance de l'effet photovoltaïque à la température d'un composé PMN-PT30% (la longueur de l'échantillon était de 1,6 mm).

Conclusions

Pour conclure cette section, on peut tout d'abord souligner que l'effet PV trouvé dans les deux composés étudiés avec des compositions de 32% et 30% persiste dans une large gamme de températures au-dessus de la température ambiante. L'effet PV disparaît lorsque les cristaux sont chauffés au-dessus de leur température de Curie FE correspondante où la structure devient centrosymétrique. Bien qu'une très petite photo-réponse (voir l'isotherme de 437 K sur la Figure 8.4) puisse encore être observée juste après la transition polaire à non polaire, elle disparaît avec un réchauffement supplémentaire. La nette disparition de l'effet photovoltaïque au-dessus de Tc ferroélectrique est une observation importante, confirmant que l'origine de photovoltaïcité dans les matériaux FE est liée aux structures polaires acentriques. Fait intéressant, à mesure que la température augmente, chaque phase cristalline séquentielle manifeste une réponse PV modifiée. De plus, toutes les transitions structurelles montrent des singularités dans les propriétés PV réduisant ou augmentant l'effet photovoltaïque. Ces effets dépendants de la structure méritent une étude séparée pour établir l'ingénierie de propriété PV. Juste avant la Tc FE, l'effet photovoltaïque augmente plus de 2 fois pour le composé à 32% et peut être considéré comme une caractéristique générale des matériaux FE PV. En effet, l'augmentation similaire, bien que moindre, a également été détectée pour le cristal PMN-PT30% proche de Tc. Une telle augmentation de PV près de sa Tc, où les fluctuations commencent à se produire, peut être qualitativement comprise en termes de sortie de l'échantillon de l'équilibre thermodynamique où le système devient plus sensible aux perturbations externes. Bien que plus théorique à l'intérieur serait bénéfique ici, les résultats suggèrent clairement le moyen technologiquement important d'augmenter l'effet PV dans FE en rapprochant le système à sa température de Curie FE. Tous les résultats obtenus démontrent clairement la possibilité d'un réglage de l'effet PV dans nos cristaux FE en fonction de la température et peuvent fournir un moyen pour l'ingénierie PV.

Conclusions générales et perspectives

Contrairement à l'industrie photovoltaïque classique (qui utilise des semi-conducteurs) relativement bien établie, le photovoltaïque à base des matériaux ferroélectriques est encore en cours de maturité. A cet égard, l'examen des propriétés photovoltaïques fondamentales des ferroélectriques nécessite des matériaux peu coûteux, de préférence sous la forme de monocristal, pour exclure les éventuelles contributions extrinsèques liées à la conception d'une cellule solaire. Par conséquent, la découverte de nouveaux composés photovoltaïques parmi les cristaux ferroélectriques largement disponibles doit être considérée comme un résultat important contribuant à l'état de l'art dans le domaine de la photovoltaïcité des ferroélectriques. Bien que l'efficacité photovoltaïque reste faible dans les composés rapportés ici (en comparaison avec d'autres matériaux, voir le Tableau 1.1), les cristaux PMN-PT rapportés ici peuvent servir comme des matériaux modèles permettant des aperçu de la propriété photovoltaïque dans FE.

Premièrement, le PMN-PT32% s'est avéré être photovoltaïque avec un effet beaucoup plus important que pour le composé PMN-PT36% dopé avec WO_3associé, démontrant que le dopage n'est pas la condition indispensable pour avoir l'effet PV dans cette famille de cristaux. Par la suite, un autre membre de cette famille, le PMN-PT30% a été choisi pour les investigations photovoltaïques en raison de sa position particulière sur le diagramme de phase. Il a été constaté que le PMN-PT30% montrait un effet photovoltaïque $\sim$ 20 fois plus grand. Les deux compositions ont été étudiées afin de démontrer la possibilité de régler leurs propriétés photovoltaïques par les méthodes de stimuli externes : champ électrique, histoire ferroélectrique, intensité lumineuse, température et même contrainte mécanique. La caractérisation ferroélectrique sous lumière et dans l'obscurité a démontrée un élargissement des boucles FE pour les deux composés sous éclairage UV. A partir de ces mesures, la différence entre le courant FE sous

la lumière et dans l'obscurité, tout d'abord, a révélée la nature hystérétique de l'effet photovoltaïque avec une hystérésis claire en photo-courant.

Deuxièmement, le photo-courant trouvé est maximal à proximité du champ électrique correspondant à la réorientation dipolaire FE. La nature hystérétique est d'une grande importance car elle entraîne le réglage du champ électrique de la réponse PV. La nature hystérétique et les caractéristiques de réglage électrique ont été vérifiées et confirmées également pour les films BFCO, connus pour être plus proches pour les applications industrielles. Les résultats obtenus montrent clairement un grand potentiel de réglages de l'effet photovoltaïques par champ électrique. La dépendance de polarisation des paramètres PV mesurée confirme l'augmentation de l'effet PV avec polarisation (c'est-à-dire le champ électrique intrinsèque).

Le troisième résultat de la caractérisation électrique concerne les domaines FE. L'état dépolarisé affecte clairement l'effet photovoltaïque et différents états spontanés (configuration des domaines) peuvent avoir une réponse PV différente. Cependant, une polarisation électrique appropriée peut surmonter en amplitude l'effet PV des états spontanés FE (contenant des domaines). Cette caractéristique devrait être générale et technologiquement importante pour de nombreux composés ferroélectriques photovoltaïques. De même, l'asymétrie du champ coercitif FE par rapport à la zéro biais doit être prise en compte car une polarisation électrique de même amplitude, mais un signe différent peut entraîner une réponse PV différente.

La caractérisation dépendante de l'intensité lumineuse de l'effet PV dans FE est également particulière. Les études dépendantes de l'intensité lumineuse extraites des caractéristiques courant-tension montrent un comportement classique avec une approche à la saturation. Cependant, de telles mesures impliquent à la fois des excitations électriques et optiques, défavorables à une étude séparée de l'effet optique. Pour une excitation optique pure, la dépendance d'intensité doit de préférence être mesurée à un champ appliqué externe nul dans l'état FE bien défini. Dans ce cas, la dynamique des photo-porteurs impliquant clairement des processus de génération et de distribution de charge peut être révélée. Fait intéressant, les mesures sous zéro biais manifestent également la fascinante dépendance de l'état FE, démontrant qu'un champ électrique intrinsèque plus grand est avantageux pour l'effet PV. Non seulement la génération de charge induite par la lumière, mais également les processus de post-recombinaison, qui se produisent à différentes échelles de temps, peuvent régir la photo-réponse. Par conséquent, la réduction des centres de recombinaison devrait entraîner une amélioration de

leur efficacité.

Pour les deux PMN-PT composés étudiés avec 32% et 30% de PT, les propriétés PV existent dans une large plage de températures bien au-dessus de la température ambiante, ce qui en fait des candidats possibles pour les cellules photovoltaïques. L'effet PV disparaît lorsque les cristaux sont chauffés au-dessus de sa température de Curie FE correspondante où la structure devient centrosymétrique, confirmant que l'origine de l'effet PV dans les matériaux FE est liée aux structures polaires acentriques. Lorsque la température augmente, chaque phase cristalline acentrique séquentielle manifeste la réponse PV modifiée. De plus, toutes les transitions structurelles montrent des singularités dans les propriétés PV réduisant ou augmentant l'effet PV. Ces effets dépendants de la structure méritent une étude distincte pour établir l'ingénierie de propriété PV à la demande. Juste avant la Tc FE, l'effet photovoltaïque augmente plus de deux fois pour le composé à 32% et peut être supposé être un effet générale dans les FE. En effet, l'augmentation similaire a également été détectée pour le cristal PMN-PT30% proche de sa Tc. Une telle augmentation de PV près de Tc, où les fluctuations du paramètre d'ordre primaire commencent à se produire, peut être qualitativement comprise en termes de sortie de l'échantillon de son état d'équilibre thermodynamique où le système devient plus sensible aux perturbations externes. Ces observations suggèrent le moyen technologiquement important d'augmenter l'effet PV dans FE.

Le fait qu'un composé plus piézoélectrique montre également une réponse photovoltaïque plus grande devrait également être pris en compte pour le développement des cellules solaires ferroélectriques. Pour tenter de vérifier si la susceptibilité piézoélectrique peut être utilisée comme paramètre de réglage supplémentaire des propriétés PV, des études dépendant de la déformation ont été menées. La compression en régime élastique réduit largement l'effet PV. Cependant, l'expansion d'une maille cristalline induite par le vide augmente la réponse PV. De plus, l'effet PV dans le cristal avec des propriétés piézoélectriques plus grandes est plus sensible à la déformation que son homologue moins piézoélectrique : le même niveau de déformation a un impact plus important sur l'effet PV dans le composé $Pb\left[(Mg_{1/3}Nb_{2/3})_{0.7}Ti_{0.3}\right]O_3$ plus piézoélectrique. Par conséquent, les fonctionnalités dépendants de la déformation rapportés ici devraient ajouter un nouveau degré de liberté à l'accordabilité PV.

Bien que l'effet PV découvert soit plus d'un ordre de grandeur plus grand en efficacité spectrale que pour le composé PMN-PT dopé par WO_3 [153] précédemment rapporté, il reste encore loin des applications en PV. A cet égard, il convient de mention-

ner que l'effet PV est connu pour dépendre de l'épaisseur [198]. Alors que la géométrie transversale utilisée ici par rapport à la propagation de la lumière est favorable pour éviter les contributions extrinsèques, la géométrie longitudinale devrait offrir un effet PV encore plus grand.

Plus généralement, les résultats obtenus au cours de cette thèse fournissent clairement une "carte routière" pour la grande accordabilité des propriétés PV en FE qui résulte de la nature ferroélectrique de ces composés. Les résultats peuvent stimuler la communauté scientifique pour des études supplémentaires sur des matériaux FE similaires et pour étendre les modèles BPVE existants. Plus généralement, en combinant différentes stratégies, comme mentionné ci-dessus, la réponse photovoltaïque peut être grandement améliorée.

Contrôle optique de la magnétisation (MRAM)

Le complexe PMN-PT a été optimisé pour fournir une électrostriction élevée et comme cela a été montré ici, il peut également changer de polarisation sous lumière. L'action raisonnable consiste donc à tirer parti de ces propriétés pour contrôler, par exemple, l'anisotropie magnétique soit via des mécanismes directs ou à médiation par la déformation. Étant combiné avec la structure magnétique sensible à la déformation (due à l'effet de magnétostriction) : monocouche (comme BFO + Ni [13], PMN-PT30% + Ni [199] voir Figure 8.8) ou, à des fins d'optimisation, des structures GMR/TMR multicouches. Une telle structure "sandwich" permet le contrôle optique (écriture et éventuellement effacement, sous certaines conditions) avec lecture électrique (et effacement) des informations sauvegardées. Ce type de dispositif pourrait être utilisé dans des stockages magnétiques non volatils (préférés en raison de considérations de vitesse) et dans la MRAM.

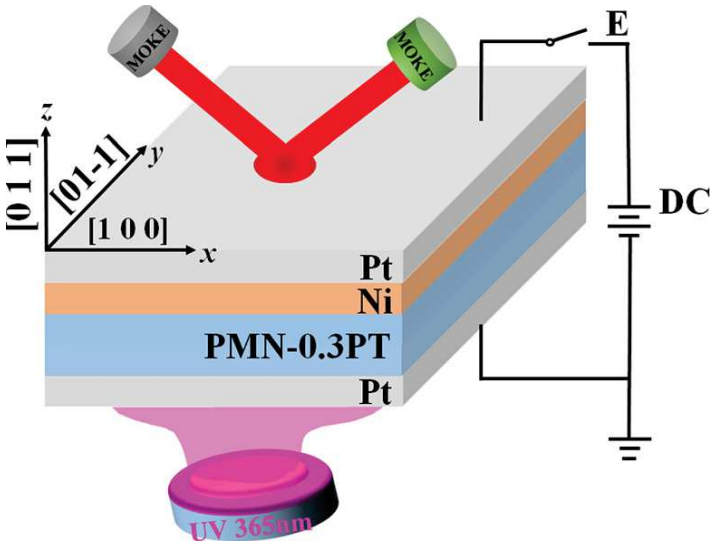

FIGURE 8.8 : Configuration expérimentale pour le contrôle de la magnétisation par déformation (extrait de [199]).

Contrôle optique des structures sensibles à la charge

La possibilité de contrôle optique de la polarisation électrique peut être amplifiée et détectée par des superpositions 2D. Comme cela a été montré dans [200], un stimulus optique spécialement conçu modifie la densité des charges de surface. Ainsi, avec une structure déposée appropriée, on forme une cellule mémoire. Pour ce rôle, le graphène est meilleur candidat, car il possède à la fois une sensibilité élevée au dopage et à la déformation (un autre degré ferroélectrique à utiliser). Ces stimuli modifient sa conductivité et un tel changement est enregistré électriquement (changement de la résistance $\rightarrow$ variation de la tension $\rightarrow$ ADC/comparateur). Cette conception se caractérise par le contrôle entièrement optique (écriture / effacement complet) et la lecture électrique (et l'effacement possible aussi) des informations enregistrées.

Comme il ressort de notre récente publication [145], l'intensité lumineuse peut devenir un degré supplémentaire de liberté en exploitant l'effet de photo-dépolarisation dépendant de la lumière dans les cristaux PMN-PT ouvrant la possibilité de piégeage de charge sélective. Un tel mécanisme est très bénéfique car il permet de changer le dopage du graphène (densité de charges interfaciales) et offre ainsi les multiples états résistifs (utiles pour la nouvelle génération de stockage d'informations à haute densité) et on peut déplacer le point de travail au niveau de résistance souhaité (en augmentant le rapport signal / bruit et vitesse de lecture), voir Figure 8.9. Ce processus de génération de charge induite par la lumière se produit à des intensités $< 20\,mW/cm^2$ (conduisant à la diminution de la résistance du graphène) et atteint finalement sa saturation à des intensités plus importantes (la résistance de la couche de graphène augmente) lorsque les photo-porteurs en excès commencent à se recombiner, réduisant ainsi la polarisation rémanente, qui se reflète dans la lecture de la résistance de la surcouche de graphène (voir Fig. 8.10). Du fait que certaines des charges se sont recombinées de manière irréversible, l'écriture optique répétable de l'état résistif du graphène devient possible. De plus, en contrôlant finement l'intensité d'éclairage (et plus généralement son historique) on trouve l'équilibre entre ces deux processus concurrents et obtient un contrôle sur la procédure de dopage. En prenant par exemple deux intensités lumineuses et une approche à impulsion unique, la commutation de résistance résultante est démontrée par Fig. 8.11.

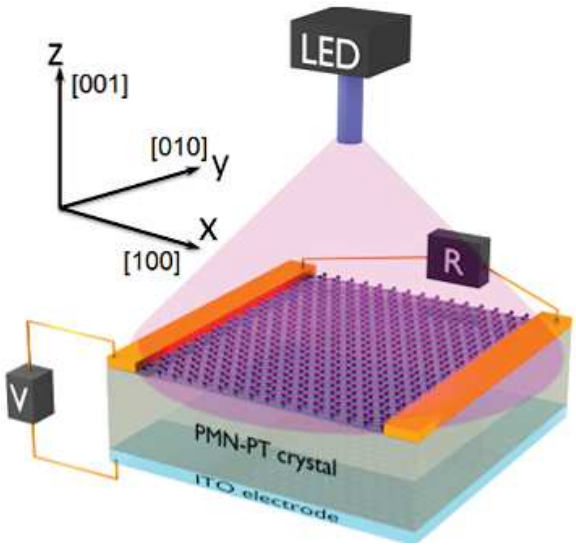

FIGURE 8.9 : Configuration expérimentale pour la preuve de concept.

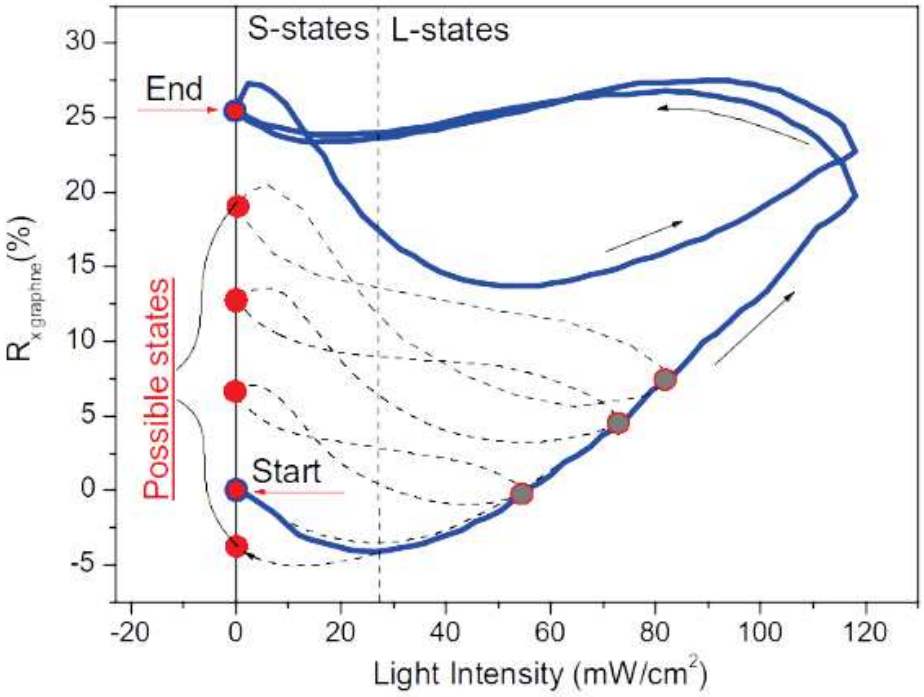

FIGURE 8.10 : Balayages d'intensité lumineuse qui démontrent l'existence de plusieurs états écrits par la lumière (en fonction de l'intensité lumineuse maximale).

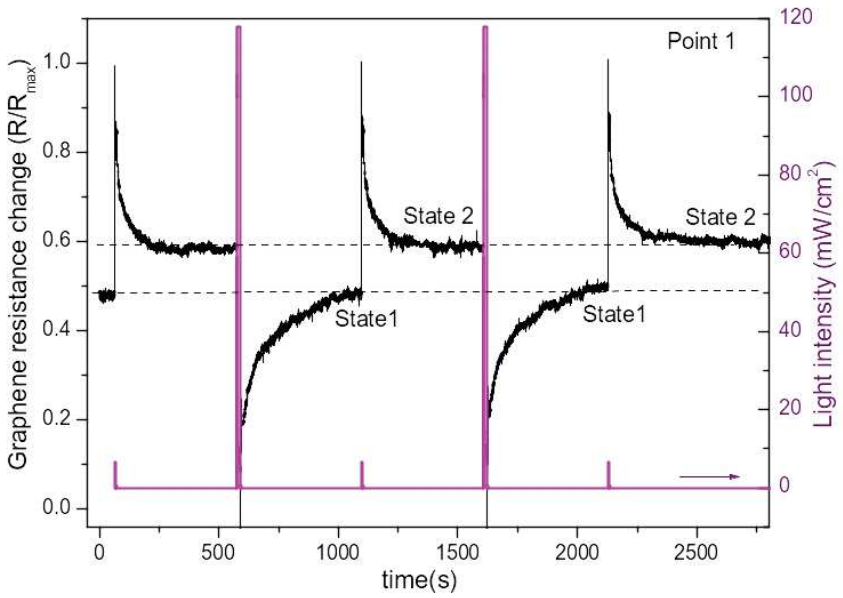

FIGURE 8.11 : Écriture optique et effacement des états résistifs du graphène avec la lumière UV.

Bibliography

[1] A. G. Chynoweth, "Surface space-charge layers in barium titanate," *Phys. Rev.*, vol. 102, pp. 705–714, 1956.

[2] T. Choi, S. Lee, Y. J. Choi, V. Kiryukhin, and S.-W. Cheong, "Switchable ferroelectric diode and photovoltaic effect in $BiFeO_3$," *Science*, vol. 324, 2009.

[3] S. Rühle, "Tabulated values of the shockley-queisser limit for single junction solar cells," *Solar Energy*, vol. 130, pp. 139–147, 2016.

[4] G. Chen, J. Chen, W. Pei, Y. Lu, Q. Zhang, Q. Zhang, and Y. He, "Bismuth ferrite materials for solar cells: Current status and prospects," *Materials Research Bulletin*, vol. 110, pp. 39–49, 2019.

[5] I. Grinberg, D. V. West, M. Torres, G. Gou, D. M. Stein, G. C. L. Wu, E. M. Gallo, A. R. Akbashev, P. K. Davies, J. E. Spanier, and A. M. Rappe, "Perovskite oxides for visible-light-absorbing ferroelectric and photovoltaic materials," *Nature*, pp. 509–512, 2013.

[6] R. Inoue, S. Ishikawa, R. Imura, Y. Kitanaka, T. Oguchi, Y. Noguchi, and M. Miyayama, "Giant photovoltaic effect of ferroelectric domain walls in perovskite single crystals," *Sci. Rep.*, vol. 5, 2015.

[7] P. Lopez-Varo, L. Bertoluzzi, J. Bisquert, M. Alexe, M. Coll, J. Huang, J. A. Jimenez-Tejada, T. Kirchartz, R. Nechache, F. Rosei, and Y. Yuanf, "Physical aspects of ferroelectric semiconductors for photovoltaic solar energy conversion," *Phys. Rep.*, vol. 653, pp. 1–40, 2016.

[8] J. E. Spanier, V. M. Fridkin, A. M. Rappe, A. R. Akbashev, A. Polemi, Y. Qi, Z. Gu, S. M. Young, C. J. Hawley, D. Imbrenda, G. Xiao, A. L. Bennett-Jackson,

and C. L. Johnson, "Power conversion efficiency exceeding the shockley-queisser limit in a ferroelectric insulator," *Nat. Photonics*, vol. 10, pp. 611–616, 2016.

[9] H. Matsuo, Y. Noguchi, and M. Miyayama, "Gap-state engineering of visible-light-active ferroelectrics for photovoltaic applications," *Nat. Commun.*, vol. 8, p. 207, 2017.

[10] A. Pérez-Tomás, A. Mingorance, D. Tanenbaum, and M. Lira-Cantú, *Metal Oxides in Photovoltaics: All-Oxide, Ferroic, and Perovskite Solar Cells*, ch. chapter, pp. 267–356. No. number in Metal Oxide Series, Elsevier.

[11] B. Kundys, M. Viret, D. Colson, and D. O. Kundys, "Light-induced size changes in $BiFeO_3$ crystals," *Nat. Mater.*, vol. 9, pp. 803–805, 2010.

[12] J. Kreisel, M. Alexe, and P. A. Thomas, "A photoferroelectric material is more than the sum of its parts," *Nat. Mater.*, vol. 11, p. 260, 2012.

[13] V. Iurchuk, D. Schick, J. Bran, D. Colson, A. Forget, D. Halley, A. Koc, M. Reinhardt, C. Kwamen, N. Morley, M. Bargheer, M. Viret, R. Gumeniuk, G. Schmerber, B. Doudin, and B. Kundys, "Optical writing of magnetic properties by remanent photostriction," *Phys. Rev. Lett.*, vol. 117, p. 107403, 2016.

[14] S. Manz, M. Matsubara, T. Lottermoser, J. Büchi, A. Iyama, T. Kimura, D. Meier, and M. Fiebig, "Reversible optical switching of antiferromagnetism in $TbMnO_3$," *Nat. Photonics*, vol. 10, pp. 653–656, 2016.

[15] B. Mettout and P. Gisse, "Theory of the photovoltaic and photo-magneto-electric effects in multiferroic materials," *Ferroelectrics*, vol. 506, no. 1, pp. 93–110, 2017.

[16] F. Rubio-Marcos, D. A. Ochoa, A. D. Campo, M. A. García, G. R. Castro, J. F. Fernández, and J. E. García, "Reversible optical control of macroscopic polarization in ferroelectrics," *Nat. Photonics*, vol. 12, pp. 29–32, 2018.

[17] A. Dejneka and M. Tyunina, "Elasto-optic behaviour in epitaxial films of perovskite oxide ferroelectrics," *Adv. Appl. Ceram.*, vol. 117, no. 1, pp. 62–65, 2018.

[18] H. T. Yi, T. Choi, S. G. Choi, Y. S. Oh, and S.-W. Cheong, "Mechanism of the switchable photovoltaic effect in ferroelectric $BiFeO_3$," *Adv. Mater.*, vol. 23, pp. 3403–3407, 2011.

[19] K. T. Butler, J. M. Frost, and A. Walsh, "Ferroelectric materials for solar energy conversion: photoferroics revisited," *Energy Environ. Sci.*, vol. 8, pp. 838–848, 2015.

[20] C. Paillard, X. Bai, M. G. I. C. Infante, G. Geneste, M. Alexe, J. Kreisel, and B. Dkhil, "Photovoltaics with ferroelectrics: current status and beyond," *Adv. Mater.*, vol. 28, pp. 5153–5168, 2016.

[21] R. Nechache, C. Harnagea, S. Li, L. Cardenas, W. Huang, J. Chakrabartty, and F. Rosei, "Bandgap tuning of multiferroic oxide solar cells," *Nat. Photonics*, vol. 9, pp. 61–67, 2015.

[22] M. L. Calzada, R. Jiménez, A. González, J. García-López, D. Leinen, and E. Rodríguez-Castellón, "Interfacial phases and electrical characteristics of ferroelectric strontium bismuth tantalate films on Pt/TiO_2 and $Ti/Pt/Ti$ heterostructure electrodes," *Chem. Mater.*, vol. 17, pp. 1441–1449, 2005.

[23] K. Takagi, S. Kikuchi, J.-F. Li, H. Okamura, R. Watanabe, and A. Kawasaki, "Ferroelectric and photostrictive properties of fine-grained plzt ceramics derived from mechanical alloying," *J. Am. Ceram. Soc.*, vol. 87, pp. 1477–1482, 2004.

[24] L. Pensak, "High-voltage photovoltaic effect," *Phys. Rev.*, vol. 109, pp. 601–601, 1958.

[25] B. Goldstein, "Properties of photovoltaic films of *CdTe*," *Phys. Rev.*, vol. 109, pp. 601–603, 1958.

[26] S. G. Ellis, F. Herman, E. E. Loebner, W. J. Merz, C. W. Struck, and J. G. White, "Photovoltages larger than the band gap in zinc sulfide crystals," *Phys. Rev.*, vol. 109, pp. 1860–1860, 1958.

[27] A. Lempicki, "Anomalous photovoltaic effect in *ZnS* single crystals," *Phys. Rev.*, vol. 113, pp. 1204–1209, 1959.

[28] R. Nitsche and W. J. Merz, "Photoconduction in ternary $V - VI - VII$ compounds," *Journal of Physics and Chemistry of Solids*, vol. 13, no. 1, pp. 154–155, 1960.

[29] R. Kern, "An electro-optical and electromechanical effect in *SbSI*," *Journal of Physics and Chemistry of Solids*, vol. 23, no. 3, pp. 249–253, 1962.

[30] E. Fatuzzo, G. Harbeke, W. J. Merz, R. Nitsche, H. Roetschi, and W. Ruppel, "Ferroelectricity in $SbSI$," *Phys. Rev.*, vol. 127, pp. 2036–2037, 1962.

[31] V. M. Fridkin, A. A. Grekov, A. I. Rodin, E. A. Savchenko, and T. R. Volk, "Photoconductivity in ferroelectrics," *Ferroelectrics*, vol. 6, no. 1, pp. 71–82, 1973.

[32] F. S. Chen, "Optically induced change of refractive indices in $LiNbO_3$ and $LiTaO_3$," *Journal of Applied Physics*, vol. 40, no. 8, pp. 3389–3396, 1969.

[33] P. S. Brody, "Large polarization-dependent photovoltages in ceramic $BaTiO_3$ + 5 wt.% $CaTiO_3$," *Solid State Comm.*, vol. 12, no. 7, pp. 673–676, 1973.

[34] A. M. Glass, D. von der Linde, and T. J. Negran, "High-voltage bulk photovoltaic effect and the photorefractive process in $LiNbO_3$," *Appl. Phys. Lett.*, vol. 25, no. 4, pp. 233–235, 1974.

[35] P. S. Brody and F. Crowne, "Mechanism for high-voltage photovoltaic effect in ceramic ferroelectrics," *Journal Of Electronic Materials*, vol. 4, no. 5, pp. 955–971, 1975.

[36] P. Brody, "High voltage photovoltaic effect in barium titanate and lead titanate-lead zirconate ceramics," *Journal of Solid State Chemistry*, vol. 12, no. 3, pp. 193–200, 1975.

[37] V. M. Fridkin, B. N. Popov, and P. V. Ionov, "Temperature and spectral dependencies of photovoltaic current in ferroelectrics," *Izvestiya Akademii Nauk SSSR Seriya Fizicheskaya*, vol. 41, no. 4, pp. 771–774, 1977.

[38] V. M. Fridkin, "The possible mechanism for the bulk photovoltaic effect and optical damage in ferroelectrics," *Applied physics*, vol. 13, pp. 357–359, 1977.

[39] V. M. Fridkin, B. N. Popov, and P. V. Ionov, "Temperature and spectral dependence of the photovoltaic current in ferroelectrics," *Ferroelectrics*, vol. 18, no. 1, pp. 165–168, 1978.

[40] V. M. Fridkin, B. N. Popov, and K. A. Verkhovskaya, "Effect of anomalous bulk photovoltage in ferroelectrics," *Phys. Stat. Sol. (a)*, vol. 39, no. 1, pp. 193–201, 1977.

[41] V. M. Fridkin, K. A. Verkhovskaya, and B. N. Popov, "Anomalously high photovoltages in ferroelectric semiconductors," *Soviet Physics Semiconductors-USSR*, vol. 11, no. 1, pp. 76–81, 1977.

[42] V. M. Fridkin, B. N. Popov, V. A. Kuznetzov, and M. L. Barsukova, "The photoconductivity and photovoltaic effect in $PbTiO_3$," *Ferroelectrics*, vol. 19, no. 1, pp. 109–110, 1978.

[43] P. S. Brody, "Semiconductor-ferroelectric nonvolatile memory using anomalous high photovoltages in ferroelectric ceramics," *Appl. Phys. Lett.*, vol. 38, no. 3, pp. 153–155, 1981.

[44] S. K. Esayan, V. V. Lemanov, and A. Y. Maksimov, "Photovoltaic effect in ferroelectric $PB_5Ge_3O_{11}$," *Ferroelectrics Letters Section*, vol. 2, no. 2, pp. 93–96, 1984.

[45] T. R. Volk, S. A. Shramchenko, L. A. Shuvalov, and V. M. Fridkin, "X-ray induced metastable photovoltaic centers in ferroelectrics," *Ferroelectrics Letters Section*, vol. 3, no. 1, pp. 23–29, 1984.

[46] Y. Inoue, K. Sato, K. Sato, and H. Miyama, "Photoassisted water decomposition by ferroelectric lead zirconate titanate ceramics with anomalous photovoltaic effects," *J. Phys. Chem.*, vol. 90, pp. 2809–2810, 1986.

[47] N. Kristoffel, "Coherent photovoltaic currents in ferroelectrics," *Ferroelectrics*, vol. 83, no. 1, pp. 55–61, 1988.

[48] Y. Inoue, K. Sato, and K. Sato, "Photovoltaic and photocatalytic behaviour of a ferroelectric semiconductor, lead strontium zirconate titanate, with a polarization axis perpendicular to the surface," *J. Chem. Soc.*, vol. 85, pp. 1765–1774, 1989.

[49] V. K. Malinovsky, "The connection between photovoltaic and photorefractive effects and the local properties of ferroelectrics," *Ferroelectrics*, vol. 117, no. 1, pp. 373–379, 1991.

[50] E. Dubovik, V. Fridkin, and D. Dimos, "The bulk photovoltaic effect in ferroelectric $Pb(Zr, Ti)O - 3$ thin films," *Integrated Ferroelectrics*, vol. 9, no. 4, pp. 285–290, 1995.

[51] S.-Y. Chu, M. L. Mulvihill, Z. Ye, and K. Uchino, "Bulk photovoltaic effect for the linearly polarized light in $Pb(Zn_{1/3}Nb_{2/3})O_3$ single crystals," *Japanese Journal of Applied Physics*, vol. 34, no. 2A, pp. 527–529, 1995.

[52] V. M. Fridkin, A. L. Shlensky, K. A. Verchovskaya, W. D. Bilke, M. Sydow, N. N. Markiewitz, and H. Pietsch, "Pyroelectric and photovoltaic effects in the ferroelectric polymer PVF_2 as fundamentals of electrophotographic process," *Journal Fur Signalaufzeichnungsmaterialien*, vol. 13, no. 6, pp. 421–430, 1985.

[53] K. A. Verkhovskaya, R. Danz, and V. M. Fridkin, "Photoconductivity and bulk photovoltaic effect in the polymer ferroelectric $PVDF$," *Fizika Tverdogo Tela*, vol. 29, no. 7, pp. 2198–2200, 1987.

[54] C. C. Mao, B. Landreth, K. M. Johnson, and G. Moddel, "Photovoltaic optically addressed spatial light modulator," *Ferroelectrics*, vol. 122, no. 1, pp. 101–112, 1991.

[55] A. V. Bune, V. M. Fridkin, K. A. Verkhovskaya, and J. F. Legrand, "Photochromic gratings in the optically sensitized ferroelectric copolymer," *Ferroelectrics*, vol. 127, no. 1, pp. 225–227, 1992.

[56] W. Kraut and R. von Baltz, "Anomalous bulk photovoltaic effect in ferroelectrics: A quadratic response theory," *Phys. Rev. B*, vol. 19, pp. 1548–1554, 1979.

[57] V. I. Belinicher and B. I. Sturman, "The photogalvanic effect in media lacking a center of symmetry," *Soviet Physics Uspekhi*, vol. 23, no. 3, pp. 199–223, 1980.

[58] R. von Baltz and W. Kraut, "Theory of the bulk photovoltaic effect in pure crystals," *Phys. Rev. B*, vol. 23, pp. 5590–5596, 1981.

[59] F. Elguibaly, "Models for the bulk photovoltaic effect in ferroelectric-crystals," *Canadian Journal Of Physics*, vol. 66, no. 8, pp. 649–654, 1988.

[60] A. V. Bune, V. M. Fridkin, K. A. Verkhovskaya, and G. Taylor, "Photoelectric properties of the ferroelectric polymer pvdf," *Polymer Journal*, vol. 22, no. 1, pp. 7–14, 1990.

[61] B. Sturman, "Dynamic holography effects in ferroelectrics induced by spatially oscillating photovoltaic currents," *J. Opt. Soc. Am. B*, vol. 8, no. 6, pp. 1333–1340, 1991.

[62] K. Tonooka, P. Poosanaas, and K. Uchino, "Mechanism of the bulk photovoltaic effect of ferroelectrics," in *Smart Structures and Materials 1998: Smart Materials Technologies* (M. R. Wuttig, ed.), vol. 3324, pp. 224–232, International Society for Optics and Photonics, SPIE, 1998.

[63] V. M. Fridkin, "Bulk photovoltaic effect in noncentrosymmetric crystals," *Crystallography Reports*, vol. 46, pp. 654–658, 2001.

[64] V. M. Fridkin, "Boltzmann principle violation and bulk photovoltaic effect in a crystal without symmetry center," *Ferroelectrics*, vol. 503, no. 1, pp. 15–18, 2016.

[65] K. Nonaka, M. Akiyama, C.-N. Xu, T. Hagio, M. Komatsu, and A. Takase, "Enhanced photovoltaic response in lead lanthanum zirconate-titanate ceramics with a-site deficient composition for photostrictor application," *Japanese J. of Appl. Phys.*, vol. 39, no. Part 1, No. 9A, pp. 5144–5145, 2000.

[66] A. A. Grekov, Z. P. Mastropas, and E. N. Myasnikov, "Structural change of the ferroelectric-semiconductor at excitation of electronic subsystem and photovoltaic effect," *Ferroelectrics*, vol. 255, no. 1, pp. 35–45, 2001.

[67] Y. W. Cho, S. K. Choi, and Y. M. Vysochanskii, "Photovoltaic effect of $Sn_2P_2S_6$ ferroelectric crystal and ceramics," *J. of Materials Research*, vol. 16, no. 11, pp. 3317–3322, 2001.

[68] A. L. Kholkin, V. K. Yarmarkin, B. M. Goltsman, and J. L. Baptista, "Photoelectric evaluation of polarization and internal field in pzt thin films," *Integrated Ferroelectrics*, vol. 35, no. 1-4, pp. 261–268, 2001.

[69] Y. Watanabe and M. Okano, "Photoresponse of zener tunneling junctions of $Pb(Ti, Zr)O_3/SrTiO_3$ at low temperature," *J. of Appl. Phys.*, vol. 94, no. 11, pp. 7187–7192, 2003.

[70] S. R. Kim and S. K. Choi, "Effects of grain size and doping on photovoltaic current in $(Pb_{1-x}La_x)TiO_3$ ferroelectric ceramics," *Ferroelectrics Letters Section*, vol. 31, no. 3-4, pp. 63–72, 2004.

[71] K. Yao, B. K. Gan, M. Chen, and S. Shannigrahi, "Large photo-induced voltage in a ferroelectric thin film with in-plane polarization," *Appl. Phys. Lett.*, vol. 87, no. 21, p. 212906, 2005.

[72] B. K. Gan, K. Yao, S. C. Lai, Y. F. Chen, and P. C. Goh, "An ultraviolet (uv) detector using a ferroelectric thin film with in-plane polarization," *IEEE Electron Device Letters*, vol. 29, no. 11, pp. 1215–1217, 2008.

[73] L. Pintilie, I. Vrejoiu, G. Le Rhun, and M. Alexe, "Short-circuit photocurrent in epitaxial lead zirconate-titanate thin films," *J. of Appl. Phys.*, vol. 101, no. 6, p. 064109, 2007.

[74] L. A. Delimova, D. V. Mashovets, and V. S. Yuferev, "Photovoltaic effect based on polarization charge in polycrystalline $Pb(ZrTi)O_3$ film," *Integrated Ferroelectrics*, vol. 102, no. 1, pp. 37–43, 2008.

[75] M. Ichiki, Y. Morikawa, Y. Mabune, T. Nakada, K. Nonaka, and R. Maeda, "Preparation of ferroelectric ceramics in a film structure and their photovoltaic properties," *Microsystem Technologies*, vol. 12, pp. 143–148, 2005.

[76] M. Qin, K. Yao, Y. C. Liang, and S. Shannigrahi, "Thickness effects on photoinduced current in ferroelectric $(Pb_{0.97}La_{0.03})(Zr_{0.52}Ti_{0.48})O_3$ thin films," *J. of Appl. Phys.*, vol. 101, no. 1, p. 014104, 2007.

[77] M. Qin, K. Yao, and Y. C. Liang, "High efficient photovoltaics in nanoscaled ferroelectric thin films," *Appl. Phys. Lett.*, vol. 93, no. 12, p. 122904, 2008.

[78] M. Qin, K. Yao, and Y. C. Liang, "Photovoltaic characteristics in polycrystalline and epitaxial $(Pb_{0.97}La_{0.03})(Zr_{0.52}Ti_{0.48})O_3$ ferroelectric thin films sandwiched between different top and bottom electrodes," *J. of Appl. Phys.*, vol. 105, no. 6, p. 061624, 2009.

[79] M. Qin, K. Yao, Y. C. Liang, and B. K. Gan, "Stability and magnitude of photovoltage in ferroelectric $(Pb_{0.97}La_{0.03})(Zr_{0.52}Ti_{0.48})O_3$ thin films in multicycle uv light illumination," *Integrated Ferroelectrics*, vol. 95, no. 1, pp. 105–116, 2007.

[80] A. A. Bogomolov, A. V. Solnyshkin, D. A. Kiselev, I. P. Raevskii, V. Y. Shonov, and D. N. Sandzhiev, "Temperature behavior of the photovoltaic and pyroelectric responses of $Sn_2P_2S_6$ semiconductor ferroelectric films," *J. of Surface Investigation-X-ray Synchrotron and Neutron Techniques*, vol. 2, no. 3, pp. 496–501, 2008.

[81] S. Y. Yang, L. W. Martin, S. J. Byrnes, T. E. Conry, S. R. Basu, D. Paran, L. Reichertz, J. Ihlefeld, C. Adamo, A. Melville, Y.-H. Chu, C.-H. Yang, J. L. Musfeldt, D. G. Schlom, J. W. Ager, and R. Ramesh, "Photovoltaic effects in $BiFeO_3$," *Appl. Phys. Lett.*, vol. 95, no. 6, p. 062909, 2009.

[82] S. Y. Yang, J. Seidel, S. J. Byrnes, P. Shafer, C.-H. Yang, M. D. Rossell, P. Yu, Y.-H. Chu, J. F. Scott, J. W. Ager, L. W. Martin, and R. Ramesh, "Above-bandgap voltages from ferroelectric photovoltaic devices," *Nature Nanotechnology*, vol. 5, pp. 143–147, 2010.

[83] W. Ji, K. Yao, and Y. C. Liang, "Bulk photovoltaic effect at visible wavelength in epitaxial ferroelectric $BiFeO_3$ thin films," *Advanced Materials*, vol. 22, no. 15, pp. 1763–1766, 2010.

[84] M.-M. Yang, Z.-D. Luo, D. J. Kim, and M. Alexe, "Bulk photovoltaic effect in monodomain $BiFeO_3$ thin films," *Appl. Phys. Lett.*, vol. 110, no. 18, 2017.

[85] Y. Li, C. Adamo, C. E. Rowland, R. D. Schaller, D. G. Schlom, and D. A. Walko, "Nanoscale excitonic photovoltaic mechanism in ferroelectric $BiFeO_3$ thin films," *APL Materials*, vol. 6, no. 8, p. 084905, 2018.

[86] V. S. Puli, D. K. Pradhan, R. K. Katiyar, I. Coondoo, N. Panwar, P. Misra, D. B. Chrisey, J. F. Scott, and R. S. Katiyar, "Photovoltaic effect in transition metal modified polycrystalline $BiFeO_3$ thin films," *Journal of Physics D: Applied Physics*, vol. 47, no. 7, p. 075502, 2014.

[87] L. Fei, Y. Hu, X. Li, R. Song, L. Sun, H. Huang, H. Gu, H. L. W. Chan, and Y. Wang, "Electrospun bismuth ferrite nanofibers for potential applications in ferroelectric photovoltaic devices," *ACS Appl. Mater. Interfaces*, vol. 7, pp. 3665–3670, 2015.

[88] J. X. Zhang, H. W. Zheng, Y. G. Zhang, G. L. Yuan, W. X. Gao, X. Y. Liu, G. S. Yin, Y. Z. Gu, and W. F. Zhang, "Photovoltaic effect of a bilayer film with $Bi_4Ti_3O_{12}/BiFeO_3$ heterostructure," *Materials Letters*, vol. 156, pp. 98–100, 2015.

[89] W. Zhang, M.-M. Yang, X. Liang, H.-W. Zheng, Y. Wang, W.-X. Gao, G.-L. Yuan, W.-F. Zhang, X.-G. Li, H.-S. Luo, and R.-K. Zheng, "Piezostrain-enhanced

photovoltaic effects in $BiFeO_3/La_{0.7}Sr_{0.3}MnO_3/PMN-PT$ heterostructures," *Nano Energy*, vol. 18, pp. 315–324, 2015.

[90] J. P. Chakrabartty, R. Nechache, C. Harnagea, and F. Rosei, "Photovoltaic effect in multiphase $Bi-Mn-O$ thin films," *Opt. Express*, vol. 22, pp. A80–A89, 2014.

[91] L. Chen, Q. Lin, J. Hart, S. Li, and D. Wang, "Enhanced photovoltaic effect in fe-doped $(Bi, Na)TiO_3 - BaTiO_3$ ferroelectric ceramics," *International Journal of Applied Ceramic Technology*, vol. 13, no. 5, pp. 896–903, 2016.

[92] K. Wang, H. W. Zheng, X. J. Li, G. L. Yuan, W. X. Gao, L. Wei, X. A. Zhang, and W. F. Zhang, "Effect of top electrodes and light sources on photovoltaic properties of polycrystalline $Bi_4Ti_3O_{12}$ film," *Materials Letters*, vol. 179, pp. 182–185, 2016.

[93] J. P. B. Silva, K. Kamakshi, K. C. Sekhar, X. R. Nóvoa, E. C. Queirós, J. Agostinho Moreira, A. Almeida, M. Pereira, P. B. Tavares, and M. J. M. Gomes, "Light controlled resistive switching and photovoltaic effects in ferroelectric $0.5Ba(Zr_{0.2}Ti_{0.8})O_3 - 0.5(Ba_{0.7}Ca_{0.3})TiO_3$ thin films," *Journal of the European Ceramic Society*, vol. 37, no. 2, pp. 583–591, 2017.

[94] H. Xiao, W. Dong, Y. Guo, Y. Wang, H. Zhong, Q. Li, and M.-M. Yang, "Design for highly piezoelectric and visible/near-infrared photoresponsive perovskite oxides," *Adv. Mater.*, vol. 31, no. 4, p. 1805802, 2019.

[95] Y. Li, X. Cui, N. Sun, J. Du, X. Li, G. Jia, and X. Hao, "Region-dependent and stable ferroelectric photovoltaic effect driven by novel in-plane self-polarization in narrow-bandgap $Bi_2FeMo_{0.7}Ni_{0.3}O_6$ thin film," *Adv. Opt. Mater.*, vol. 7, no. 3, p. 1801105, 2019.

[96] A. Bihari Swain, D. Murali, B. R. K. Nanda, and P. Murugavel, "Large bulk photovoltaic response by symmetry-breaking structural transformation in ferroelectric $[Ba(zr_{0.2}ti_{0.8})o_3]0.5[(ba_{0.7}ca_{0.3})tio_3]0.5$," *Phys. Rev. Applied*, vol. 11, p. 044007, 2019.

[97] X. He, C. Chen, C. Li, H. Zeng, and Z. Yi, "Ferroelectric, photoelectric, and photovoltaic performance of silver niobate ceramics," *Advanced Functional Materials*, vol. 29, no. 28, p. 1900918, 2019.

[98] D. S. Knoche, Y. Yun, N. Ramakrishnegowda, L. Mühlenbein, X. Li, and A. Bhatnagar, "Domain and switching control of the bulk photovoltaic effect in epitaxial $BiFeO_3$ thin films," *Scientific Reports*, vol. 9, p. 13979, 2019.

[99] L.-F. Zhu, W.-Y. Pan, Y. Xie, B.-P. Zhang, Y. Yin, and G.-L. Zhao, "Effect of regulation of defect ion on ferroelectric photovoltaic characteristics of $BiFeO_3 - BaTiO_3$ based perovskite materials," *Acta Physica Sinica*, vol. 68, 2019.

[100] M. A. Jalaja and S. Dutta, "Optically controlled polarization, photovoltaic and switchable diode behavior in multifunctional $KBiFe_2O_5$ composite film," *Ceramics International*, vol. 45, pp. 22553–22557, 2019.

[101] Y. Watanabe and M. Okano, "Photodiode properties of epitaxial $Pb(Ti, Zr)O_3/SrTiO_3$ ferroelectric heterostructures," *Appl. Phys. Lett.*, vol. 78, no. 13, pp. 1906–1908, 2001.

[102] D. Cao, C. Wang, F. Zheng, W. Dong, L. Fang, and M. Shen, "High-efficiency ferroelectric-film solar cells with an n-type Cu_2O cathode buffer layer," *Nano Lett.*, vol. 12, no. 6, pp. 2803–2809, 2012.

[103] P. Zhang, D. Cao, C. Wang, M. Shen, X. Su, L. Fang, W. Dong, and F. Zheng, "Enhanced photocurrent in $Pb(Zr_{0.2}Ti_{0.8})O_3$ ferroelectric film by artificially introducing asymmetrical interface schottky barriers," *Materials Chemistry and Physics*, vol. 135, no. 2, pp. 304–308, 2012.

[104] F. Zheng, Y. Xin, W. Huang, J. Zhang, X. Wang, M. Shen, W. Dong, L. Fang, Y. Bai, X. Shen, and J. Hao, "Above 1% efficiency of a ferroelectric solar cell based on the $Pb(Zr, Ti)O_3$ film," *J. Mater. Chem. A*, vol. 2, pp. 1363–1368, 2014.

[105] D.-F. Pan, G.-F. Bi, G.-Y. Chen, H. Zhang, J.-M. Liu, G.-H. Wang, and J.-G. Wan, "Polarization-dependent interfacial coupling modulation of ferroelectric photovoltaic effect in pzt-zno heterostructures," *Scientific Reports*, vol. 6, 2016.

[106] Y. Zhou, J. Zhu, X. Liu, and Z. Wu, "Photovoltaic effect of ferroelectric $Pb(Zr_{0.52}, Ti_{0.48})O_3$ deposited on $SrTiO_3$ buffered n-gaas by laser molecular beam epitaxy," *Functional Materials Letters*, vol. 10, no. 04, p. 1750036, 2017.

[107] Y. Song, L. Li, Y. Chen, F. Li, W. Qu, H. Wu, A. S. Yerramilli, T. L. Alford, and H. Zheng, "Fabrication of pzt/cuo composite films and their photovoltaic

properties," *Journal of Sol-Gel Science and Technology*, vol. 87, no. 2, pp. 285–291, 2018.

[108] Y. Chen, J. Chen, S. Yang, Y. Li, X. Gao, M. Zeng, Z. Fan, X. Gao, X. Lu, and J. M. Liu, "A bi-functional ferroelectric $Pb(Zr_{0.52}Ti_{0.48})O_3$ films: Energy storage properties and ferroelectric photovoltaic effects," *Materials Research Bulletin*, vol. 107, pp. 456–461, 2018.

[109] V. N. Harshan and S. Kotru, "Influence of work-function of top electrodes on the photovoltaic characteristics of $Pb_{0.95}La_{0.05}Zr_{0.54}Ti_{0.46}O_3$ thin film capacitors," *Appl. Phys. Lett.*, vol. 100, no. 17, p. 173901, 2012.

[110] M. Ichiki, H. Furue, T. Kobayashi, R. Maeda, Y. Morikawa, T. Nakada, and K. Nonaka, "Photovoltaic properties of $(Pb, La)(Zr, Ti)O_3$ films with different crystallographic orientations," *Appl. Phys. Lett.*, vol. 87, no. 22, p. 222903, 2005.

[111] B. Chen, M. Li, Y. Liu, Z. Zuo, F. Zhuge, Q.-F. Zhan, and R.-W. Li, "Effect of top electrodes on photovoltaic properties of polycrystalline $BiFeO_3$ based thin film capacitors," *Nanotechnology*, vol. 22, no. 19, 2011.

[112] J. Seidel, D. Fu, S. Y. Yang, E. Alarcón-Lladó, J. Wu, R. Ramesh, and J. W. r. Ager, "Efficient photovoltaic current generation at ferroelectric domain walls," *Phys. Rev. Lett.*, vol. 107, no. 12, p. 126805, 2011.

[113] G. Gopal Khan, R. Das, N. Mukherjee, and K. Mandal, "Effect of metal doping on highly efficient photovoltaics and switchable photovoltage in bismuth ferrite nanotubes," *physica status solidi (RRL) - Rapid Research Letters*, vol. 6, no. 7, pp. 312–314, 2012.

[114] T. L. Qu, Y. G. Zhao, D. Xie, J. P. Shi, Q. P. Chen, and T. L. Ren, "Resistance switching and white-light photovoltaic effects in $BiFeO_3/Nb$-$SrTiO_3$ heterojunctions," *Appl. Phys. Lett.*, vol. 98, no. 17, p. 173507, 2011.

[115] Y. Zang, D. Xie, X. Wu, Y. Chen, Y. Lin, M. Li, H. Tian, X. Li, Z. Li, H. Zhu, T. Ren, and D. Plant, "Enhanced photovoltaic properties in graphene/polycrystalline $BiFeO_3$/pt heterojunction structure," *Applied Physics Letters*, vol. 99, no. 13, p. 132904, 2011.

[116] W. Dong, Y. Guo, B. Guo, H. Liu, H. Li, and H. Liu, "Enhanced photovoltaic properties in polycrystalline $BiFeO_3$ thin films with rhombohedral perovskite structure deposited on fluorine doped tin oxide substrates," *Materials Letters*, vol. 88, pp. 140–142, 2012.

[117] W. Dong, Y. Guo, B. Guo, H. Li, H. Liu, and T. W. Joel, "Enhanced photovoltaic effect in $BiVO_4$ semiconductor by incorporation with an ultrathin $BiFeO_3$ ferroelectric layer," *ACS Applied Materials & Interfaces*, vol. 5, no. 15, pp. 6925–6929, 2013.

[118] C. S. Tu, C.-M. Hung, Z.-R. Xu, V. H. Schmidt, Y. Ting, R. R. Chien, Y.-T. Peng, and J. Anthoninappen, "Calcium-doping effects on photovoltaic response and structure in multiferroic $BiFeO3$ ceramics," *Journal of Applied Physics*, vol. 114, no. 12, p. 124105, 2013.

[119] Z. Lin, W. Cai, W. Jiang, C. Fu, C. Li, and Y. Song, "Effects of annealing temperature on the microstructure, optical, ferroelectric and photovoltaic properties of $BiFeO_3$ thin films prepared by sol-gel method," *Ceramics International*, vol. 39, no. 8, pp. 8729–8736, 2013.

[120] Z. Fan, K. Yao, and J. Wang, "Photovoltaic effect in an indium-tin-oxide/$ZnO/BiFeO_3/Pt$ heterostructure," *Appl. Phys. Lett.*, vol. 105, no. 16, p. 162903, 2014.

[121] C.-M. Hung, C. S. Tu, Z.-R. Xu, L.-Y. Chang, V. H. Schmidt, R. R. Chien, and W. C. Chang, "Effect of diamagnetic barium substitution on magnetic and photovoltaic properties in multiferroic $BiFeO_3$," *Journal of Applied Physics*, vol. 115, no. 17, p. 17D901, 2014.

[122] C.-S. Tu, Z.-R. Xu, V. H. Schmidt, T.-S. Chan, R. R. Chien, and H. Son, "A-site strontium doping effects on structure, magnetic, and photovoltaic properties of $(Bi_{1-x}Sr_x)FeO_{3-\delta}$ multiferroic ceramics," *Ceramics International*, vol. 41, no. 7, pp. 8417–8424, 2015.

[123] S. Sharma, M. Tomar, A. Kumar, N. K. Puri, and V. Gupta, "Enhanced ferroelectric photovoltaic response of bifeo3/batio3 multilayered structure," *Journal of Applied Physics*, vol. 118, no. 7, p. 074103, 2015.

[124] J. Chakrabartty, R. Nechache, C. Harnagea, S. Li, and F. Rosei, "Enhanced photovoltaic properties in bilayer $BiFeO_3/Bi-Mn-O$ thin films," *Nanotechnology*, vol. 27, no. 21, 2016.

[125] C.-S. Tu, C.-S. Chen, P.-Y. Chen, H.-H. Wei, V. H. Schmidt, C.-Y. Lin, J. Anthoniappen, and J.-M. Lee, "Enhanced photovoltaic effects in a-site samarium doped $BiFeO_3$ ceramics: The roles of domain structure and electronic state," *Journal of the European Ceramic Society*, vol. 36, no. 5, pp. 1149–1157, 2016.

[126] R. Gao, C. Fu, W. Cai, G. Chen, X. Deng, and X. Cao, "Thickness dependence of photovoltaic effect in $BiFeO_3$ thin films based on asymmetric structures," *Journal of Electronic Materials*, vol. 46, no. 4, pp. 2373–2378, 2017.

[127] L. Wang, H. Ma, L. Chang, C. Ma, G. Yuan, J. Wang, and T. Wu, "Ferroelectric $BiFeO_3$ as an oxide dye in highly tunable mesoporous all-oxide photovoltaic heterojunctions," *Small*, vol. 13, no. 1, p. 1602355, 2017.

[128] A. M. Afzal, Y. Javed, S. Hussain, A. Ali, M. Z. Yaqoob, and S. Mumtaz, "Enhancement in photovoltaic properties of bismuth ferrite/zinc oxide heterostructure solar cell device with graphene/indium tin oxide hybrid electrodes," *Ceramics International*, vol. 46, no. 7, pp. 9161–9169, 2020.

[129] H. Lee, H.-S. Kim, O. Y. Gong, J. Y. Kim, J. H. Kim, J. S. Choi, H. S. Jung, J.-Y. Park, D. H. Kim, Y.-S. Seo, and T. Choi, "Enhanced ferroelectric photovoltaic effect in semiconducting single-wall carbon nanotube/$BiFeO_3$ heterostructures enabled by wide-range light absorption and efficient charge separation," *Journal of Materials Chemistry A*, vol. 8, no. 20, pp. 10377–10385, 2020.

[130] O. Ceballos-Sanchez, A. Sanchez-Martinez, F. J. Flores-Ruiz, A. M. Huerta-Flores, L. M. Torres-Martinez, R. Ruelas, and M. Garcia-Guaderrama, "Study of $BiFeO_3$ thin film obtained by a simple chemical method for the heterojunction-type solar cell design," *Journal of Alloys and Compounds*, vol. 832, 2020.

[131] Y. Zhang, H. Sun, C. Yang, H. Su, and X. Liu, "Modulating photovoltaic conversion efficiency of $BiFeO_3$-based ferroelectric films by the introduction of electron transport layers," *ACS Applied Energy Materials*, vol. 2, no. 8, pp. 5540–5546, 2019.

[132] W. Jiang, W. Cai, Z. Lin, and C. Fu, "Effects of nd-doping on optical and photovoltaic properties of barium titanate thin films prepared by sol-gel method," *Materials Research Bulletin*, vol. 48, no. 9, pp. 3092–3097, 2013.

[133] R. Nechache, W. Huang, S. Li, and F. Rosei, "Photovoltaic properties of Bi_2FeCrO_6 films epitaxially grown on (100)-oriented silicon substrates," *Nanoscale*, vol. 8, pp. 3237–3243, 2016.

[134] W. Huang, C. Harnagea, D. Benetti, M. Chaker, F. Rosei, and R. Nechache, "Multiferroic bi2fecro6 based p-i-n heterojunction photovoltaic devices," *Journal of Materials Chemistry A*, vol. 5, no. 21, pp. 10355–10364, 2017.

[135] J. P. Chakrabartty, R. Nechache, C. Harnagea, and F. Rosei, "Photovoltaic effect in multiphase bi-mn-o thin films," *Opt. Express*, vol. 22, no. S1, pp. A80–A89, 2014.

[136] J. Chakrabartty, C. Harnagea, M. Celikin, F. Rosei, and R. Nechache, "Improved photovoltaic performance from inorganic perovskite oxide thin films with mixed crystal phases," *Nature Photonics*, vol. 12, no. 5, pp. 271+, 2018.

[137] W. Seok Woo, S. Sik Won, C. Won Ahn, S. A. Chae, A. Ullah, and I. Won Kim, "Photovoltaic effect of lead-free $(Na_{0.82}K_{0.18})_{0.5}Bi_{4.5}Ti_4O_{15}$ ferroelectric thin film using pt and indium tin oxide top electrodes," *Journal of Applied Physics*, vol. 115, no. 3, p. 034107, 2014.

[138] H. Han, S. Song, J. H. Lee, K. J. Kim, G.-W. Kim, T. Park, and H. M. Jang, "Switchable photovoltaic effects in hexagonal manganite thin films having narrow band gaps," *Chemistry of Materials*, vol. 27, no. 21, pp. 7425–7432, 2015.

[139] R. Gao, W. Cai, G. Chen, X. Deng, X. Cao, and C. Fu, "Enhanced ferroelectric photovoltaic effect based on converging depolarization field," *Materials Research Bulletin*, vol. 84, pp. 93–98, 2016.

[140] H. Han, D. Kim, K. Chu, J. Park, S. Y. Nam, S. Heo, C.-H. Yang, and H. M. Jang, "Enhanced switchable ferroelectric photovoltaic effects in hexagonal ferrite thin films via strain engineering," *ACS Applied Materials & Interfaces*, vol. 10, no. 2, pp. 1846–1853, 2018.

[141] C. Li, K. Jiang, J. Jiang, Z. Hu, A. Liu, G. Hu, W. Shi, and J. Chu, "Enhanced photovoltaic response of lead-free ferroelectric solar cells based on $(K, Bi)(Nb, Yb)O_3$ films," *Physical Chemistry Chemical Physics*, vol. 22, no. 6, pp. 3691–3701, 2020.

[142] M. A. Jalaja and S. Dutta, "Multifunctional $KBiFe_2O_5$ thick film: advances in functional properties," *Journal of Materials Science-Materials in Electronics*, vol. 31, no. 13, pp. 10234–10240, 2020.

[143] J. Park, S. S. Won, C. W. Ahn, and I. W. Kim, "Ferroelectric photocurrent effect in polycrystalline lead-free $(K_{0.5}Na_{0.5})(Mn_{0.005}Nb_{0.995})O_3$ thin film," *J. of the Am. Ceram. Soc.*, vol. 96, no. 1, pp. 146–150, 2013.

[144] L. Pintilie, C. Dragoi, and I. Pintilie, "Interface controlled photovoltaic effect in epitaxial $Pb(Zr, Ti)O_3$ films with tetragonal structure," *J. of Appl. Phys.*, vol. 110, no. 4, p. 044105, 2011.

[145] A. S. Makhort, F. Chevrier, D. Kundys, B. Doudin, and B. Kundys, "Photovoltaic effect and photopolarization in $Pb\left[(Mg_{1/3}Nb_{2/3})_{0.68}Ti_{0.32}\right]O_3$ crystal," *Phys. Rev. Mater.*, vol. 2, p. 012401, 2018.

[146] A. Quattropani, A. S. Makhort, M. V. Rastei, G. Versini, G. Schmerber, S. Barre, A. Dinia, A. Slaoui, J.-L. Rehspringer, T. Fix, S. Colis, and B. Kundys, "Tuning photovoltaic response in Bi_2FeCrO_6 films by ferroelectric poling," *Nanoscale*, vol. 10, pp. 13761–13766, 2018.

[147] S. Young, F. Zheng, and A. Rappe, "First-principles calculation of the bulk photovoltaic effect in bismuth ferrite," *Phys. Rev. Lett.*, vol. 109, p. 236601, 2012.

[148] A. Bhatnagar, A. Roy Chaudhuri, Y. Heon Kim, D. Hesse, and M. Alexe, "Role of domain walls in the abnormal photovoltaic effect in $BiFeO_3$," *Nature Communications*, vol. 4, p. 2835, 2013.

[149] C. Blouzon, J.-Y. Chauleau, A. Mougin, S. Fusil, and M. Viret, "Photovoltaic response around a unique 180° ferroelectric domain wall in single-crystalline $BiFeo_3$," *Phys. Rev. B*, vol. 94, p. 094107, 2016.

[150] R. Williams and R. H. Bube, "Photoemission in the photovoltaic effect in cadmium sulfide crystals," *J. of Appl. Phys.*, vol. 31, no. 6, pp. 968–978, 1960.

[151] C.-M. Hung, C.-S. Tu, W. D. Yen, L. S. Jou, M.-D. Jiang, and V. H. Schmidt, "Photovoltaic phenomena in $BiFeO_3$ multiferroic ceramics," *J. of Appl. Phys.*, vol. 111, no. 7, p. 07D912, 2012.

[152] Y. Guo, H. Luo, K. Chen, H. Xu, X. Zhang, and Z. Yin, "Effect of composition and poling field on the properties and ferroelectric phase-stability of $Pb(Mg_{1/3}Nb_{2/3})O_3 - PbTiO_3$ crystals," *J. of Appl. Phys.*, vol. 92, no. 10, pp. 6134–6138, 2002.

[153] C.-S. Tu, F.-T. Wang, R. R. Chien, V. H. Schmidt, C.-M. Hung, and C.-T. Tseng, "Dielectric and photovoltaic phenomena in tungsten doped $Pb\left[(Mg_{1/3}Nb_{2/3})_{1-x}Ti_x\right]O_3$ crystal," *Appl. Phys. Lett.*, vol. 88, no. 3, p. 032902, 2006.

[154] M. Mitra, J. Drayton, M. L. C. Cooray, V. G. Karpov, and D. Shvydka, "Piezo-photovoltaic coupling in *CdS*-based thin-film photovoltaics," *Journal of Applied Physics*, vol. 102, no. 3, p. 034505, 2007.

[155] F. Bai, N. Wang, J. Li, D. Viehland, P. M. Gehring, G. Xu, and G. Shirane, "X-ray and neutron diffraction investigations of the structural phase transformation sequence under electric field in $0.7Pb(Mg_{1/3}Nb_{2/3}) - 0.3PbTiO_3$ crystal," *Journal of Applied Physics*, vol. 96, no. 3, pp. 1620–1627, 2004.

[156] Y. Guo, H. Luo, D. Ling, H. Xu, T. He, and Z. Yin, "The phase transition sequence and the location of the morphotropic phase boundary region in $(1-x)[Pb(Mg_{1/3}Nb_{2/3})O_3] - xPbTiO_3$ single crystal," *J. Phys. Condens. Matter*, vol. 15, no. 2, pp. L77–L82, 2003.

[157] Crystal GmbH, "https://www.crystal-gmbh.com/."

[158] C. B. Sawyer and C. H. Tower, "Rochelle salt as a dielectric," *Phys. Rev.*, vol. 35, pp. 269–273, 1930.

[159] H. M. Barkla and D. M. Finlayson, "The properties of KH_2P0_4 below the curie point," *Phil. Mag.*, vol. 44, pp. 109–130, 1953.

[160] H. H. Wieder, "Retarded polarization phenomena in $BaTiO_3$ crystals," *Journal of Applied Physics*, vol. 27, no. 4, pp. 413–416, 1956.

[161] J. Mastner, "A quasistatic hysteresis loop tracer," *Journal of Physics E: Scientific Instruments*, vol. 1, no. 12, pp. 1249–1250, 1968.

[162] Q. Liu and J. Huber, "Creep in ferroelectrics due to unipolar electrical loading," *Journal of the European Ceramic Society*, vol. 26, no. 13, pp. 2799–2806, 2006.

[163] G. Viola, K. Boon Chong, F. Guiu, and M. John Reece, "Role of internal field and exhaustion in ferroelectric switching," *Journal of Applied Physics*, vol. 115, no. 3, p. 034106, 2014.

[164] Y. J. Shin, B. C. Jeon, S. M. Yang, I. Hwang, M. R. Cho, D. Sando, S. R. Lee, J.-G. Yoon, and T. W. Noh, "Suppression of creep-regime dynamics in epitaxial ferroelectric $BiFeO_3$ films," *Scientific Reports*, vol. 5, p. 10485, 2015.

[165] X. Xia, Y. Wang, Z. Zhong, and G. J. Weng, "Theory of electric creep and electromechanical coupling with domain evolution for non-poled and fully poled ferroelectric ceramics," *Proc. R. Soc.*, vol. 472, 2016.

[166] D. Zhao, T. Lenz, G. H. Gelinck, P. Groen, D. Damjanovic, D. M. de Leeuw, and I. Katsouras, "Depolarization of multidomain ferroelectric materials," *Nature Communications*, vol. 10, p. 2547, 2019.

[167] D. J. Jung, M. Dawber, J. F. Scott, L. J. Sinnamon, and J. M. Gregg, "Switching dynamics in ferroelectric thin films: An experimental survey," *Integrated Ferroelectrics*, vol. 48, no. 1, pp. 59–68, 2002.

[168] R. von Baltz and W. Kraut, "Theory of the bulk photovoltaic effect in pure crystals," *Phys. Rev. B*, vol. 23, pp. 5590–5596, 1981.

[169] B. Jaffe, W. R. Cook, and H. Jaffe, *Piezoelectric Ceramics*. London and New York: Academic Press, 1 ed.

[170] D. Lee, S. M. Yang, T. H. Kim, B. C. Jeon, Y. S. Kim, J.-G. Yoon, H. N. Lee, S. H. Baek, C. B. Eom, and T. W. Noh, "Multilevel data storage memory using deterministic polarization control," *Adv. Mater.*, vol. 24, no. 3, pp. 402–406, 2012.

[171] D. Z. Sun, H. S. Luo, M. Y. Zhao, H. Q. Xu, S. W. Lin, and Z. W. Yin, "Investigation on inhomogeneity in $PMN-PT$ material by nonlinear pyroelectric effect," *Ferroelectrics Letters Section*, vol. 27, no. 3-4, pp. 59–63, 2000.

[172] P. Kumar, S. Sharma, O. Thakur, C. Prakash, and T. C. Goel, "Dielectric, piezoelectric and pyroelectric properties of $PMN-PT$ (68:32) system," *Ceramics International*, vol. 30, no. 4, pp. 585–589, 2004.

[173] Y. Tang and H. Luo, "Investigation of the electrical properties of $(1-x)Pb(Mg_{1/3}Nb_{2/3})O_3 - xPbTiO_3$ single crystals with special reference to pyroelectric detection," *J. of Physics D: Applied Physics*, vol. 42, p. 075406, 2009.

[174] P. Yu, Y. Tang, and H. Luo, "Fabrication, property and application of novel pyroelectric single crystals-$PMN-PT$," *J. of Electroceramics*, vol. 24, pp. 1–4, 2010.

[175] R. Kandilian, A. Navid, and L. Pilon, "The pyroelectric energy harvesting capabilities of $PMN-PT$ near the morphotropic phase boundary," *Smart Materials and Structures*, vol. 20, no. 5, p. 055020, 2011.

[176] C. S. Lynch, W. Yang, L. Collier, Z. Suo, and R. M. McMeeking, "Electric field induced cracking in ferroelectric ceramics," *Ferroelectrics*, vol. 166, no. 1, pp. 11–30, 1995.

[177] J. Nuffer, D. C. Lupascu, and J. Rödel, "Damage evolution in ferroelectric *PZT* induced by bipolar electric cycling," *Acta Materialia*, vol. 48, no. 14, pp. 3783–3794, 2000.

[178] S. Ozgul, M. andTrolier-Mckinstry and C. A. Randall, "Fatigue induced effects on bipolar strain loops in *PZN-PT* piezoelectric single crystals," *Journal of Electroceramics*, vol. 20, pp. 133–138, 2008.

[179] J.-H. Gao, D. Xue, L. Zhang, Y. Wang, H. Bao, C. Zhou, W. Liu, W. Chen, and X. Ren, "Aging-induced domain memory in acceptor-doped perovskite ferroelectrics associated with ferroelectric-ferroelectric transition cycle," *Europhysics Lett.*, vol. 96, no. 3, p. 37001, 2011.

[180] Y. A. Genenko, J. Glaum, M. J. Hoffmann, and K. Albe, "Mechanisms of aging and fatigue in ferroelectrics," *Mat. Sc. and Eng.: B*, vol. 192, pp. 52–82, 2015.

[181] J. Lv, X. Lou, and J. Wu, "Defect dipole-induced poling characteristics and ferroelectricity of quenched bismuth ferrite-based ceramics," *J. Mater. Chem. C*, vol. 4, pp. 6140–6151, 2016.

[182] H. Borkar, M. Tomar, V. Gupta, R. S. Katiyar, J. F. Scott, and A. Kumar, "Optically controlled polarization in highly oriented ferroelectric thin films," *Mat. Res. Express*, vol. 4, no. 8, p. 086402, 2017.

[183] H. Borkar, V. Rao, M. Tomar, V. Gupta, J. F. Scott, and A. Kumar, "Experimental evidence of electronic polarization in a family of photo-ferroelectrics," *RSC Adv.*, vol. 7, pp. 12842–12855, 2017.

[184] K. Y. Chan, W. S. Tsang, C. L. Mak, K. H. Wong, and P. M. Hui, "Effects of composition of $PbTiO_3$ on optical properties of $(1-x)PbMg_{1/3}Nb_{2/3}O_3 - xPbTiO_3$ thin films," *Phys. Rev. B*, vol. 69, p. 144111, 2004.

[185] R. E. Pasynkov, "On some problems of the phenomenological theory of ferroelectric-semiconductors," *Ferroelectrics*, vol. 6, no. 1, pp. 19–27, 1973.

[186] D. P. Rai, S. Kaur, and S. Srivastava, "Band gap modulation of mono and bi-layer hexagonal *ZnS* under transverse electric field and bi-axial strain: A first principles study," *Physica B: Condensed Matter*, vol. 531, pp. 90–94, 2018.

[187] Z. Bai, W. Geng, Y. Zhang, S. Xu, H. Guo, and A. Jiang, "The abnormal photovoltaic effect in $BiFeO_3$ thin films modulated by bipolar domain orientations and oxygen-vacancy migration," *Applied Physics A: Materials Science & Processing*, vol. 123, p. 561, Aug. 2017.

[188] F. Wu, X. He, J. Zhang, B. Yang, E. Sun, J. Jiang, and W. Cao, "Optical bandgap and dispersions of $0.24Pb\left(In_{1/2}Nb_{1/2}\right)O_3 - 0.43Pb\left(Mg_{1/3}Nb_{2/3}\right)O_3 - 0.33PbTiO_3$ single crystal poled along $[011]_c$ direction," *Optical Materials*, vol. 60, pp. 101–104, 2016.

[189] C. He, Z. Chen, H. Chen, T. Wu, J. Wang, X. Gu, Y. Liu, and K. Zhu, "Anisotropy electric and optical properties of pimnt single crystal," *Journal of Nanophotonics*, vol. 12, p. 1, 2018.

[190] R. Nechache, C. Harnagea, and A. Pignolet, "Multiferroic properties—structure relationships in epitaxial Bi_2FeCrO_6 thin films: recent developments," *Journal of Physics: Condensed Matter*, vol. 24, no. 9, p. 096001, 2012.

[191] S. M. Young, F. Zheng, and A. M. Rappe, "First-principles calculation of the bulk photovoltaic effect in bismuth ferrite," *Phys. Rev. Lett.*, vol. 109, p. 236601, 2012.

[192] G. Cheroff and S. P. Keller, "Optical transmission and photoconductive and photovoltaic effects in activated and unactivated single crystals of zns," *Phys. Rev.*, vol. 111, pp. 98–102, 1958.

[193] V. M. Fridkin and B. N. Popov, "Anomalous photovoltaic effect in ferroelectrics," *Sov. Phys. Usp.*, vol. 21, p. 981, 1978.

[194] C. M. Ramsdale, J. A. Barker, A. C. Arias, J. D. MacKenzie, R. H. Friend, and N. C. Greenham, "The origin of the open-circuit voltage in polyfluorene-based photovoltaic devices," *J. Appl. Phys.*, vol. 92, no. 8, pp. 4266–4270, 2002.

[195] S. Dubey, J. N. Sarvaiya, and B. Seshadri, "Temperature dependent photovoltaic (pv) efficiency and its effect on pv production in the world - a review," *Energy Procedia*, vol. 33, pp. 311–321, 2013.

[196] T. R. Shrout, Z. P. Chang, N. Kim, and S. Markgraf, "Dielectric behavior of single crystals near the $(1-x)Pb(Mg_{1/3}Nb_{2/3})O_3 - (x)PbTiO_3$ morphotropic phase boundary," *Ferroelectrics Letters Section*, vol. 12, no. 3, pp. 63–69, 1990.

[197] S. Ueda, I. Tatsuzaki, and Y. Shindo, "Change in the dielectric constant of *SbSI* caused by illumination," *Phys. Rev. Lett.*, vol. 18, pp. 453–454, 1967.

[198] P. Poosanaas, A. Dogan, S. Thakoor, and K. Uchino, "Influence of sample thickness on the performance of photostrictive ceramics," *J. Appl. Phys.*, vol. 84, no. 3, pp. 1508–1512, 1998.

[199] X. Zhang, X. Guo, B. Cui, J. Yun, J. Mao, Y. Zuo, and L. Xi, "Light modulation of magnetization switching in *PMN-PT/Ni* heterostructure," *Appl. Phys. Lett.*, vol. 116, no. 13, p. 132405, 2020.

[200] D. Kundys, A. Cascales, A. S. Makhort, H. Majjad, F. Chevrier, B. Doudin, A. Fedrizzi, and B. Kundys, "Optically rewritable memory in a graphene-ferroelectric-photovoltaic heterostructure," *Phys. Rev. Applied*, vol. 13, p. 064034, 2020.

Anatolii MAKHORT

Tuning photovoltaic properties in ferroelectric materials

Résumé

Les cellules photovoltaïques conventionnelles approchent leur limite fondamentale. Bien que les matériaux électriquement polaires offrent une solution alternative, la compréhension de leurs propriétés photovoltaïques, ainsi que la rareté des composés efficaces constituent un défi important. Cette thèse été consacrée à la recherche d'un composé photovoltaïque dit modèle et optimisation de sa performance. En conséquence, les propriétés photovoltaïques ont été découvertes dans le complexe PMN–xPT. Il est démontré l'existence d'une non-linéarité dans le photo-courant dans l'état de polarisation saturée qui peut également entraîner un effet de mémoire optique. Les études de l'influence de la température et de la déformation sur l'effet photovoltaïque ont été également menées. Les résultats globaux obtenus suggèrent fortement la nature hautement sensible et réglable des effets photovoltaïques et ouvrent les perspectives pour augmenter l'efficacité des cellules photovoltaïques et au-delà.

Mots clés : ferroélectrique, photovoltaïque, réglage

Résumé en anglais

Conventional solar cells are ultimately approaching their fundamental limit. Although electrically polar materials provide an alternative solution, understanding their photovoltaic properties, as well as a scarcity of efficient compounds constitute an important challenge. Therefore, this thesis was devoted to finding a model photovoltaic compound and optimization of its performance. As a result, the photovoltaic properties were discovered in the PMN–xPT complex. It was shown a nonlinearity in the photocurrent in the saturated polarization state that also results in optical memory effect. The stress and temperature-dependent studies of the photovoltaicity were performed as well. The overall obtained results strongly suggest the highly tunable nature of photovoltaic effects and open the prospect for additional degrees of freedom to increase ferroelectric-based photovoltaic cells efficiency and beyond.

Keywords: ferroelectric, photovoltaic, tuning